

# Heterostructure development and quantum control for semiconductor qubits

by

Bohdan Khromets

A thesis  
presented to the University of Waterloo  
in fulfillment of the  
thesis requirement for the degree of  
Master of Science  
in  
Physics - Quantum Information

Waterloo, Ontario, Canada, 2021

© Bohdan Khromets 2021

## **Author's Declaration**

This thesis consists of material all of which I authored or co-authored: see Statement of Contributions included in the thesis. This is a true copy of the thesis, including any required final revisions, as accepted by my examiners.

I understand that my thesis may be made electronically available to the public.

## Statement of contributions

The introductory chapter 1 does not contain any significant original results. Excluding introductions, the rest of the thesis consists of original contributions by Bohdan Khromets, with the following exceptions:

- In chapter 2, AFM scans were obtained by Yinqiu (Peyton) Shi and Trevor Blaikie. The FIB preparation of the samples for cross-sectional imaging, STEM and EELS data acquisition are thanks to the staff members of the Canadian Center for Electron Microscopy at McMaster University, Hamilton, Ontario, Canada. However, all image processing and analysis for the thesis have been done by Bohdan Khromets.
- Chapter 3 is dedicated to a big collaborative software project QuDiPy<sup>1</sup>. A non-exhaustive list of people involved in software development at different stages of the project is the following: Bohdan Khromets, Brandon Buonacorsi, Stephen Harrigan, Zach Merino, Aaranya Alexander, Joanna Roy. Bohdan Khromets has been one of the leading authors from the very beginning, has reviewed most of the other's code, and is the current chief developer and maintainer of the repository. The conceptualization of the software structure, used as a reference for table 3.1, is mainly due to Brandon Buonacorsi, Stephen Harrigan and Bohdan Khromets. Stephen Harrigan and Bohdan Khromets equally contributed to the creation of the node operation simulation diagram from figure 3.4.
- In section 3.4 of chapter 3, only the theoretical foundations and algorithms developed and/or implemented by Bohdan Khromets are presented. The only exception is subsection 3.4.2, where the contributions by Brandon Buonacorsi and Marek Korkusinski (the co-authors of our article [1]) are more significant.
- In section 4.6 of chapter 4, the software Bohdan Khromets created for voltage pulse engineering incorporates, among other things, the results of the simulations performed by Rubaya Absar, and the software developed by Stephen Harrigan and Zach Merino, as noted in text.

---

<sup>1</sup>Link to the GitHub repository: <https://github.com/mainCSG/QuDiPy>

## Abstract

States of confined electrons in semiconductors are promising candidates for quantum bits with high controllability, scalability, and coherence. Particularly, spin quantum dots offer direct integration with the modern MOS technology, whereas the exotic Majorana bound states are virtually immune to decoherence. In all cases, high-quality material system design is necessary for the fabrication of quantum devices, and the physical quantities that drive qubit operations require optimal pulse engineering for deterministic quantum control.

The first goal of our study is to develop a consistent procedure of epitaxial InGaAs metallization with a flat Al layer and a pristine metal-semiconductor interface, necessary for the future observation of Majorana quasiparticles. The comprehensive analysis of the kinetics of Al on III-V heterostructures we carried out shows that the effects of deposition rate and methods of Al surface protection are understudied. With cross-sectional transmission electron microscopy, we demonstrate high heterostructure quality using As<sub>4</sub> as a capping layer and an order of magnitude larger Al deposition rate than previously reported. Based on the subsequent analysis for different Al growth rates and cappings, we conclude that faster rates are beneficial to minimize heat transfer to the wafer, protect the uncapped Al surface from rearrangement, and improve its morphology.

Our second goal is to simulate the operation of a voltage- and ESR-controlled, quantum-dot-based spin quantum processor in silicon. To achieve this, we devise methods to extract the Hubbard model and spin interaction parameters from the electric potential landscape simulations of realistic device geometries. In addition, we present a novel, numerically efficient algorithm for voltage and ESR field pulse engineering that yields a theoretical 100% fidelity, preserves charge stability, and automatically incorporates all cross-couplings between quantum dots. The general optimal control formulation makes it possible to use the method in conjunction with gradient optimization routines. The algorithms are implemented as parts of a general-purpose, open-source Python package for semiconductor quantum dot simulations.

We expect that the obtained results will further facilitate the development of semiconductor qubits, and become a stepping stone towards the realization of hybrid quantum dot-Majorana devices.

## Acknowledgements

First and foremost, I sincerely thank my supervisors, Jonathan Baugh and Zbig Wasilewski, for their relentless support in all academic matters during my Master's studies. I also thank the members of both of my research groups: Stephen Harrigan, Alex Currie, Brandon Buonacorsi, Alan Tam, Chris Deimert, Peyton Shi, and others, for all their time, help, shared knowledge, and a very positive social experience. I am always grateful to all my family, whose care, patience and empathy I cannot overstate, and my numerous Ukrainian friends, now scattered across the globe, for their support and desire to deepen our friendships despite all distances and borders. I thank all schools I studied in, all my teachers and people who contributed to my development at all stages of my life for rendering me capable of doing graduate studies at the prestigious University of Waterloo. Finally, I thank Fr. Eugene Shchukin and all my friends from the parish of Saint Patriarch Tikhon Confessor and New Martyrs of Russia (Russian Orthodox Church Abroad) for great encouragement to grow spiritually, and being as close to a second family as possible during my stay in Canada.

Overall, I thank everybody for transforming my Master's studies into a process of enormous scientific, intellectual, personal, emotional, and spiritual growth that made me the man I am today.

# Table of Contents

List of Figures	x
List of Tables	xiii
<b>1 Quantum information processing with low-dimensional semiconductor systems</b>	<b>1</b>
1.1 Energy states of electrons in semiconductors . . . . .	1
1.1.1 General energy properties . . . . .	1
1.1.2 Electron interactions in the semiconductor . . . . .	3
1.1.3 Realization of zero-energy states . . . . .	4
1.2 Control of electron interactions for quantum gate operations on spins . . . . .	6
1.2.1 Single-qubit operations . . . . .	6
1.2.2 Two-qubit operations . . . . .	7
1.3 Combined quantum operation of localized electrons and Majorana fermions	8
1.3.1 Non-abelian braiding . . . . .	8
1.3.2 Integration with quantum dots for universal computation . . . . .	8
<b>2 Epitaxial metallization of III-V heterostructures with aluminum</b>	<b>11</b>
2.1 Motivation . . . . .	11
2.2 Epitaxial heterostructure growth and characterization . . . . .	13
2.3 Kinetics of aluminum growth on semiconductors . . . . .	16

2.3.1	Effects of crystal structure and symmetry . . . . .	16
2.3.2	Atomic transport . . . . .	17
2.3.3	Strain and energetics . . . . .	18
2.4	Realization of heterostructure with flat Al layer and sharp interfaces . . . . .	20
2.4.1	Statement of experimental problem . . . . .	20
2.4.2	Surface flatness and layer structure confirmation . . . . .	22
2.4.3	Cross-sectional microscopy and spectroscopy with atomic resolution . . . . .	26
2.5	Deposition rate optimization and surface protection for low-temperature growth . . . . .	32
2.5.1	Choice of growth parameters for investigation . . . . .	32
2.5.2	Wafer temperature monitoring during the aluminum deposition . . . . .	32
2.5.3	Evolution of surface reconstruction . . . . .	36
2.5.4	Post-growth imaging . . . . .	42
2.5.5	Surface morphology studies with AFM . . . . .	46
2.6	Summary of chapter 2 . . . . .	52
<b>3</b>	<b>Algorithm and software design for a spin-qubit quantum architecture simulation</b>	<b>54</b>
3.1	Motivation . . . . .	54
3.2	Spin qubit quantum computer architecture in silicon . . . . .	56
3.3	QuDiPy: a quantum dot simulation package . . . . .	59
3.3.1	Simulation of the node operation . . . . .	59
3.3.2	Scope of the simulator . . . . .	62
3.4	Theoretical foundations of the simulator . . . . .	65
3.4.1	Potential data extraction and manipulation . . . . .	65
3.4.2	Determination of the many-electron energy spectrum . . . . .	67
3.4.3	Construction of effective Hamiltonians . . . . .	70
3.4.4	Spin dynamics simulation . . . . .	74
3.5	Summary of chapter 3 . . . . .	79

<b>4</b>	<b>Efficient constrained pulse engineering for spin qubits</b>	<b>80</b>
4.1	Introduction . . . . .	80
4.2	Pulse engineering method . . . . .	82
4.2.1	Control problem definition . . . . .	82
4.2.2	Activation function . . . . .	82
4.2.3	Expression for the cost function . . . . .	84
4.2.4	Stability of charge configuration . . . . .	85
4.2.5	Restriction on absorbed RF electromagnetic energy . . . . .	90
4.2.6	Restriction on voltage sweep rates . . . . .	91
4.3	Design of effective parameter pulses for primitive quantum gates . . . . .	92
4.3.1	Choice of the gates to design . . . . .	92
4.3.2	Idling qubits . . . . .	93
4.3.3	Z rotations . . . . .	94
4.3.4	X and Y rotations . . . . .	95
4.3.5	Arbitrary rotations . . . . .	98
4.3.6	SWAP <sup>k</sup> pulses . . . . .	100
4.4	Preliminary quantum circuit optimization . . . . .	103
4.4.1	Rotation angle shift by $2\pi$ . . . . .	103
4.4.2	Hybrid gates . . . . .	104
4.4.3	Parallel execution of gates . . . . .	105
4.5	Engineering of voltage pulses . . . . .	109
4.5.1	Connection between physical and effective parameters . . . . .	109
4.5.2	Voltage values for idling qubits . . . . .	110
4.5.3	General formalism for voltage control pulse engineering . . . . .	112
4.5.4	Constraint satisfaction . . . . .	114
4.5.5	Choice of shape function . . . . .	116
4.6	Examples of single-qubit gate simulations . . . . .	118



4.6.1	Relations between effective and physical parameters for a standalone quantum dot . . . . .	118
4.6.2	High-fidelity resonant and nonresonant spin rotations . . . . .	121
4.7	Summary of chapter 4 . . . . .	125
<b>5</b>	<b>Gradient ascent pulse engineering for spin qubits</b>	<b>126</b>
5.1	Motivation . . . . .	126
5.2	Operator formalism for quantum system evolution . . . . .	128
5.2.1	Liouville equation . . . . .	128
5.2.2	Toggling frame . . . . .	130
5.2.3	Directional derivatives . . . . .	131
5.2.4	Van Loan method . . . . .	132
5.3	Control problem formulation for gradient minimization . . . . .	135
5.3.1	Spin dynamics: generalization to a nonlinear problem . . . . .	135
5.3.2	Expression for the cost function . . . . .	137
5.3.3	Maximizing fidelity . . . . .	138
5.3.4	Lowering susceptibility to decoherence . . . . .	139
5.4	Summary of chapter 5 . . . . .	141
<b>6</b>	<b>Conclusions and future work</b>	<b>142</b>
	<b>References</b>	<b>144</b>

# List of Figures

1.1	A prototypical, voltage controlled device for the information transfer between a quantum dot and Majorana fermions, proposed in ref. [25] . . . . .	9
2.1	Veeco Gen10 MBE system, used in our lab. . . . .	14
2.2	Aluminum grains at the lattice constant threshold value $a=5.98 \text{ \AA}$ corresponding to the two possible Al growth modes [39]. . . . .	19
2.3	Full InP (100) wafer, with flats and crystallographic directions. . . . .	20
2.4	BB photos of G0680 and G0697. . . . .	23
2.5	AFM micrographs of the mirror-like (left) and hazy areas (right) of G0680. Surface point defects (framed) of this kind are seen all across the sample. . . . .	24
2.6	STM scans of G0697: near the surface (left), and at the $\text{In}_{0.53}\text{Ga}_{0.47}\text{As} / \text{InP}$ interface (right). . . . .	25
2.7	Surface after annealing at 400 °C for 30 min, resolved with STM. . . . .	25
2.8	Layer thickness measurements with cross-sectional SEM on G0697. . . . .	26
2.9	Thin lamella machined with FIB for G0697. . . . .	27
2.10	TEM with a 1 nm resolution confirms the flatness of G0680 layers on a $\mu\text{m}$ scale. . . . .	27
2.11	TEM and EELS scans with 0.15 nm resolution, with the highlighted $\text{AlO}_x$ region inside the As cap layer. . . . .	28
2.12	Expected layer structure (left), compared to the STEM micrographs of G0680 in the areas around Al layer (center and right). . . . .	29
2.13	10 nm resolution STEM scan of G0697: nonuniformity on a micron scale. . . . .	30

2.14	EELS of G0697 resolves intermittent In and Ga clusters within Al layer, indicative of significant group-III exchange. . . . .	30
2.15	BET temperature data with the fit to a first-order model (2.2). . . . .	34
2.16	Heterostructure temperature measured with BET as a function of the thermal energy outputted from Al cells. . . . .	36
2.17	The onset of amorphous rings in Gr0.5As . . . . .	40
2.18	The evolution of RHEED pattern of Gr0.5, starting from the end of Al deposition. . . . .	41
2.19	Evolution of Gr2.0 RHEED pattern over the course of a month. . . . .	42
2.20	BB photos of the wafers capped with As <sub>4</sub> . . . . .	43
2.21	BB photos of the wafers not capped with arsenic: bulging or large-scale roughness. . . . .	43
2.22	25 $\mu\text{m} \times 25 \mu\text{m}$ scans of the mirror-like and hazy areas of Gr2.0As. . . . .	48
2.23	Horizontally elongated shallow features and atomic-level flatness in Gr2.0As. . . . .	49
2.24	The AFM scans of the “wavy” parts of Gr0.5 and Gr2.0, featuring atomic flatness. . . . .	49
3.1	Device-level proposal for a compute node . . . . .	57
3.2	4-step cycle of the surface code error-correction algorithm . . . . .	57
3.3	Quantum circuit for the data qubit stabilization of a group of four nodes. Reproduced from [65]. . . . .	58
3.4	Pulse desing for quantum node operations with QuDiPy. . . . .	60
3.5	Processing of an analytical 2-dimensional potential. . . . .	66
3.6	Dependence of the optimization function $f_{\min}(\omega)$ on $\omega$ and the size of the harmonic orbital basis ( $M_x M_y = M$ ). Reproduced from [1] . . . . .	69
4.1	Activation function $\Xi_p(x, \alpha)$ . . . . .	83
4.2	Extending the charge stability boundaries to the regions with different total charges. . . . .	89
4.3	Number of electrons in the left dot of a 2-dot system at different values of detuning $\epsilon$ and tunnel coupling $t$ . Reproduced from [77] . . . . .	89

4.4	Hybrid ROT - SWAP gates. . . . .	105
4.5	Diagram of plunger and tunnel gate arrangement in the qubit node. . . . .	109
4.6	Single-dot device structure emulated in <code>nextnano++</code> . . . . .	119
4.7	Potential energy and electric field landscapes, obtained from <code>nextnano++</code> simulation at $z = -0.2$ nm, $V = 0.5$ V. . . . .	120
4.8	Deviation $g$ -factor dependency on the plunger gate voltage in a single dot geometry, obtained from <code>nextnano++</code> electric potential and field data. . . . .	121
4.9	Single qubit rotation simulations of a system of two antiparallel spins. . . . .	122
4.10	Evolution of the Bloch vector of the first electron at each step of the quantum circuit from fig. 4.9. . . . .	122
4.11	Sequence of voltage and ESR field control pulses that realizes the quantum circuit from figure 4.9. . . . .	123
4.12	Time evolution of the 2-electron system spin state. . . . .	124

# List of Tables

2.1	Summary of the employed characterization techniques. . . . .	15
2.2	Lattice constants of some zinc blende III-V compounds, and Al. . . . .	16
2.3	Heterostructure design adopted for all our MBE growths. . . . .	20
2.4	In1 and Ga2 cell flux parameters for the growth of two InGaAs buffers in G0680. . . . .	22
2.5	A series of growth with varied deposition rates and capping. . . . .	33
2.6	Temperature dynamics during and after the Al deposition: measured and fitted data. . . . .	35
2.7	Surface reconstructions for selected semiconductor heterostructures, reported in works [44–48] . . . . .	37
2.8	RHEED pattern time evolution during the aluminum deposition on Gr0.5As. . . . .	37
2.9	Evolution of the RHEED pattern at a fixed azimuth during the aluminum deposition. . . . .	39
2.10	Strained growth of Al or AlAs: time before the growth of relaxed Al begins, and the thickness of the strained part. . . . .	40
2.11	Nomarski images of the wafers capped with amorphous arsenic. . . . .	45
2.12	Nomarski images of the uncapped wafers (x40 magnification), showing no significant morphology differences in the areas differently affected by the Al migration. . . . .	46
2.13	AFM scans of the mirror-like areas of Gr0.1As and Gr0.5As. . . . .	47
2.14	Summary of the distinct feature types identified with AFM in Gr0.1As–Gr2.0 samples. . . . .	51

3.1	Functionality and intended use of QuDiPy modules. . . . .	64
3.2	Algorithm for the extraction of Hubbard parameters from potential landscape. . . . .	73
4.1	Values of ESR phases $\phi$ to be supplied during spin rotations around $\hat{x}$ and $\hat{y}$ axes. . . . .	95
4.2	Relative changes in pulse parameters upon the shift of angle of rotation by $2\pi$ . . . . .	104
4.3	Voltage-driven quantum gates that can be run in parallel. . . . .	107
4.4	Voltage and ESR-driven quantum gates that can be run in parallel. . . . .	108
5.1	Components of the spin evolution generator. If higher precision is required, influence of all voltages on $\delta g_k, J_k$ can be taken into account. . . . .	135
5.2	Derivatives with respect to the control parameters of a nonlinear spin dynamics control problem. . . . .	136

# Chapter 1

## Quantum information processing with low-dimensional semiconductor systems

### 1.1 Energy states of electrons in semiconductors

#### 1.1.1 General energy properties

The power and ubiquity of semiconductor technology are directly connected to the quantum properties of semiconductors. One of the key properties is that at zero temperature, their electrons fully populate the lowest energy band (valence band). When the temperature goes above zero, a small fraction of electrons from this band are excited to the band above (conduction band). Thus, under normal circumstances, all electronic properties of semiconductors are determined by the electrons at the bottom of the conduction band, or at the top of the valence band (in this band, however, it is more convenient to work with the few *unpopulated* states, interpreted as “holes” with positive charges and masses). Both extrema can be always approximated with quadratic polynomials, corresponding to the following dispersion relation:

$$E(\vec{k}) = E_0 + \frac{\hbar^2(\vec{k} - \vec{k}_0)^2}{2m^*}, \quad E_0 \equiv E(\vec{k}_0). \quad (1.1)$$

Here,  $\vec{k}_0$  denotes the extremum of the conduction (or valence) band, and  $m^*$  is the parameter one can interpret as the electron (or hole) *effective* mass. Indeed, formula (1.1)

describes nothing but a motion of a free quantum particle with the momentum  $\vec{p} = \hbar\vec{k}$  and mass  $m^*$  in a reference frame that moves with the constant momentum  $\hbar\vec{k}_0$ . This essentially means that we can ignore a very strong and nonuniform crystal field as long as we treat electrons as quasiparticles with the effective mass  $m^*$  (and also the opposite charge when we describe holes in the valence band). Without loss of generality, only electrons in the conduction band will be discussed further.

If the electrons are in any way confined, this modifies another fundamental property of semiconductors: density of states,  $g(E) = \frac{dn}{dE}$ . This quantity defines the concentration of the electrons  $dn(E)$  whose energies lie in the interval  $[E, E + dE]$ . For the systems of different dimensionality,  $g(E)$  has different dependencies on the electron energy:

$$g_{3D} \propto \sqrt{E - E_0}, \quad g_{2D} = \text{const}, \quad g_{1D} \propto \frac{1}{\sqrt{E - E_0}} \quad g_{0D} \propto \delta(E - E_0). \quad (1.2)$$

This indicates that the presence of confinement fundamentally changes the way how the conduction band is filled with electrons. Namely, higher level of confinement groups the electron energies closer to the value  $E_0$ <sup>1</sup> This effect inevitably changes of electron transport properties, and is thus of major theoretical and experimental interest.

On the one hand, the modern level of technology allows for the creation of physically low-dimensional systems: 1 monolayer-thick flakes (e.g., graphene), nanowires, and nanoparticles. On the other hand, the effective confinement can be also achieved in planar structures, which are much more common in the modern semiconductor electronics technology. In particular, band bending that occurs at the interface of distinct semiconductor layers such as Si and SiO<sub>2</sub> creates a triangular potential well in the out-of-plane direction. This effect localizes the electrons in the vicinity of the interface, leading to the formation of a 2-dimensional electron gas (2DEG). Another approach to achieve confinement is band gap engineering, where compounds with distinct electron affinities and band gaps are combined in one heterostructure to give a desired potential well profile. Experimentally, this can be achieved, for example, with molecular beam epitaxy [2]. The subsequent gating of such quantum well structures allows to electrostatically define any one-dimensional channels [3] or arrays of quantum dots, consistent with the modern MOS or CMOS technology [4].

---

<sup>1</sup>As all physical objects are in fact three-dimensional, the electronic states are confined to a series of values  $\{E_i \geq E_0\}$  rather than a single value  $E_0$ . They denote electronic *subbands* within the conduction band that emerge due to a quantum confinement along some of the object dimensions



### 1.1.2 Electron interactions in the semiconductor

For quasi-free electrons in the conduction band, the kinetic part of the Hamiltonian is conventional:

$$H_T = \sum_i -\frac{\hbar^2}{2m^*} \frac{\partial^2}{\partial \vec{r}^2}$$

In addition, since electrons are charged particles, the pairwise Coulomb interaction between them is always present:

$$v = \sum_{i>j} \frac{e^2}{4\pi\epsilon_0\epsilon_r|\vec{r}_i - \vec{r}_j|}, \quad (1.3)$$

where the relative permittivity  $\epsilon_r$  of the semiconductor incorporates the effect of screening. Apart from the orbital, spin degree of freedom is intrinsic to all electrons in nature. When an external magnetic field  $\vec{B}$  is applied, it directly couples to the spin operator  $\vec{S}$  of each electron:

$$H_z = g\vec{B} \cdot \vec{S} = \frac{g}{2}\mu_B\vec{B} \cdot \vec{\sigma}, \quad (1.4)$$

where  $\mu_B = 5.788 \cdot 10^{-2} \frac{\text{meV}}{\text{T}} = 9.274 \cdot 10^{-24} \frac{\text{J}}{\text{T}}$  is the Bohr magneton,  $g$  is the electron Lande factor, and  $\vec{\sigma}$  is the vector of Pauli matrices  $X, Y, Z$ . It immediately follows from the Hamiltonian 1.4 that a constant external field induces energy splitting in the spectrum by  $g\mu_B B$  (Zeeman effect).

The spin and orbital degrees of freedom can couple through the mechanism known as spin-orbit interaction. For electrons in individual atoms, this is a relativistic effect due to electron motion in the nuclear electric potential. In its own reference frame, an electron couples to the effective magnetic field induced by the motion of charged nuclei  $\vec{B}_{eff} = \frac{\vec{E} \times \vec{v}}{c^2}$ . In solids, the effect is of a more complex nature related to interband electron scattering; nevertheless, the corresponding Hamiltonian can be still written in a general form:

$$H_{SO} = a\vec{L} \cdot \vec{S}, \quad (1.5)$$

where  $\vec{L} = \vec{p} \times \vec{r}$  is the orbital angular momentum of the quasielectron.

When we want to describe individual electrons as opposed to their statistical parameters, it is always convenient to work within the spin space only whenever possible. Indeed, using the algebra of Pauli operators:

$$\sigma_i \sigma_j = \delta_{ij} + i\epsilon_{ijk} \sigma_k$$

is much simpler analytically and numerically than manipulating such continuous variables as electron position vectors. Fortunately, due to Pauli principle, the exchange interaction

Hamiltonian 1.3 for each pair of electrons can be mapped onto a pure spin Heisenberg Hamiltonian [5]:

$$\frac{e^2}{4\pi\epsilon_0\epsilon_r|\vec{r}_1 - \vec{r}_2|} \Rightarrow H_{\text{H}} = \frac{J}{\hbar^2} \vec{S}_1 \cdot \vec{S}_2$$

This effective interaction is commonly referred as exchange, and  $J$  is known as exchange coupling parameter (in units of energy). If Coulomb interaction is small enough to be considered a perturbation, the parameter  $J$  is mainly determined by the overlap between the single-electron wavefunctions of the two electrons.

In 2D and 1D systems, spin-orbit interaction can be also mapped onto an effective spin model of Rashba or Dresselhaus spin-orbit coupling [6]. In addition, this interaction indirectly manifests itself in the change of electron  $g$ -factor (this applies to systems of all dimensions). For example, in InSb quantum wells, a strong interband coupling due to a very small bandgap leads to extreme negative values of this parameter:  $-g \sim 35\text{-}50$  [7, 8].

### 1.1.3 Realization of zero-energy states

The interplay of various interactions can lead to exotic electron phases in semiconductors. One prominent example is the quasiparticles known as Majorana fermions. These particles are not truly fermions (they obey their own statistics), always exist in pairs, are localized at the system edges, and realize an exotic zero-energy Majorana zero mode (MZM), doubly degenerate in fermion (i.e. electron) parity. The Majorana quasiparticle operators are Hermitian and are equal superpositions of the electron creation and annihilation operators:

$$\gamma_1 = a + a^\dagger, \quad \gamma_2 = -i(a - a^\dagger), \quad (1.6)$$

Thus, these particles can be referred as “half” an electron each.

The possibility of observing such quasiparticles in the semiconductors with same-spin (or  $p$ -type) pairing was first theorized in the seminal paper by Kitaev [9]. Although pure pairing of this kind is almost nonexistent in nature, its effective analog can be engineered in more accessible material systems, as was shown by Lutchyn *et al.* [10] and Oreg *et al.* [11]. Particularly, a quasi-1-dimensional semiconductor with spin-orbit coupling in the proximity of a superconductor can host an MZM if the axially applied Zeeman field  $B$  exceeds the value [12]:

$$B_{\text{c}} = \frac{2}{g\mu_{\text{B}}} \sqrt{\Delta^2 + \mu^2}, \quad (1.7)$$

where  $\Delta$  is the superconducting gap induced in the semiconductor, and  $\mu$  is the chemical potential. This value marks the onset of a topologically protected MZM phase, where the

doubly-degenerate zero energy level is separated from other levels by an energy gap. This property is especially valuable for quantum information processing, since the decoherence can be almost fully avoided with the use of topologically protected quasiparticles [12].

Yet, a careful choice of material system parameters is necessary to observe this quasiparticles in nature. First, a large spin-orbit coupling (for better Majorana fermion localization at the edges [12]) and a large  $g$ -factor (for higher Zeeman energy) in the semiconductor are required. In particular, the current dominance of InAs and InSb-based quantum wire and quantum well devices in the field is because both of these properties are highly pronounced in these material systems. Second, the critical magnetic field of the superconducting metal should be higher than the threshold value 1.7. Thin Al layers [13] and niobium-containing compounds [14] tend to meet this criterion well. Last but not least, overall high purity and good sharpness of superconducting-semiconductor interface are highly desirable, which makes molecular beam epitaxy a perfect choice of the technology.

Over the past decade, significant progress has been made towards the observation of this exotic phase, though the evidence is still not conclusive. The experimental methods chiefly rely on the zero-bias conductance peak measurements [14–17], Coulomb blockade tunnel spectroscopy [18], observation of  $4\pi$ -periodic Josephson effect [19]. Earlier studies predominantly involved nanowires, but gearing towards the 1-dimensional voltage-defined channels in a 2DEG [3] appears to be the current trend.

## 1.2 Control of electron interactions for quantum gate operations on spins

The abundance of interactions in semiconductors led to the development of numerous quantum control methods to drive qubit operations. Since universal quantum computation requires only a set of properly chosen single- and two-qubit gates, its realization is generally sufficient to achieve this goal.

### 1.2.1 Single-qubit operations

The longest known (and thus the most developed) method for single-electron spin manipulation is electron spin resonance (ESR). When a static Zeeman field  $\vec{B}_0$  is applied on a qubit, it is known to induce a constant spin precession around the direction of the field with the Larmor frequency  $\omega_0 = g\mu_B B_0/\hbar$ . This immediately follows from formula (1.4) if we write the corresponding evolution operator:

$$U_z = e^{-\frac{i}{\hbar}H_z} = e^{-\frac{it}{\hbar}\vec{B}_0 \cdot \vec{\sigma}},$$

and use a well-known fact that an angular momentum operator  $\vec{S}$  is the generator of rotation by an angle  $\theta$  around a unit vector  $\vec{n}$  [20]:

$$R(\vec{n}, \theta) = e^{-i\theta \frac{\vec{S} \cdot \vec{n}}{\hbar}}.$$

The situation is different when two magnetic fields, namely, static Zeeman  $\vec{B}_0$ , and oscillating radio frequency  $\vec{B}_{\text{RF}}$ , are applied in perpendicular directions. The Hamiltonian then reads:

$$H_{\text{ESR}}/\hbar = \frac{\omega_0}{2}Z + \frac{\Omega}{2}[X \cos(\omega_{\text{RF}}t + \phi) + Y \sin(\omega_{\text{RF}}t + \phi)], \quad \Omega = g\mu_B B_{\text{RF}}/\hbar \quad (1.8)$$

If we move to a reference frame, also known as the rotation frame, where the fast Larmor precession is “unwound”:

$$|\psi_{\text{rot}}\rangle = e^{i\frac{\omega_0 Z}{2}} |\psi_{\text{lab}}\rangle,$$

the Hamiltonian will transform to the following form (up to a small fast-oscillating component that can be neglected):

$$H_{\text{rot}} = (\omega_0 - \omega_{\text{RF}})\frac{Z}{2} + \frac{\Omega}{2}(X \cos \phi + Y \sin \phi) \quad (1.9)$$

Expression (1.9) embodies the essence of ESR method: if the frequency of the oscillating field is tuned in resonance with Larmor frequency, a qubit realizes deterministic rotations around the axis in the plane of the oscillating field, with the axis direction specified by its phase. Conversely, detuning from resonance at  $B_{\text{RF}} = 0$  drives spin rotations around  $\hat{z}$  axis. Therefore, ESR provides a way to drive arbitrary rotations of a single qubit. This is a wide class of quantum gates that lacks only one additional two-qubit gate to achieve universal quantum computation.

Another method commonly used to implement single-qubit gates is the electric dipole spin resonance (EDSR). In this method, spin rotations are realized by changing the dipole characteristics of an electron with the external electric field. Even though spin-orbit coupling can be harnessed for this purpose, a much more intuitive method is presented in the works [21, 22] and commonly used overall. A micromagnet creates a gradient of magnetic field perpendicular to the global Zeeman field  $\vec{B}_0$ . The electron is periodically displaced with the external electric field along this gradient. The oscillating coupling is quantified with a time-dependent spin Hamiltonian of the type 1.8. This means that the scope of quantum control achievable with EDSR is equivalent to ESR.

## 1.2.2 Two-qubit operations

The key component of any two qubit spin gate is the exchange coupling 1.3. The Heisenberg Hamiltonian expression  $\propto \vec{\sigma}_1 \cdot \vec{\sigma}_2$  is closely related to a 2-qubit SWAP gate:

$$\text{SWAP} = \frac{1}{2} (I_1 I_2 + X_1 X_2 + Y_1 Y_2 + Z_1 Z_2),$$

Unfortunately, SWAP does not form a set of universal gates with single-qubit rotations, but it turns out that  $\sqrt{\text{SWAP}}$  does. It can be shown (cf. sec. 4.3) that 2-qubit exchange directly realizes any gate of type  $\text{SWAP}^k$ .

It is also possible to combine exchange and Zeeman interactions in case  $J \ll \hbar\omega_0$  to create universal two-qubit gates of other kinds such as  $\frac{1}{\sqrt{2}}(I_1 I_2 + iZ_1 Z_2)$  [23], and its more general version, Ising gate [22].

## 1.3 Combined quantum operation of localized electrons and Majorana fermions

### 1.3.1 Non-abelian braiding

Majorana fermions are highly nonlocal, and the only quantum operation that can be realized with them can be their exchange (for example, by moving the borders of a 2-dimensional T-junction with voltage sweeps, as suggested in [24]). From their topological properties, it follows that their exchange leads to the following transformation of their operators [12]:

$$\gamma_1 \rightarrow -\gamma_2, \quad \gamma_2 \rightarrow \gamma_1,$$

which corresponds to a unitary operation:

$$U_{12} = e^{-i\frac{\pi}{4}\gamma_1\gamma_2}. \quad (1.10)$$

The most remarkable property of the Majorana exchange operation can be seen when there is more than one pair of such quasiparticles in the system. Then, the exchange operations on the Majoranas from different pairs generates a superposition of both charge states. Moreover, distinct exchange operations that involve one Majorana fermion do not commute:

$$[U_{i-1,i}U_{i,i+1}] = i\gamma_{i-1,i}\gamma_{i,i+1}$$

which implies that the final state of the system where several pairs are exchanged depends on the order of these operations. This is the manifestation of a non-Abelian exchange statistics, or braiding, not observed in known elementary particles. The operation is also very attractive for fault-tolerant quantum computation: since the information is stored nonlocally, it cannot be measured by local noise operators [12]. Unfortunately, the quantum gates of type 1.10 are insufficient for universal quantum computation. Moreover, there does not exist any purely topological method of Majorana qubit readout. One way to tackle these problems is to interface the Majorana-hosting systems with spin qubits.

### 1.3.2 Integration with quantum dots for universal computation

The report [25] was chronologically the first one to suggest an algorithm to transfer quantum information between a quantum dot and an MZM both ways. The device proposal (fig. 1.1) is based on a degenerate quantum dot located amid two edges of topological

superconductors. The voltage control of the quantum dot charging energy and tunnel barriers allows to map the Majorana parity state onto a spin-qubit state or vice versa deterministically (up to a unitary transformation). Interestingly, just sweeping the voltage proves to be enough to create entanglement between Majorana and spin states. Yet, the experimental implementation of this proposal does not seem feasible due to the need for a strictly doubly-degenerate dot and Majorana channels with perfect spin polarizations in opposite directions.

The subsequent study of a system of one Majorana nanowire and one quantum dot with voltage-controlled coupling [26] sheds significantly more light on the applicability and consistency of MZM readout. The method is based on inducing the overlap between the Majorana bound states by bringing them close to each other, resonantly coupling one of them to the quantum dot, and performing a charge measurement on the dot. The method allows to directly test the oscillatory nature of a Majorana zero mode, and identify the protection of the topological order at different length scales. Unlike in [25], this proposal realistically incorporates lifted degeneracy in the quantum dot, and allows to discern distinct spin-polarized Majorana bound states.

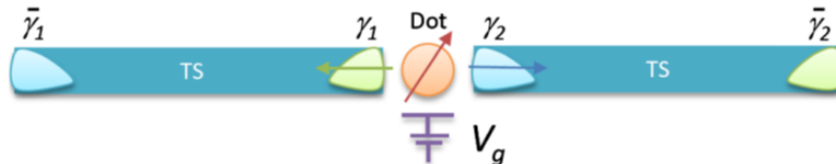


Figure 1.1: A prototypical, voltage controlled device for the information transfer between a quantum dot and Majorana fermions, proposed in ref. [25]

Based on the simple model of Majorana-dot interaction, provided in [25], further investigations derive scalable architectures with universal quantum computation. The work [27] analyses a system of 1 quantum dot between two nanowires, similar to the one from figure 1.1, and creates its more detailed quantum model that incorporates interactions due to confined electrons and Cooper pairs. From the effective dot-Majorana exchange interaction, hybrid SWAP and Phase gates, suitable for universal quantum computation, are engineered, and a modular Majorana-dot network is designed.

The subsequent study [28] proposes a fully measurement-based architecture, with the measurements being done on pairs and quartets of quantum dots by detecting changes in their ground state energy, average charge and differential capacitance. The scheme obviates the need in physical moving of Majorana fermions for braiding while realizing a Clifford-complete gate set with high fidelity. As in the study [27], the architecture is scalable and

modular. The significant improvement is grouping Majorana devices into the islands with high charging energy to protect topological states from quasiparticle poisoning. Later on, the same research group complemented their results in the article [29] with the realization of the topologically nonprotected T magic gate with exponential error suppression. A measurement-based universal dynamic decoupling algorithm incorporating nonadiabatic evolution is designed for this purpose. The magic T gate and Clifford group finally realize universality of quantum computation in this architecture.

Overall, these results indicate the abundance of methods to characterize and manipulate Majorana bound states with spin qubit, and to overcome the nonuniversality of the topologically protected braiding operation. Their implementation, however, is yet to come, as the MZMs are yet to be unambiguously detected experimentally.



# Chapter 2

## Low-temperature epitaxial metallization of III-V heterostructures with aluminum for the observation of Majorana zero modes

### 2.1 Motivation

Molecular beam epitaxy (MBE) has long been known as a superior technique to grow atomically clean planar heterostructures at the microscale and nanoscale. Particularly, it is an excellent choice for a wide class of microelectronic devices based on metal-semiconductor junctions: Schottky diodes [30, 31], field-effect transistors (FETs), high-Q resonators [32], radiation detectors, laser diodes, etc. Recently, a significant interest has grown in using MBE for the cutting-edge quantum technology, such as superconducting [32] and topological [3, 12, 15, 18] quantum bits.

The successful creation of any of these devices is contingent on a careful choice of the material system. Aluminum is a metal abundant in nature with low resistivity (down to  $2.4 \mu\Omega\cdot\text{cm}$ ), which becomes a type-I superconductor with a very large coherence length at low temperatures. Therefore, aluminum gates or shells lend themselves very well both to Schottky barrier-based and superconducting RF devices. Optoelectronic devices operation

typically relies on a direct semiconductor bandgap, which makes III-V compounds a natural choice of the semiconductor system in this case. Topological qubits impose even more requirements [12]: high  $g$ -factor and spin-orbit coupling in the semiconductor, and high critical field of the superconductor. InAs or InSb-based heterostructures with a thin Al layer on top satisfy these criteria very well.

However, the MBE growth of Al on III-V semiconductors can present difficulties. This is because multiple factors contribute to the growth mode and, subsequently, sample quality: temperature, bulk and surface crystal structure, strain, to name a few. To our best knowledge, no holistic review with the analysis of all these factors has been ever published. In addition, there is insufficient data in the literature about the effect of Al growth rate and its surface capping on the quality of the layer structure. Yet, developing a clear procedure for consistent III-V metallization with Al is particularly important to realize a material platform that can host Majorana zero modes. First of all, a sharp, clean metal-semiconductor interface is necessary to achieve significant proximity superconductivity and not to harm the electron mobility in the 2DEG. Secondly, flatness of Al layer is needed for high critical magnetic field and the ability to fabricate multiple Majorana devices on one chip consistently. Therefore, developing a comprehensive understanding of the aluminum formation on III-V heterostructures, with the special focus on InAs- and InSb-derived semiconductor compounds, is the *goal* of this chapter.

Section 2.2 gives a brief summary of the method of molecular beam epitaxy, growth monitoring and characterization techniques we used in our experiments. Section 2.3 presents a critical literature review on the topic of III-V heterostructure metallization. Here, physical mechanisms that underlie aluminum formation are deduced and put in the context of the very recent papers that also pursue topological qubits. The following sections summarize our experimental results of Al deposition on In-rich InGaAs, which is a relevant material for the heterostructures with InAs quantum wells [2]. Section 2.4 presents the characterization of our two earlier samples, featuring their cross-sectional microscopy and spectroscopy with atomic resolution. Section 2.5 is dedicated to a comprehensive investigation of Al layer formation and surface morphology evolution for different Al deposition rates, presence and absence of capping. Section 2.6 provides a summary of the results.

Some images in this chapter are acquired by other people (see Statement of Contributions for details) but all image processing and analysis are the author's. Other than this, all the following sections consist of the author's original results.

## 2.2 Epitaxial heterostructure growth and characterization

### Molecular beam epitaxy

The method of molecular beam epitaxy is conceptually simple: direct deposition of ultrapure vapors of elementary substances onto a clean wafer surface at ultra-high vacuum (UHV). However, the implementation may vary among different setups. Figure 2.1 shows a Veeco MBE Gen10 facility installed in our lab, which features automatic wafer transfer between the modules, one UHV growth module (right of figure), one UHV storage module (left of figure) and a preparation module (not shown). A wafer, loaded onto a substrate holder, is first outgassed at 200°C in the load lock, then transferred to the preparation module for the outgassing at a higher, substrate material specific, temperature. Finally, the wafer is moved to the growth module with the UHV on the order of  $10^{-10}$  Torr. At the bottom of the growth module, effusion cells with the ultrapure III-V materials: Al, Ga, In, As, Sb, and dopants: Si, Be, are located. During the epitaxial growth, the shutters covering the cells with elements needed for the grown layer are opened, while crucibles with the compounds are being heated up to the temperatures that produce desired fluxes.

### In situ growth monitoring

The advantage of MBE is not only a high-precision composition control without contamination but also the ability to monitor numerous parameters of the growth in situ, including but not limited to pressure, residual gas composition, manipulator and wafer temperature, growth surface dynamics.

In our case, the manipulator temperature is measured by a conventional thermocouple, whereas the wafer temperature is acquired with band-edge thermometry (BET). The bandgap of a semiconductor is temperature dependent. Therefore, the cutoff wavelength below which light does not pass through the wafer can be used to directly determine its temperature. The spectral position of the absorption edge has been monitored using a combination of InGaAs and Si array spectrometers to allow tracking InP substrate temperature across a broad temperature range, including sub-0°C temperatures.

The reflection high-energy electron diffraction (RHEED) technique allows to monitor the surface reconstruction and flatness in real time. An electron beam, incident on the sample surface at a grazing angle, produces a diffraction pattern that corresponds to only



Figure 2.1: Veeco Gen10 MBE system, used in our lab. The photo is reproduced from the [official Veeco website](#)

a few monolayers at the surface. This is used to determine the epitaxial growth mode and surface reconstruction. We utilize a [kSA 400](#) RHEED monitoring system with a Staib Instruments 12keV electron gun for this purpose. The RHEED pattern image capturing can be triggered at chosen azimuths during wafer rotation, thus permitting reconstruction monitoring at several azimuths during the growth.

### **Ex situ characterization**

There are two surface imaging tools immediately available in our lab. First of them is a “black box” (BB) photography setup that consists of a black box, a photo camera and a remote flash. The sample of interest is placed inside the black box and photographed with high exposure and short exposure time. A very strong sensitivity to light scattering, characteristic of this approach, allows to reveal slightest irregularities in the sample surface structure. The second tool is a Nomarski differential phase contrast microscope. It can produce images of the samples with enhanced contrast, determined by the difference in optical paths of orthogonally polarized beams passing through an anisotropic crystal. This microscopy technique features a tremendous vertical resolution on the order of nanometers to expose surface imperfections.

For a further quantitative analysis of surface morphology and sample cross section, we use the methods summarized in table 2.1. The cross-sectional studies done at McMaster University additionally required preparation of thin lamellas. This was done with the Xe<sup>+</sup> plasma focused ion beam (FIB) facility Helios G4 by Thermo Fisher Scientific.

Name	Working principle	Suitable for	Tool used	Tool location
AFM Atomic force microscopy	Scans the surface with a probe sensitive to molecular forces. The vertical coordinates of the probe give the surface map	Determination of the vertical relief of the surface with atomic precision	Bruker Icon Fastscan AFM	University of Waterloo
SEM Scanning electron microscopy	Obtains a contrast image by measuring the secondary emission current across the surface	Surface and cross-sectional studies of conductive samples	JEOL JSM-7200F	
STM Scanning tunneling microscopy	Measures the tunneling current across the surface to resolve its morphology up to an atomic level		Omicron STM	
HAADF STEM High-angle annular dark field imaging, scanning transmission electron microscopy	Scans a thin specimen with an electron beam and measures the scattering of the transmitted electrons with an annular dark-field detector	Cross-sectional studies with atomic resolution	FEI Titan 80-300	Canadian Center for Electron Microscopy, McMaster University
EELS Electron energy loss spectroscopy	Locally determines chemical composition from the energy spectrum of inelastically scattered electrons		Gatan spectrometer embedded in Titan STEM facility	

Table 2.1: Summary of the employed characterization techniques.

## 2.3 Kinetics of aluminum growth on semiconductors

### 2.3.1 Effects of crystal structure and symmetry

#### Bulk parameters

Aluminum is known to have a face-centered cubic crystal structure at room temperature (RT). The majority of III-V semiconductors have zinc blende (face-centered cubic) or wurzite (hexagonal) crystal structures, and occasionally rock salt (face-centered cubic). This review will cover the growth on zinc blende crystals only. When comparing the lattice constants of aluminum and III-V compounds (tab. 2.2), one can easily notice that the value of Al scaled by a factor of  $\sqrt{2}$ :  $a(\text{Al}) \cdot \sqrt{2} = 5.7163$ , is close to the values of III-V compounds. The factor of  $\sqrt{2}$  arises when two cubic crystal lattices are rotated by  $45^\circ$  with respect to each other. Therefore, it is natural to expect that Al[100], rotated by  $45^\circ$  (we denote it as [100]R45) will be a dominant growth direction on (100) III-V substrates or buffers.

	GaAs	InAs	InSb	InP	Al
Lattice constant, Å	5.6533	6.0583	6.4794	5.8667	4.042

Table 2.2: Lattice constants of some zinc blende III-V compounds, and Al.

Nevertheless, both early and recent studies on GaAs (100) substrates demonstrate at least three growth directions of the Al layer with variable quality: [100]R45 [30, 34], [110]R45 [32, 34, 35], and [111] [36]. Furthermore, in the case of [110]R45 orientation, atoms are in 1-to-1 registry only along  $[1\bar{1}0]$  axis of GaAs surface, whereas the lattice match is good only every 4 unit cells (7 cells is a better approximation) of Al along [110] axis. However, no  $4\times$  or  $7\times$  diffraction pattern is observed.

This indicates that the knowledge of bulk crystal parameters is not enough to predict the growth of Al on III-Vs, and other factors should be considered.

#### Surface reconstruction

For MBE growth, it is also important to take into account the structure of semiconductor surface. In most cases, the surface reconstructs into patterns with the symmetry and stoichiometry different from the bulk. In particular, the studies on GaAs (100) [34] show

that on the As-stabilized ( $2 \times 4$ ) and Ga-rich ( $4 \times 6$ ), aluminum forms along a well-defined  $[110]R45$  or  $[100]R45$  direction, respectively, whereas the As-rich ( $4 \times 4$ ) favors the formation of grains of both types. This can be understood from the symmetry considerations. The ( $4 \times 4$ ) reconstruction has high enough symmetry (2-fold rotation & 2 mirror planes) to allow aluminum migration along both  $\langle 110 \rangle$  axes within GaAs (100) surface, leading to the Al grain formation. Conversely, the low-symmetry reconstructions effectively fix the Al orientation, and thus are generally better suited for the growth of monocrystalline Al films on GaAs. However, it is worth noting that the effect of surface reconstruction has not been extensively investigated in the recent literature on InAs and InSb and thus is yet to be understood.

### 2.3.2 Atomic transport

#### Temperature-driven diffusion

In works [33], [34], Al was grown on differently reconstructed GaAs surfaces at RT and 400°C. With the aid of Auger electron spectroscopy, the authors observe significant arsenic diffusion for  $\sim 50$  Å up the Al layer at high temperatures, and no As penetration above  $\sim 5$  Å at RT. It turns out that Ga diffusion may or may not happen at RT and is surface reconstruction-dependent, which indicates that the temperature is not the determining factor of group-III diffusion.

This means that using low enough temperatures suffices to at least inhibit the contamination of metallic layer with group-V elements. The recent reports on GaAs- [37], InAs- [36, 38, 39], and InSb-based [40, 41] heterostructures metallization confirm this with the cross-sectional electron energy loss spectroscopy (EELS). In all cases, the authors cool down samples overnight before the deposition and use additional methods (if applicable) to reach subzero temperatures, with  $-40^\circ\text{C}$  [40] being the lowest value reported.

#### Group-III exchange

The works [33], [34] provide an important observation on the Al growth on GaAs (001) at RT: the Al layer contamination is negligible when GaAs reconstructs into As-stabilized ( $2 \times 4$ ), whereas the Auger peak of gallium persists up to 1000 Å of Al in case of the Ga-rich ( $4 \times 6$ ) reconstruction. This dramatic difference emphasizes the crucial role of the surface composition and bond structure in determining the Al growth. Indeed, the ( $2 \times 4$ ) surface, abundant in arsenic, forms strong covalent bonds both with Ga from the underlying layers and the first Al monolayer (ML). On the contrary, the gallium-rich ( $4 \times 6$ ) reconstruction

can form only weak metallic bonds with Al. The bonds are also less directional and thus not as good at defining the Al layer orientation.

A crude calculation done in [33] suggests that the exothermic energy release due to aluminum cluster formation is small ( $\approx 1$  eV) on As adsorption sites and significant ( $\approx 2.5$  eV) on Ga sites. This amount of energy is enough to activate a replacement (or exchange) reaction between Ga and Al, which is the driving force behind the Ga proliferation from the Ga-rich surface to the top of Al layer.

Therefore, strong covalent bonds due to the group-III elements at the surface inhibit group-V exchange reactions, thereby protecting the material purity and interface abruptness. Recent studies on InAs and InSb-based structures take advantage of this by adding thin interlayers that provide strong bonds at the interface. In particular, the work [36] showcases a remarkable improvement in the metal-semiconductor interface quality ( $\sim 5$  ML roughness), average width of Al islands, and defect formation suppression by depositing 1.5 Å, 0.7 Å, and 0.3 Å of AlAs on an InAs buffer. The same group reports an even better improvement (down to 1 ML roughness) with AlSb interlayers of thicknesses ranging between 0.8-50 Å on a GaSb buffer [41]. Monocrystalline aluminum grows along [110]R45 in both cases.

The choice of Al-based compounds for the interlayers in these works [36, 41] is very natural because no exchange reaction is possible in principle between them and metallic aluminum. However, GaAs interlayers on top of InAs [36, 39] and InGaAs [38, 39] also yield high-quality interfaces, and 2 MLs of InAs on the InSb buffer is explicitly shown to prevent interface degradation for more than a year [40]. This proves that the composition of the top MLs is not always crucial in achieving sharp interface and securing the unidirectional and low-dislocation growth of Al provided that the covalent bonds are strong enough. The cross-sectional imaging in all these studies is done with transmission electron microscopy (TEM, see fig. 2.2 for an example).

### 2.3.3 Strain and energetics

The energetics of surfaces and interfaces requires special attention, as they are very important sources of strain. The surface energy of an Al film is determined by its growth direction, with [111] corresponding to the lowest energy. This means that a sufficiently low energy of an aluminum-semiconductor interface and low strain in the buffer [38] should favor the monocrystalline Al formation along [111].

In general, the interplay of interfacial, surface and defect formation energies are hard to harness. For instance, the work [41] demonstrates the pristine interface between 25 nm



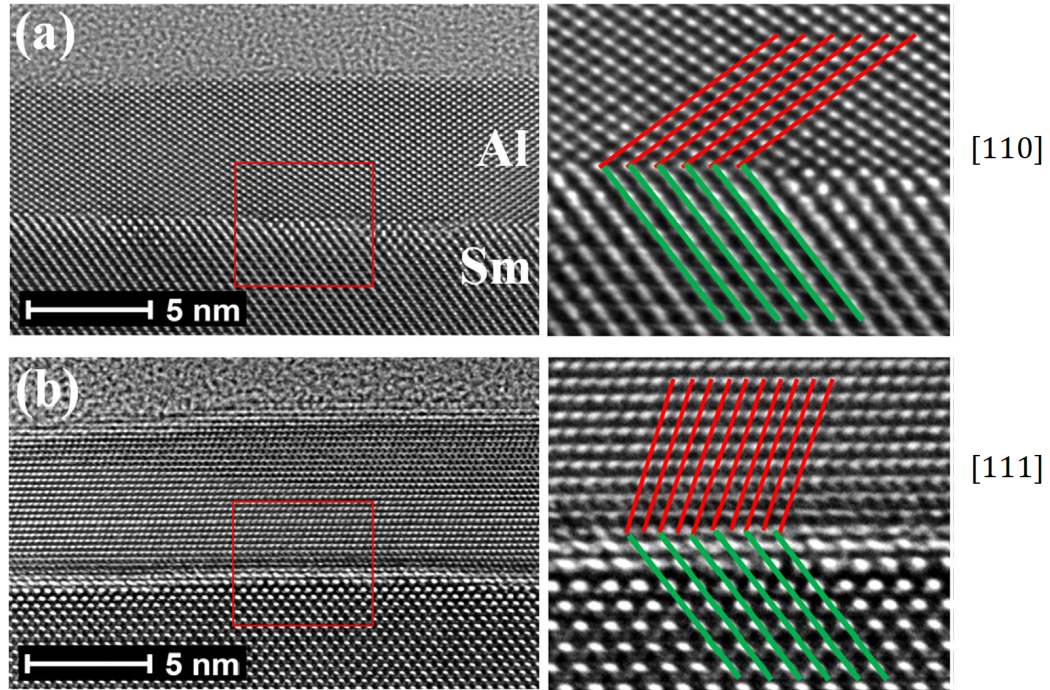


Figure 2.2: Aluminum grains at the lattice constant threshold value  $a=5.98 \text{ \AA}$  corresponding to the two possible Al growth modes, resolved with STEM in work [39]. (a) 1-to-1 registry (low interface energy) between Al and InGaAs, corresponding to [110] Al growth direction (high surface energy). (b) Mismatch in registry (high interface energy), and [111] Al growth direction with low surface energy.

of AlSb and Al, whereas 50 nm of AlSb lead to the Al film full of threading dislocations and Moire fringes, despite the fact that the AlSb critical thickness on GaSb is  $\sim 200 \text{ nm}$ . The reason for this unexpected strain imbalance remains to be identified. Nevertheless, the work [39] offers profound insight into the link between the lattice constant of the top semiconductor buffer, strain character in the Al film and its growth direction. The authors analyze a broad spectrum of buffer layers with different lattice constants  $a$  ranging from  $5.87\text{-}6.10 \text{ \AA}$ , and report the formation of tensely strained [110] Al for  $a < a_s = 5.98 \text{ \AA}$ , and compressively strained [111] Al for  $a > a_s$ . The STEM scans at  $a = a_s$  (fig. 2.2), when grains of both type form, reveal that the existence of the threshold value  $a_s$  is a manifestation of the surface and interface energy competition. It is worth noting that there is no obvious way to relate this value to the lattice parameter of bulk Al (see subsec. 2.3.1), which emphasizes the significance of strain contribution to the growth mode.

## 2.4 Realization of heterostructure with flat Al layer and sharp interfaces

### 2.4.1 Statement of experimental problem

The results from the literature presented in section 2.3 shed light on most mechanisms that influence the Al formation on III-V semiconductors; however, some of them are yet to be understood. In particular, the effect of deposition rate on the growth is almost not investigated in the literature. The only trustworthy resource for the thinnest films [33] reports no dependency of Al quality/ growth direction on the growth rate in the range of  $0.02 - 0.4 \text{ \AA/s}$ , and this information is insufficient to make any conclusions. Furthermore, no other means of protecting the Al surface except controlled oxidation [38, 40] has been reported. The field would benefit from the investigation how else the Al layer can be terminated, and how well this approach protects the layer flatness.

To understand the effects of deposition rate and surface capping, we conduct a series of MBE growths and investigate them with various in situ and ex situ tools. We grow all our structures on quarter-3" InP wafers (fig. 2.3). For all such substrates, the primary flat cut (bottom right) lies in  $(0\bar{1}\bar{1})$  plane, whereas the secondary flat (left) lies in  $(0\bar{1}1)$ . For consistency, the layer structure is chosen to be the same for all our growths, with the only possible difference being the substrate doping (n+ or semi-insulating). This design is presented in table 2.3. Doped substrates are required for the normal operation of STM, whereas semi-insulating ones are better suited for temperature measurements with BET.

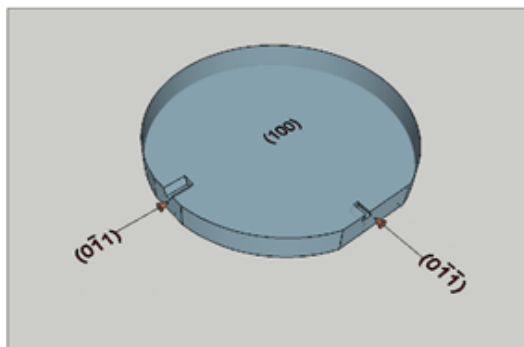


Figure 2.3: Full InP (100) wafer, with the in-plane crystallographic directions. We use quarters of such wafers for all experiments.

As cap (amorphous), $\sim 10^1 - 10^2 \text{ nm}$
Al, 10 nm
$\text{In}_{0.75}\text{Ga}_{0.25}\text{As}$ , 10 nm
$\text{In}_{0.53}\text{Ga}_{0.47}\text{As}$ (lattice-matched), 300 nm
InP substrate (600 $\mu\text{m}$ ): Fe (semi-insulating) doping, <i>or</i> S (n+) doping

Table 2.3: Heterostructure design adopted for all our MBE growths.

Once the oxide is thermally desorbed from InP, its surface is capped with a 300 nm buffer layer of a lattice-matched  $\text{In}_{0.53}\text{Ga}_{0.47}\text{As}$ . The values for thickness  $d$  and composition  $x$  of the top semiconductor buffer  $\text{In}_x\text{Ga}_{1-x}\text{As}$  —  $d = 10$  nm with  $x = 0.75$  — are adopted from the reference [2]. In this article, two such layers form a sandwich structure with an InAs layer in between. This design improves the electron mobility in the InAs quantum well up to  $10^6$   $\text{cm}^2/(\text{V}\cdot\text{s})$ . This is precisely what we want to achieve in the long run, when epitaxially grown structures with aluminum layers on top will be used for Majorana-hosting devices. In our test structures, outlined in table 2.3, we only aim to optimize the growth conditions of the top layers and interfaces, and thus do not require an InAs quantum well. The aluminum layer thickness is borrowed from the pioneering work [38] in the field of heterostructure-based Majorana qubits. Because of the high surface atomic mobility of aluminum, it is critical that it be deposited at the lowest possible temperature to achieve 2D smooth epitaxy. For this, after we finalize semiconductor parts of each growths, we eliminate all non-essential sources of heat and leave the sample in the growth module to cool down overnight.

For the surface protection, we choose to deposit a layer of amorphous  $\text{As}_4$ . This approach has been used to protect the surfaces of epitaxially grown semiconductors from oxidation and contamination in between depositions. For example, Luo et al [42] employed this method to transfer a GaAs-based heterostructure to another UHV chamber with an Al cell and a scanning tunneling microscope. The sample was then kept at  $300^\circ\text{C}$  for several hours to desorb arsenic and subsequently deposit an Al layer. To our best knowledge, however, this method has never been applied to the surfaces of *aluminum* layers. With the As source being readily available in our MBE system, its successful use for capping will eventually enable us to fabricate high-quality, uncontaminated superconductor-semiconductor devices. Together with the sharp metal-semiconductor interfaces, this is crucial for the successful detection and control of Majorana zero modes.

## 2.4.2 Surface flatness and layer structure confirmation

### Sample growth

To experimentally pursue the epitaxial growth of heterostructures with high-quality metal-semiconductor interfaces, we grow two samples, designated as G0680 and G0697. The only difference in their composition is the substrate doping: semi-insulating in G0680, and n+ in G0697.

The growth procedure for the semiconductor part is conventional, and includes oxide desorption of the InP wafer, soak with As<sub>2</sub> to prevent its desorption from the surface, successive deposition of the lattice-matched In<sub>0.75</sub>Ga<sub>0.25</sub>As, and then the indium-rich In<sub>0.53</sub>Ga<sub>0.47</sub>As buffers. The cell temperature and flux parameters for G0680 are summarized in table 2.4. In1 and Ga2 are the names of the cells used for the deposition, and BEP denotes beam-equivalent pressure. The growth rate for both InGaAs layers is chosen to be 2.5 Å/s. A completely analogous procedure for the semiconductor layers growth was used in all experiments presented in this thesis, with the values of cell temperatures, fluxes and pressures being possibly different from the ones given in table 2.4.

Material	x	Ga2 tip temp. (°C)	Ga2 base temp. (°C)	Ga2 flux (cm <sup>-2</sup> s <sup>-1</sup> )	Ga2 BEP (Torr)	GaAs-only equivalent growth rate (Å/s)
In <sub>x</sub> Ga <sub>1-x</sub> As	0.526	1053.7	903.7	2.3439E+14	2.1900E-07	1.1019
In <sub>x</sub> Ga <sub>1-x</sub> As	0.750	1022.7	872.7	1.1988E+14	1.1351E-07	0.5636
Material	x	In1 tip temp. (°C)	In1 base temp. (°C)	In1 flux (cm <sup>-2</sup> s <sup>-1</sup> )	In1 BEP (Torr)	InAs-only equivalent growth rate (Å/s)
In <sub>x</sub> Ga <sub>1-x</sub> As	0.526	953.4	793.4	2.6011E+14	2.7791E-07	1.4032
In <sub>x</sub> Ga <sub>1-x</sub> As	0.750	967.6	807.6	3.5964E+14	3.8172E-07	1.9402

Table 2.4: In1 and Ga2 cell flux parameters for the growth of two InGaAs buffers in G0680.

After the top InGaAs layer was finalized, we closed the main shutter, positioned right under the wafer, and left the sample in MBE chamber to cool overnight. We managed to reach lower temperature for G0680 (thermocouple reading around 0°C) than for G0697 (about 6–7°C). It also manifested itself in a sharper RHEED pattern during the subsequent deposition. In these two initial experiments, samples were rotated during Al growth to achieve better uniformity. The Al layers on both samples were grown at 3 Å/s. The RHEED pattern was used mainly as a guide when to stop supplying arsenic at the final stage of the deposition (streaks begin to disappear when the surface becomes amorphous). Unfortunately, we have no means to measure the thickness of arsenic cap in situ; we only expect it to be thicker on G0680 than on G0697 because we waited for longer.

## Surface morphology

The “black box” (BB) photos of the two samples are given in figure 2.4. They reveal the unexpected influence of the RHEED beam on the surface. We attribute the circular pattern of G0680 to the effect of the misaligned RHEED beam on the As coating, or the way As sticks to the surface: the area is rough wherever the RHEED beam hit the sample and is smooth where it did not. We speculate that the formation of mirror-like and rough areas on G0697 is related to the malfunction of the main shutter. Presumably, it did not close properly before or after the growth, so that the smooth part is where the shutter properly shields the wafer.

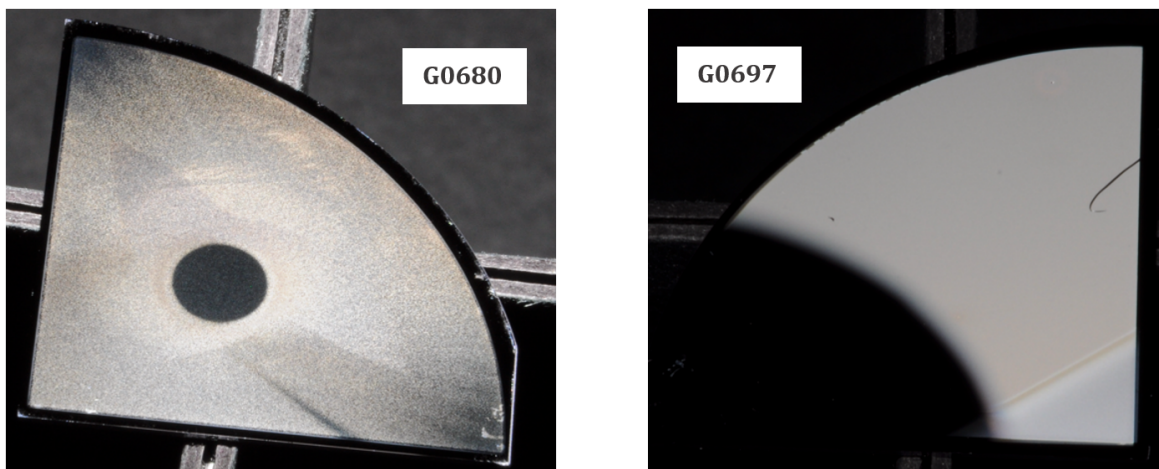


Figure 2.4: BB photos of G0680 and G0697 that reveal two distinct areas on each wafer. The effect is attributed to the exposure to a misaligned RHEED beam.

Yet, the subsequent morphology study confirms a good level of flatness both inside (mirror-like area) and outside the circle (rough area) of G0680. The corresponding AFM scans are shown in figure 2.5. The root mean square (RMS) roughness of the surface  $\sim 1.3$  nm both inside and outside the bright circle. The height of point defects that consist of a pit and two hills on the sides (framed) inside the circle is around 4 nm. The distance between neighboring defects in both regions is on the order of 5–10  $\mu\text{m}$ .

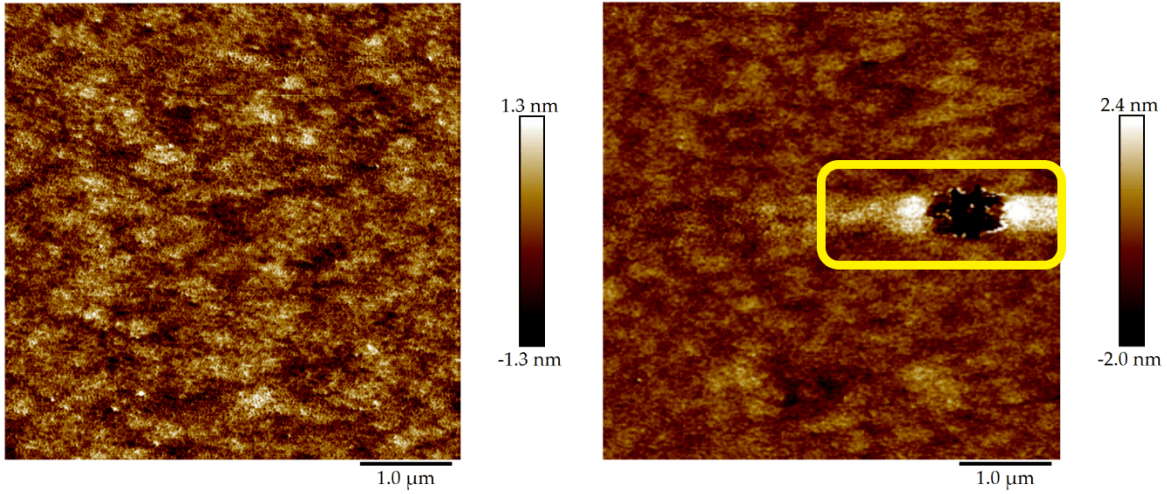


Figure 2.5: AFM micrographs of the mirror-like (left) and hazy areas (right) of G0680. Surface point defects (framed) of this kind are seen all across the sample.

### Layer structure determination

Next, we attempted to discern the Al and other thin layers in G0697 with the cross-sectional scanning tunneling microscopy (the STM on G0680 was not possible because of its semi-insulating substrate). The sample was transferred to the STM facility and cleaved in situ at UHV ( $\sim 10^{-10}$  mbar). On the  $300\ \mu\text{m}$ -wide scan in the constant current mode (left of fig. 2.6), a border between two distinct patterns (blue arrow) stands out. This is the indication of the  $\text{In}_{0.53}\text{Ga}_{0.47}\text{As}$  / InP (substrate) interface, which was later resolved at higher resolution (right of fig. 2.6). Atomic terraces are conspicuous over the entire scan area, which confirms high-quality cleaving of the semiconductor part of the growth.

Unfortunately, the cleavage plane was getting more and more curved towards the edge, and bright spots started appearing on the scans. We now attribute these effects to the fact that aluminum is very soft compared to III-V compounds and thus cannot cleave smoothly. Another suspicion was that the amorphous region beside the edge is due to As cap. In order to desorb it, we kept the sample at  $400\ \text{°C}$  in the STM preparation chamber for about 30 minutes. Further measurements reveal that the surface significantly rearranges (fig. 2.7). First of all, triangular cleavage planes transform into a “camouflage” pattern, albeit remaining only a few atomic layers thick. The corresponding planes of  $\text{In}_{0.53}\text{Ga}_{0.47}\text{As}$  coalesce and form terraces elongated perpendicularly to the scan direction. Unfortunately, the region near the surface remained significantly uneven and did not allow for scans. Therefore, since no layers except the substrate and the lattice-matched  $\text{In}_{0.53}\text{Ga}_{0.47}\text{As}$  have

been resolved, we conclude that STM is of little utility to the cross-sectional studies of aluminum-metallized heterostructures.

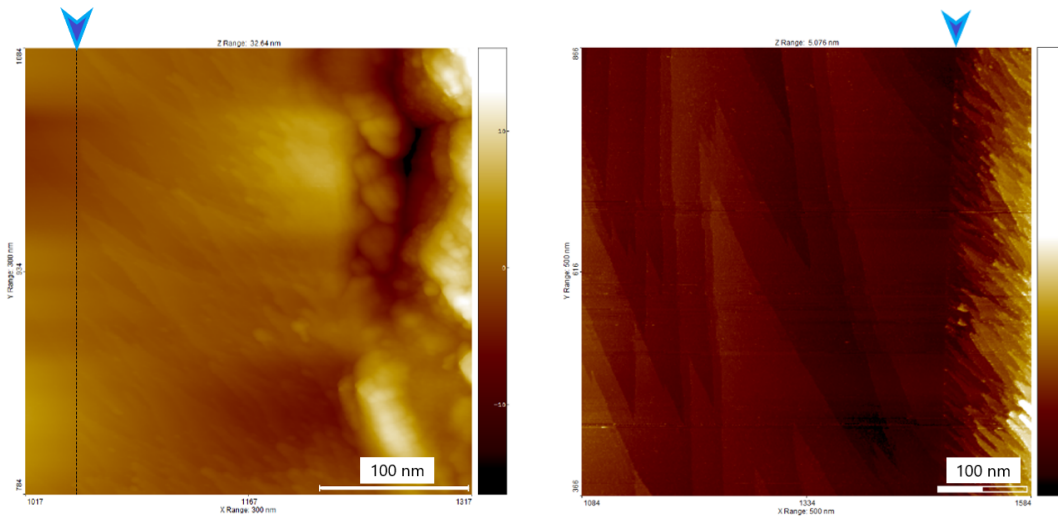


Figure 2.6: STM scans of G0697: near the surface (left), and at the  $_{0.53}\text{Ga}_{0.47}\text{As} / \text{InP}$  interface (right). The scanning windows are 300 and 500 nm, respectively. The position of  $\text{In}_{0.53}\text{Ga}_{0.47}\text{As} / \text{InP}$  interface is indicated with blue arrows.

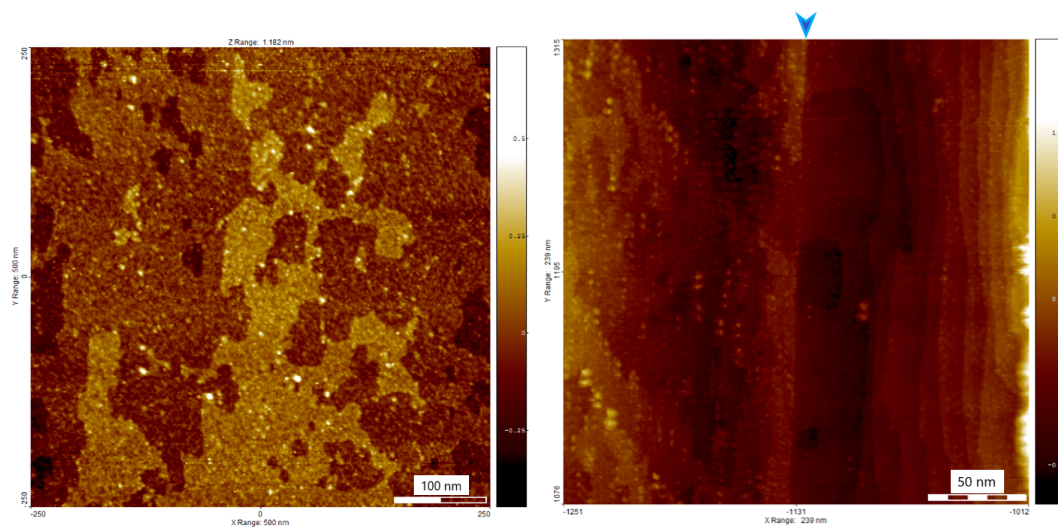


Figure 2.7: Surface after annealing at 400 °C for 30 min, resolved with STM. Left: region deep in the substrate (500 nm wide scan); right: 100 nm wide scan near the  $\text{In}_{0.53}\text{Ga}_{0.47}\text{As} / \text{InP}$  interface, indicated with a blue arrow (cf. fig. 2.6).

The STM measurements of G0697 were followed by cross-sectional scanning electron microscopy (SEM). The sample cleaved well in most places and was flat with the features at the top. Scanning with SEM (fig. 2.8) happened to resolve the layers clearly (horizontal green lines) and yield very good estimates of the layer thicknesses. The value for  $\text{In}_{0.53}\text{Ga}_{0.47}\text{As}$  (301 nm) from fig. 2.8a perfectly agrees with the adopted heterostructure design from table 2.3. The n+ doping of the substrate gives a good contrast and thus proves to be beneficial in this experiment. Also, we finally managed to estimate the As cap thickness to be on the order of 200 nm for G0697 (fig. 2.8b). Remarkably, a very thin  $\sim 20$  nm layer was resolved at x100K magnification (fig. 2.8c). Yet, it was not possible to identify whether it was Al,  $\text{In}_{0.75}\text{Ga}_{0.25}\text{As}$  or both. This scan also reveals the flaky structure of the As cap in some places.

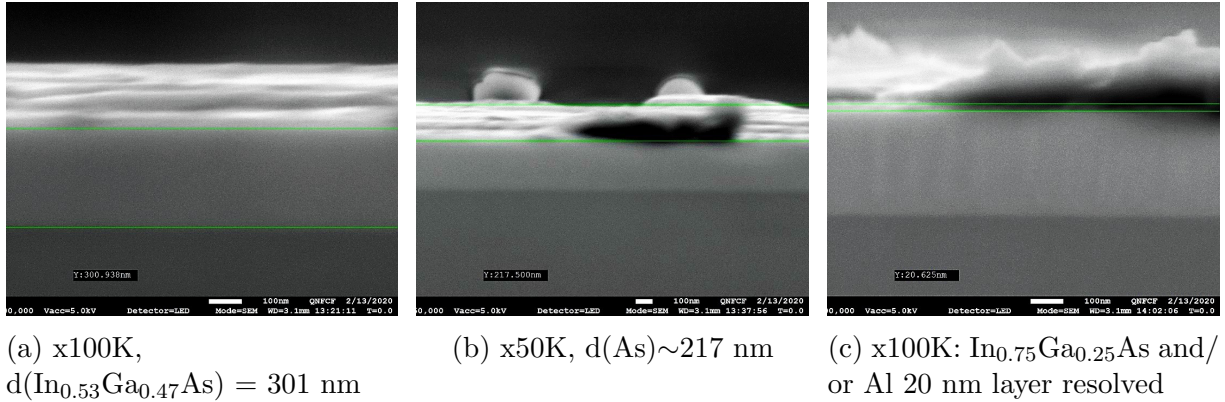


Figure 2.8: Layer thickness measurements with cross-sectional SEM on G0697.

### 2.4.3 Cross-sectional microscopy and spectroscopy with atomic resolution

The subsequent cross-sectional studies with STEM (scanning transmission electron microscopy) and EELS (electron energy loss spectroscopy) tools, hosted in one UHV chamber, revealed the layer structure of our epitaxial growths with atomic precision.

Before the experiments, thin lamellas were machined using the  $\text{Xe}^+$  Focused Ion Beam (FIB) technique. The lamellas were extracted from the flat, feature-free areas on top of both samples. Figure 2.9 shows an  $\sim 12\mu\text{m}$  wide lamella for G0697, placed into a copper frame. The thickness of the lamella is on the order of 80 nm — sufficiently small to provide electron transparency.



## Imaging of G0680

G0680 sample was studied first. A low-resolution image 2.10 confirms the uniformity of the layer structure on a micron scale. As in SEM previously, the contrast between InP and  $\text{In}_{0.53}\text{Ga}_{0.47}\text{As}$ , lattice matched to it, is high. The area with the thin  $\text{In}_{0.75}\text{Ga}_{0.25}\text{As}$  and Al layers is discernible by bare eye under a dark,  $\sim 70$  nm layer of tungsten carbide, initially deposited onto the lamella to protect the surface from damage. The brightest part at the top is a remainder of platinum (Pt), which acted a solder for a tungsten needle used to extract the lamella from the bulk wafer.

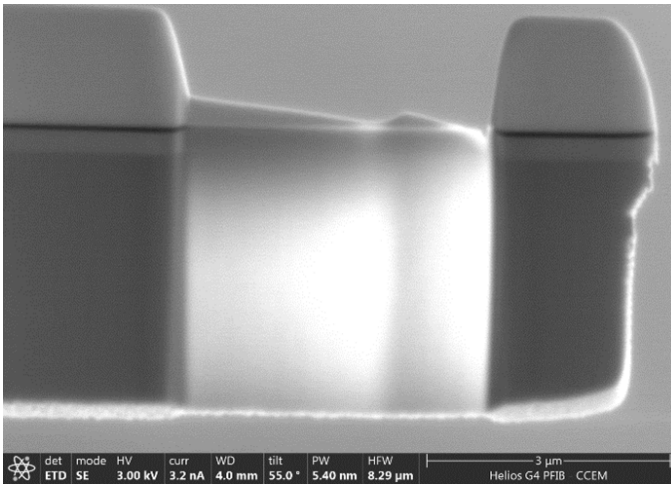


Figure 2.9: Thin lamella machined with FIB for G0697.

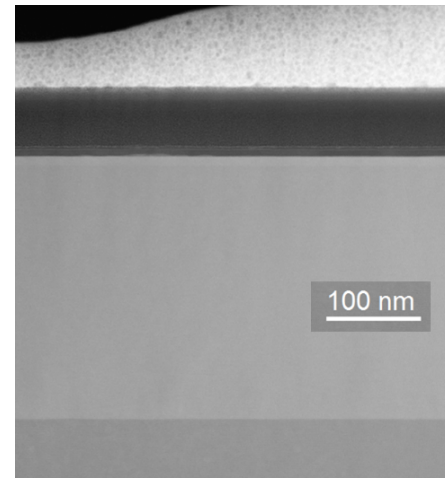


Figure 2.10: TEM with a 1 nm resolution confirms the flatness of G0680 layers on a  $\mu\text{m}$  scale.

The high resolution STEM and EELS scans for G0680 are presented in figure 2.11. The window of measurement is chosen to make visible all layers starting from  $\text{In}_{0.53}\text{Ga}_{0.47}\text{As}$  up to the onset of tungsten carbide deposit. First of all, we conclude that the elemental composition is in agreement overall with the expected layer structure (tab. 2.3). The other results are the following:

- The thickness of the Al layer ( $\sim 9$  nm) is consistent with our calibrations. The thickness of As cap is about 8 nm;
- In the STEM micrograph, the top of As layer is rough and appears to pile up out of the plane of the lamella;

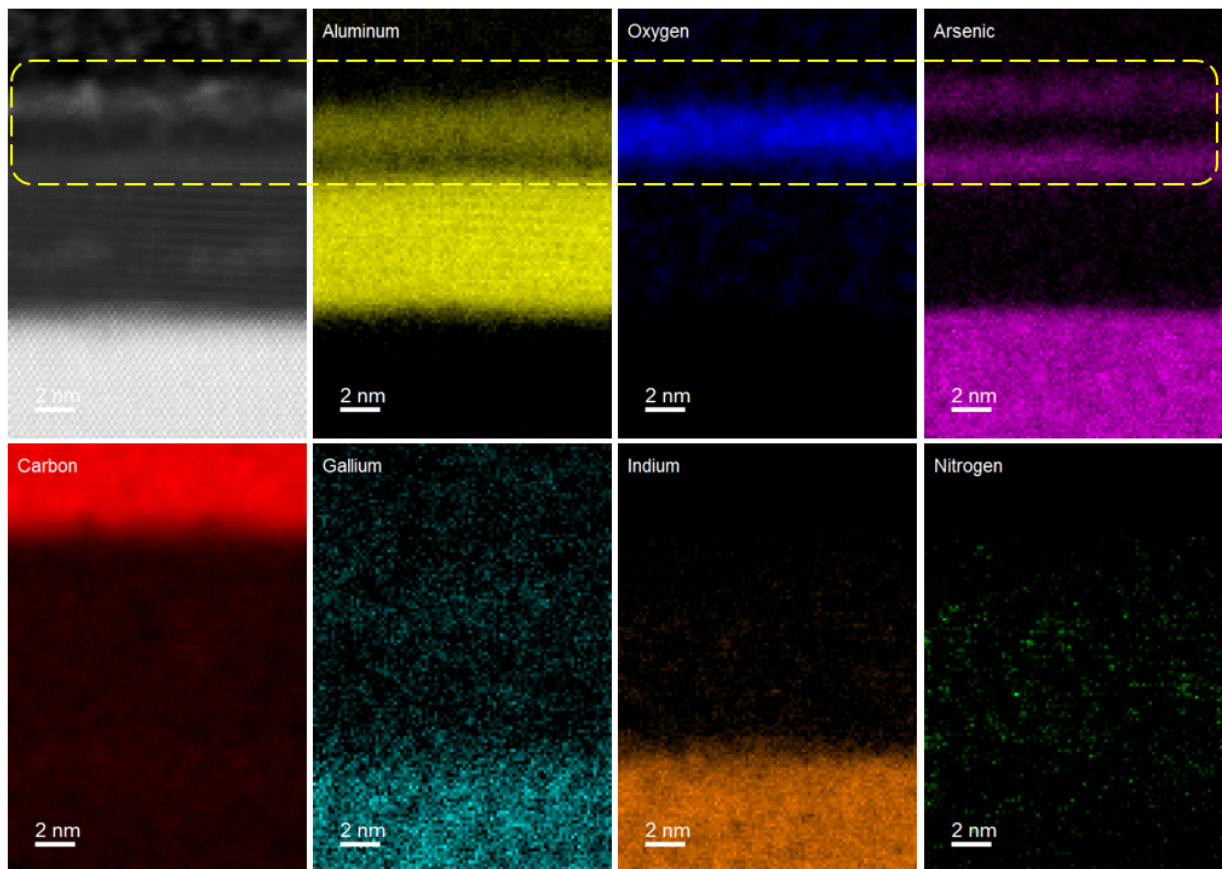


Figure 2.11: TEM and EELS scans with 0.15 nm resolution, with the highlighted  $\text{AlO}_x$  region inside the As cap layer.

- The chemical composition within the As capping layer is quite unexpected. Scans in different regions of the sample consistently show that an aluminum oxide  $\text{AlO}_x$  layer forms in the middle of it (framed area in figure 2.11). It is also noticeable as a darker area in the STEM scan;
- As oxidizes neither above nor below the  $\text{AlO}_x$  layer; neither it does below the lower part of As. This means that although we do not completely understand the formation of  $\text{AlO}_x$ , it is possible in principle to protect the main Al layer from oxidation with an As cap;
- The average interdiffusion depths of Al & InGaAs, and Al & bottom of As is about 1 nm, which proves sharpness of both interfaces;

- Gallium spectrum does not look abruptly terminated at the bottom of Al layer, indicating a non-negligible group-III exchange.

Additional conclusions can be made from the high-resolution STEM scans that resolve areas near Al-InGaAs and Al-As interfaces, shown in figure 2.12:

- STEM confirms a very sharp and smooth interface between Al and InGaAs. The Al-As interface is also good but definitely rougher, and there are signatures of Al mounts not completely leveled off in certain areas;
- We notice blurry regions in the middle of Al layer (central figure) over a wide range across the sample. Since they do not spoil the Al crystal structure, we attribute them to oxide patches, residues of FIB preparation, or imperfect sample cleaning that followed it;
- $\text{AlO}_x$  layer is discernible since it is darker than any other layer in the scan except carbon at the top (right figure), but neither its crystal structure nor morphology is visible.

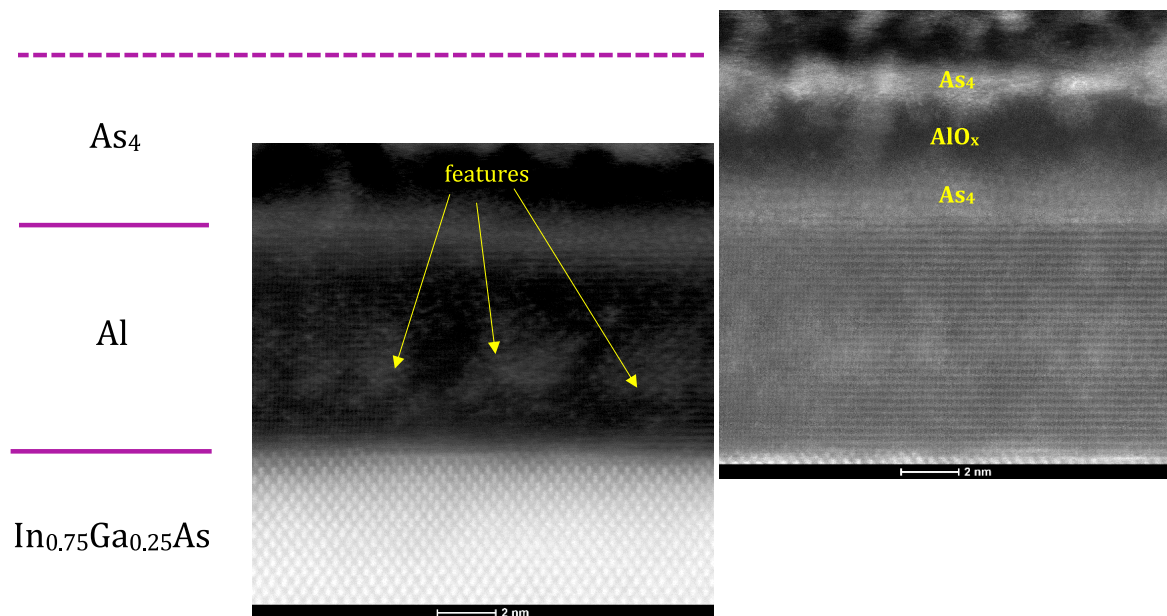


Figure 2.12: Expected layer structure (left), compared to the STEM micrographs of G0680 in the areas around Al layer (center and right).

## Imaging of G0697

The low-resolution STEM scan of G0697 (fig. 2.13) shows its significant nonuniformity on a micron scale and thus lower quality compared to G0680. In addition, the EELS spectra from figure 2.14 reveal alternating clusters of In and Ga within Al layer, which has a well-defined interface with InGaAs nonetheless. This effect was completely absent from G0680, where In concentration above the top InGaAs layer was negligible (cf. fig. 2.11). This illustrates the need for a more stringent control of the epitaxy. The mechanisms that underpinned this growth dynamics were not understood; we can only speculate about the effects of FIB preparation, and implications of higher temperature during Al and As deposition compared to G0680. Indeed, the G0697 wafer temperature at the beginning of Al deposition was higher, and the radiative heat transfer to its n+ doped substrate was significantly more pronounced.

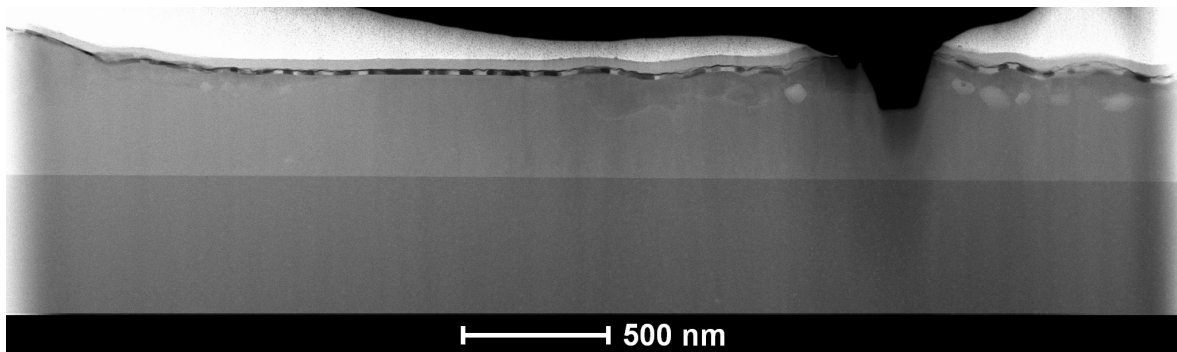


Figure 2.13: 10 nm resolution STEM scan of G0697 shows its nonuniformity on a  $\mu\text{m}$  scale.

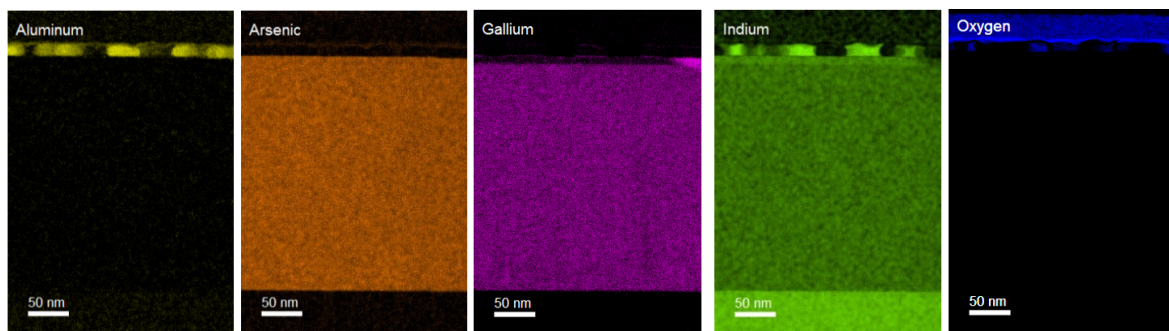


Figure 2.14: EELS of G0697 resolves intermittent In and Ga clusters within Al layer, indicative of significant group-III exchange.

Another important observation is that As cap is virtually non-existent in G0697, which contradicts the  $\sim 200$  nm estimate from SEM on this sample. This effectively shows that the As cap almost fully evaporates at some point before the STEM/EELS experiment, most likely, during the FIB preparation. Therefore, an additional investigation of the arsenic evaporation rate, and possibly, its mechanical protection by some ex-situ deposition, would be beneficial.

## Comparison

The STEM and EELS results presented in this subsection conclusively indicate that we managed to grow a flat aluminum layer with a pristine metal-semiconductor interface only in one case. This indicates that the deposition of a flat aluminum layer is not trivial and is highly dependent on the temperature dynamics during the Al deposition. As the temperatures of the wafer before the deposition, of the Al cells during the deposition, and the total duration of the deposition are the factors that contribute to the total thermal footprint, they all should be thoroughly investigated. Besides, the arsenic capping is shown to be effective only in one of the two experiments, though the chemical processes it undergoes remain obscure. This prompts us to a more comprehensive surface morphology study. The results of both investigations constitute the next section of this chapter.

## 2.5 Deposition rate optimization and surface protection for low-temperature growth

### 2.5.1 Choice of growth parameters for investigation

In the previous section, we unambiguously demonstrated the growth of a flat aluminum layer with quality InGaAs-Al interface, and achieved surface protection with capping. A much higher heterostructure quality of G0680 than of G0697 emphasized the need to understand better the influence of ambient temperature and heat sources on the growth. Besides, both depositions were carried out at an extremely high rate ( $3 \text{ \AA/s}$ ). In terms of the aluminum cell operation, this value is equivalent to the growth of a zinc blende compound like AlAs at  $6 \text{ \AA/s}$ . This rate approaches the relative upper limit that does not jeopardize the long-term performance of aluminum cells. Using lower values is generally preferable but is not guaranteed a priori to give the same layer structure quality. Therefore, our next goal is to thoroughly investigate every stage of the epitaxial growth and the evolution of the wafer surface with or without arsenic capping for varied deposition rates. This will produce more insight into the process of layer and interface formation, collectively influenced by the speed of deposition and temperature input into the system.

Table 2.5 summarizes the key parameters of five new heterostructures we have grown for this purpose. All of them are based on a semi-insulating InP substrate, follow the same layout and procedure of semiconductor buffer deposition as described in subsection 2.4.1. Now, we use two Al cells instead of one, and choose three distinct deposition rates that both cover the conventional range of values and go beyond it.  $0.1$  and  $0.5 \text{ \AA/s}$  for our growths roughly correspond to the bounds of the typical operable range ( $0.09 \text{ \AA/s}$  [36, 41],  $0.33 \text{ \AA/s}$  [40],  $0.5 \text{ \AA/s}$  [32]), whereas  $2 \text{ \AA/s}$  is much larger than any value reported previously. We expect the range  $0.1 - 2 \text{ \AA/s}$  to span distinct growth regimes if they should be observed. Three of the samples in this batch are capped with amorphous  $\text{As}_4$ , whereas the surfaces of the rest are deliberately left unprotected.

### 2.5.2 Wafer temperature monitoring during the aluminum deposition

For our growths, we have access to two sources of information about the wafer temperature. The first one is thermocouple directly connected to the manipulator that holds the wafer. The second one is the Silicon array spectrometer we calibrated specifically to extract the

Growth name	Growth number	Al deposition rate, Å/s	Capping
G0841	Gr0.1As	0.1	Capped
G0842	Gr0.5As	0.5	Capped
G0843	Gr0.5	0.5	Uncapped
G0844	Gr2.0As	2	Capped
G0847	Gr2.0	2	Uncapped

Table 2.5: A series of growth with varied deposition rates and capping.

InP substrate temperature from the position of its band edge. A broadband light source (halogen lamp), used to obtain the InP transmittance spectrum that gives the band edge, is verified not to cause any noticeable heating of the wafer.

As before, after the deposition of the semiconductor part, the wafers were left in the MBE chamber overnight with all non-essential sources of heat having been eliminated. For all our samples, the manipulator thermocouple temperature decayed with a time constant on the order of 0.5 hours, and stabilized on average over the course of 4-5 hours at the values  $\sim 3 - 7^\circ\text{C}$ . The corresponding BET values for the wafers happened to be higher (on the order of  $22 - 29^\circ\text{C}$ ). Unlike for G0680 and G0697, discussed in section 2.4, the main shutter was not available for our more recent series of growths. As a result, the sample surface was seeing more thermal radiation from the flange with effusion cells. This did not allow to reach temperatures below  $0^\circ\text{C}$ .

The temperature dynamics during the growths is presented in figure 2.15. The temperatures of Al cells are kept constant during depositions; therefore, the radiant power emitted from the cells is deemed constant:

$$P = \sigma (T_1^4 S_1 + T_2^4 S_2). \quad (2.1)$$

Here,  $T_{1,2}$  are the temperatures of the cells,  $S_{1,2}$  are the sizes of the nozzles where aluminum atoms come from, and  $\sigma$  is the Stefan-Boltzmann constant for black body radiation (the emissivity of the cell is assumed to be close to 1):  $\sigma = 5.67 \cdot 10^{-8} \text{ W} \cdot \text{m}^{-2} \cdot \text{K}^{-4}$ .

The radiances of the wafer and a much cooler MBE chamber are negligible compared to the radiance of the hot aluminum cells. Therefore, the only significant source of energy dissipation from the wafer is its thermal conductive coupling to the heat reservoir (chamber) through the manipulator. The constant energy input with one thermal conductivity channel corresponds to a simple first-order (i.e. exponential) temperature process. Therefore, we interpolate the BET readings for the period of Al growth ( $t_1 \leq t < t_2$ ), and the

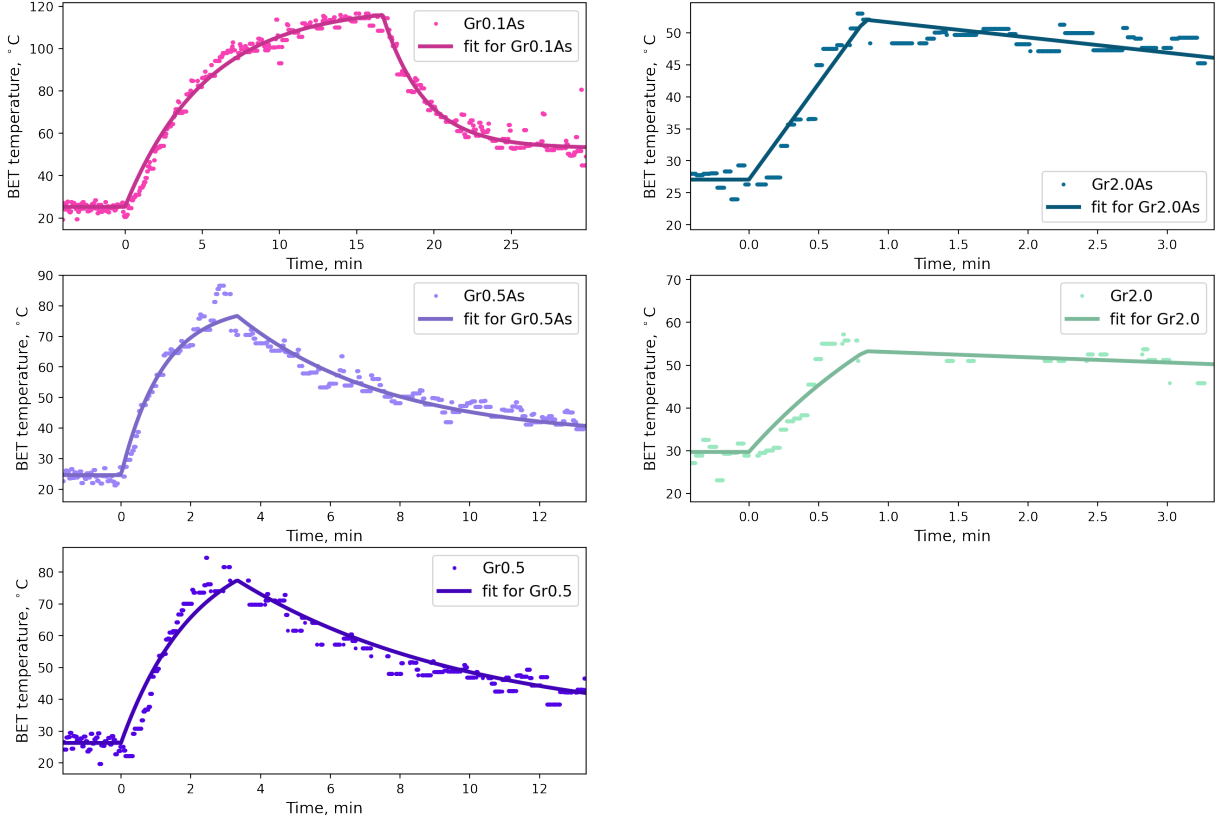


Figure 2.15: BET temperature data with the fit to a first-order model (2.2). Only part of the data, closest in time to the aluminum growth, is shown. The fits are done over time ranges up to 80 minutes.

period after it ( $t \geq t_2$ ), with two exponential functions:

$$T = \begin{cases} T_0, & t < t_1 \\ T_0 + a \left( 1 - \exp\left(-\frac{t-t_1}{\tau_1}\right) \right), & t_1 \leq t < t_2 \\ T_0 + a \left( 1 - \exp\left(-\frac{t_2-t_1}{\tau_1}\right) \right) - b \left( 1 - \exp\left(-\frac{t-t_2}{\tau_2}\right) \right) & t \geq t_2 \end{cases} \quad (2.2)$$

Here,  $T_0$  is the wafer temperature before the Al deposition,  $a$  is the maximum possible increase of the temperature during the growth of Al;  $b$  is the temperature drop after the Al deposition is finished;  $\tau_1, \tau_2$  are thermal time constants of the system before and after the Al deposition, respectively. Such a choice of the function  $T(t)$  ensures that it is continuous both at  $t = t_1$  and  $t = t_2$ . The initial ramp rate during the growth  $q = \left. \frac{dT}{dt} \right|_{t_1} = \frac{a}{\tau_1}$ .



The fitting parameters, extracted from the data, along with the relevant quantities that influence the system temperature dynamics, are presented in table 2.6.

Growth #	Al depos. rate, Å/s	$T_1$ , °C	$T_2$ , °C	Al depos. time	$T_{\max}$ , °C	$q$ , °C/min	Fitting parameters				
							$T_0$ , °C	$a$ , °C	$b$ , °C	$\tau_1$ , min	$\tau_2$ , min
Gr0.1As	0.1	1000.6	1005.5	16m 40s	116	17.9	25.3	94.7	63.0	5.28	2.72
Gr0.5As	0.5	1075.0	1079.9	3m 20s	76.7	46.0	24.6	55.6	39.9	1.21	4.31
Gr0.5	0.5	1075.1	1079.0	3m 20 s	77.4	30.6	26.3	64.3	45.7	2.10	6.66
Gr2.0As	2	1148.7	1149.8	50 s	52.1	299	27.1	1.52e5	1940	5080	8.13e4
Gr2.0	2	1148.8	1144.5	50 s	53.3	36.8	29.7	55.9	1.29e5	1.52	1.06e5

Table 2.6: Temperature dynamics during and after the Al deposition: measured and fitted data.

Here,  $T_1, T_2$  are the temperatures of Al1 & Al2 cells during the Al deposition, respectively, and  $T_{\max}$  is the maximal recorded BET value at the very end of Al deposition. Importantly,  $T_{\max}$  decreases when the Al cell temperatures (and thus its growth rate) increase. To investigate this counterintuitive result closer, we plot in figure 2.16 the measured band-edge temperature versus the cumulative energy output from unit surface area of the molten aluminum in a cell:

$$D(t) = \frac{1}{2}\sigma t(T_1^4 + T_2^4), \quad (2.3)$$

(we assume for simplicity that the areas of the Al1 and Al2 cell nozzles are the same). The different lines are packed very closely together and have almost identical slopes. On the one hand, it means that the simple model of radiative heat transfer (2.3) explains the wafer temperature dynamics very well, and on the other hand, the heat losses to the reservoir are indeed very slow compared to the timescale of the Al deposition. Moreover, short growth duration proves to be a much more substantial factor than the cell temperature in the determination of thermal footprint. For example, despite having a 20x faster Al growth rate than Gr0.1As, Gr2.0 receives an order of magnitude *less* heat from the Al cells and thus undergoes an almost 3 times smaller temperature increase despite the difference in cell temperatures by about 150°C. This proves that shortening the duration of deposition is a viable method to mitigate the wafer heating for all observable growth regimes.

When it comes to the quality of the exponential fit with the expression (2.2), we conclude from the figure 2.15 that it works reasonably well for slower aluminum depositions: Gr0.1As, Gr0.5As, Gr0.5. In all cases, though, it fails to capture a kink at the beginning of Al deposition, being the most pronounced when the growth is the fastest (Gr2.0As, Gr2.0). At the same time, the right branch of the exponential fit (i.e. after the end of aluminum

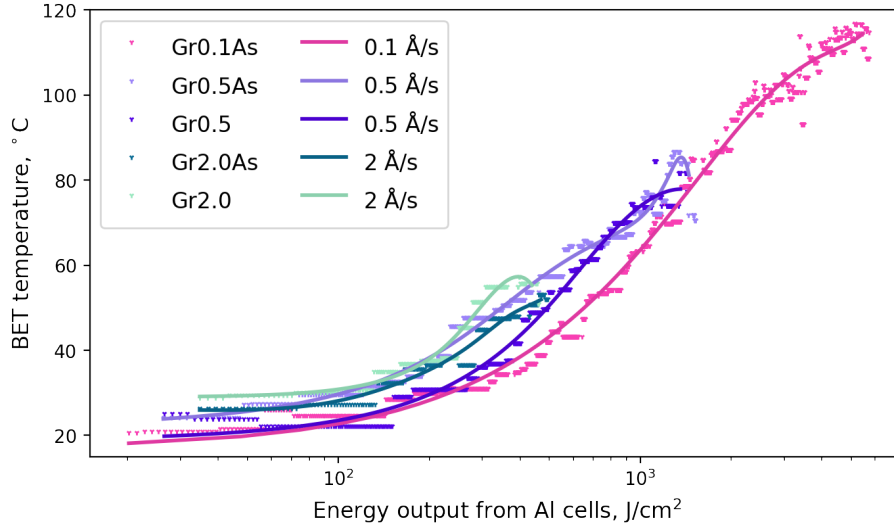


Figure 2.16: Heterostructure temperature measured with BET as a function of the thermal energy outputted from a unit surface area of hot Al effusion cells. The interpolation is done with B-splines using SciPy [43].

deposition) remains good in all cases even for long observation times, not shown in figure. Interestingly, the corresponding time constants  $\tau_2$  (pure energy dissipation without significant heating) differ profoundly for the two groups of growths: on the order of minutes for Gr0.1As, Gr0.5As and Gr0.5 (slower ones) versus days for Gr2.0As and Gr2.0 (faster ones). Essentially, these values:  $\tau_{fast} \sim 2 - 6$  min, and  $\tau_{slow} \sim 10^4 - 10^5$  min, are the time constant estimates for two distinct heat transfer processes. We attribute the faster one to the heat exchange with the manipulator: apparently, the wafer and manipulator are being heated highly unequally during the aluminum growth. The slower process is the energy transfer to the reservoir, which starts to dominate once the wafer and the manipulator reach thermal equilibrium.

### 2.5.3 Evolution of surface reconstruction

#### During the semiconductor layer deposition

To correctly identify the surface reconstructions from the RHEED patterns, we garner information about the possible reconstructions for related semiconductor materials from the literature [44–48]. This data is summarized in table 2.7.

Top layer	Substrate	$1 \times 2$	$1 \times 3$	$2 \times 2$	$2 \times 3$	$2 \times 4$	$3 \times 4$	$4 \times 4$
InP	InP	✓		✓		✓		✓
$\text{In}_{0.53}\text{Ga}_{0.47}\text{As}$	InP					✓	✓	
$\text{In}_{0.27}\text{Ga}_{0.73}\text{As}$	GaAs				✓	✓	✓	
$\text{In}_{0.81}\text{Ga}_{0.19}\text{As}$	InP					✓	✓	
InAs	GaAs	✓	✓			✓		✓

Table 2.7: Surface reconstructions for selected semiconductor heterostructures, reported in works [44–48]

Table 2.8 presents the RHEED patterns at two distinct azimuths, and the corresponding surface reconstructions for Gr0.5As. The same results apply to all other growths, since the semiconductor part of the heterostructure is grown in the same way. One important observation is the  $(2 \times 4)$ -reconstructed surface of the top indium-rich InGaAs barrier, which precedes the aluminum deposition.

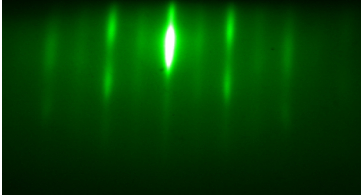
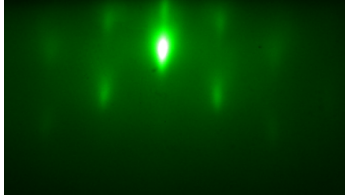
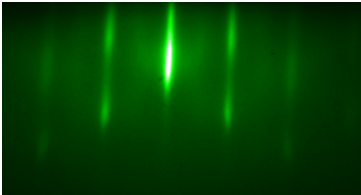
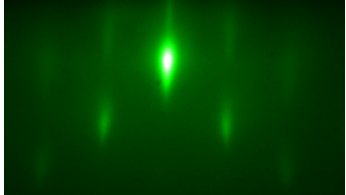
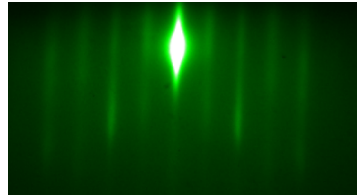
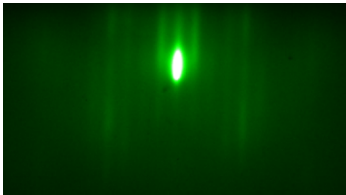
Stage	Reconstruction	$0^\circ$ azimuth pattern	$90^\circ$ azimuth pattern
After oxide desorption of InP substrate	$(2 \times 1)$		
After the growth of $\text{In}_{0.53}\text{Ga}_{0.47}\text{As}$	$(1 \times 1)$ and/or $(2 \times 1)$ : secondary streaks are barely visible		
After the growth of $\text{In}_{0.75}\text{Ga}_{0.25}\text{As}$	$(2 \times 4)$		

Table 2.8: RHEED pattern time evolution during the aluminum deposition on Gr0.5As.

## During the Al deposition

Unlike before (sec. 2.4), we do not rotate the substrate during aluminum deposition. Thus we are hoping to minimize the obscure effect of RHEED beam on the surface observed previously (see left of fig. 2.4). In turn, this limits the RHEED operation to a single azimuth and thus disables us from identifying the surface reconstruction unambiguously. Nonetheless, after the semiconductor growth is finished, we record the azimuth that gives the most pronounced streaks, and reset the substrate manipulator to it in the morning, right before the aluminum deposition.

Despite the fact that the growth rates are very different, the scenario of aluminum layer deposition is the same in all cases. The summary of this process is provided in table 2.9 and is based on Gr0.1As only except for the last stage of RHEED pattern evolution, where a comparison between the slowest and the fastest growths is relevant. The first observation is the change in streak spacing after the overnight cooling, which indicates that the uncapped InGaAs surface reconstructed to  $(1 \times 1)$ ,  $(1 \times 2)$  or  $(1 \times 3)$  over this period of time. At the beginning of Al deposition, we identify the “strained” growth mode (streaks do not change their position). The chemical composition of this part is not definitively identified. However, we speculate that apart from Al nucleation, this may possibly signify the formation of lattice-matched AlAs due to the presence of residual As on the surface adsorbed after the end of  $\text{In}_{0.75}\text{Ga}_{0.25}\text{As}$  deposition. In accordance with the results reported in the work [36] on InAs metallization, such a layer is likely to prevent Al from etching into the semiconductor.

Next, relaxed Al growth in either  $[110]$  or  $[111]$  direction is observed, manifested by the appearance (and then dominance) of a second group of streaks. From the time it takes Al to start relaxing, we estimate the of strained Al or AlAs layer that grows prior. The results of each experiment are given in table 2.10 (page 40). We notice that faster growths allow for thicker strained regions, with  $\sim 1.5$  nm, or about 3.6 ML, being the maximum for Gr2.0 (the fastest one). This is in concordance with the lower thermal output from Al cells, discussed earlier in subsection 2.5.2: it takes longer to thermally activate the nucleation that favors the growth in a new direction. Therefore, it is reasonable to expect a higher quality of the metal-semiconductor interface for faster depositions, too.

It is worth noting that the sharpness of streaks for Gr2.0 was slightly better than for the rest of the growths at all stages. Moreover, its strained part is almost 1.5 thicker than of Gr2.0As with the same growth rate. This may be due to the additional measure we took to minimize sticking of the residual As: we kept the wafer at  $400^\circ\text{C}$  right after the end of  $\text{In}_{0.75}\text{Ga}_{0.25}\text{As}$  deposition until As background pressure dropped below  $10^{-10}$  Torr.

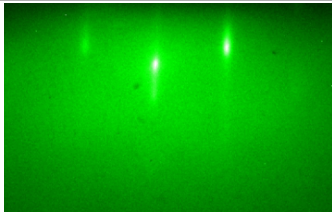
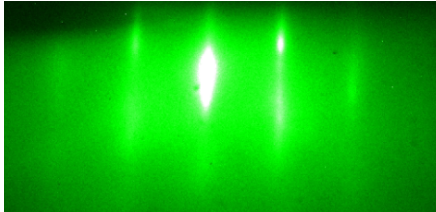
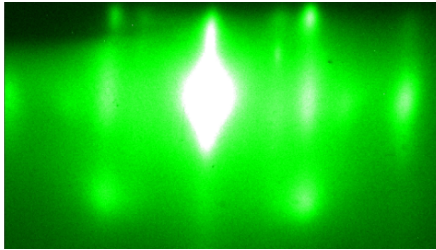
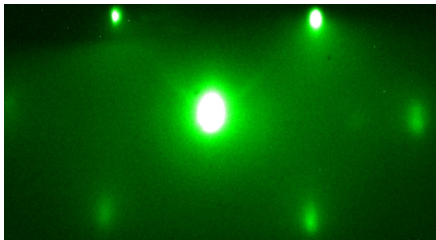
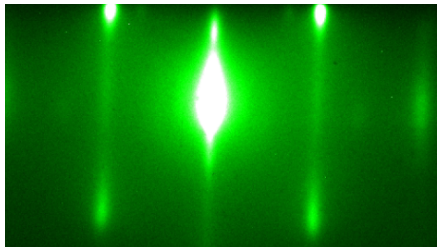
Event	Description	Image at a fixed 0° azimuth
Reconstruction changes overnight before the Al deposition	The streak spacing increases 2x during the overnight cooling, indicating the change of the reconstruction to $(1 \times ?)$	
Strained layer grows	The streaks' brightness grows, indicating the formation of a lattice-matched layer of Al or AlAs (possible due to the residual As adsorbate on $\text{In}_{0.75}\text{Ga}_{0.25}\text{As}$ )	
Relaxed aluminum diffraction pattern appears	2 <sup>nd</sup> series of streaks, spaced $1.41 \times \approx \sqrt{2} \times$ wider appears and grows in brightness. This indicates the formation of relaxed Al[110] or Al[111] layers, as $a_0(\text{InP}): a_0(\text{Al}) \approx 1 : \sqrt{2}$	
Aluminum diffraction pattern stabilizes	The relaxed Al layer streaks gradually transform into dots; the diffraction pattern from InGaAs layer gradually disappears.  The faster the deposition, the better the Al streaks preserve their shape	Gr0.1As (slow):   Gr2.0 (fast): 

Table 2.9: Evolution of the RHEED pattern at a fixed azimuth during the aluminum deposition. Gr0.1As data is presented unless otherwise specified.

Growth name	Growth #	Time for relaxed Al streaks to appear, s	Deposition rate of Al, Å/s	Thickness of the strained part, Å
G0841	Gr0.1As	58	0.1	5.8
G0842	Gr0.5As	13	0.5	6.5
G0843	Gr0.5	14	0.5	7
G0844	Gr2.0As	5.3	2	10.6
G0847	Gr2.0	7.3	2	14.6

Table 2.10: Strained growth of Al or AlAs: time before the growth of relaxed Al begins, and the thickness of the strained part.

### After the Al deposition

After the deposition of 10 nm of aluminum on Gr0.1As, Gr0.5As and Gr2.0As, we closed the Al shutter, opened the As valve and shutter, and waited until RHEED showed a completely hazy image with amorphous rings (fig. 2.17). It took us different time during different experiments: about 4.5 minutes for Gr0.5As and about 1 minute for Gr2.0As. This is due to high sensitivity of the process of As sticking to temperature: it takes more time to deposit an As layer on a hotter wafer.

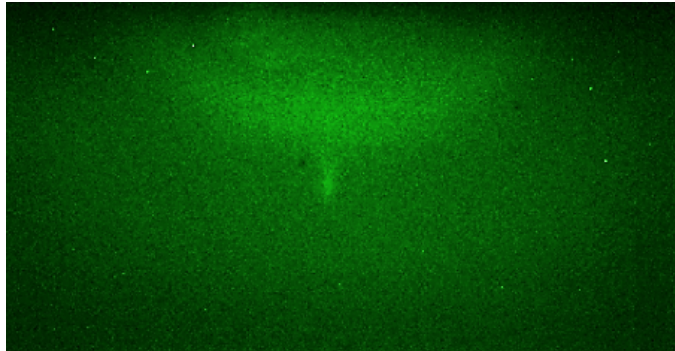


Figure 2.17: The onset of amorphous rings in Gr0.5As

For the uncapped Gr0.5 and Gr2.0, we waited for some more time until the RHEED pattern stabilized. After that, these samples were left in the storage part of our MBE chamber at UHV in the  $10^{-11}$  range, and were occasionally monitored on a daily or weekly basis. Gr0.5 demonstrated a very interesting dynamics, outlined in the flowchart 2.18. Within 1 minute after the growth, previously bright spots completely disappeared, and in about

30 seconds the pattern reorganized into dots separated  $\sqrt{2}$  times less than the relaxed Al streaks, or precisely as much as the initial InGaAs pattern! This clearly indicates a rearrangement of the top of the aluminum crystal. Dim dots from the relaxed Al growth mode re-appeared (circled), a new sequence vertical of streaks of unknown origin (framed) emerged, and a chevron-like pattern indicated the occurrence of faceting. However, these secondary features disappeared overtime, whereas the backbone of the pattern remained in place after 10 days at UHV. The relative brightness of the diffuse pattern substantially increased over this period, signifying the adsorption of background gases.

Remarkably, the dynamics of the Gr2.0 surface evolution (fig. 2.19) was completely different: the RHEED pattern showed only some increase in the diffuse component over the course of a month! This is a significant result, not presented previously, that sufficiently fast deposition of aluminum is sufficient to protect its surface from rearrangement over very prolonged periods of time even at high vacuum. This is the third advantage of fast epitaxial growth deduced so far, along with lower temperature increase and thicker strained part of the layer, which is likely accompanied with a better-quality metal-semiconductor interface.

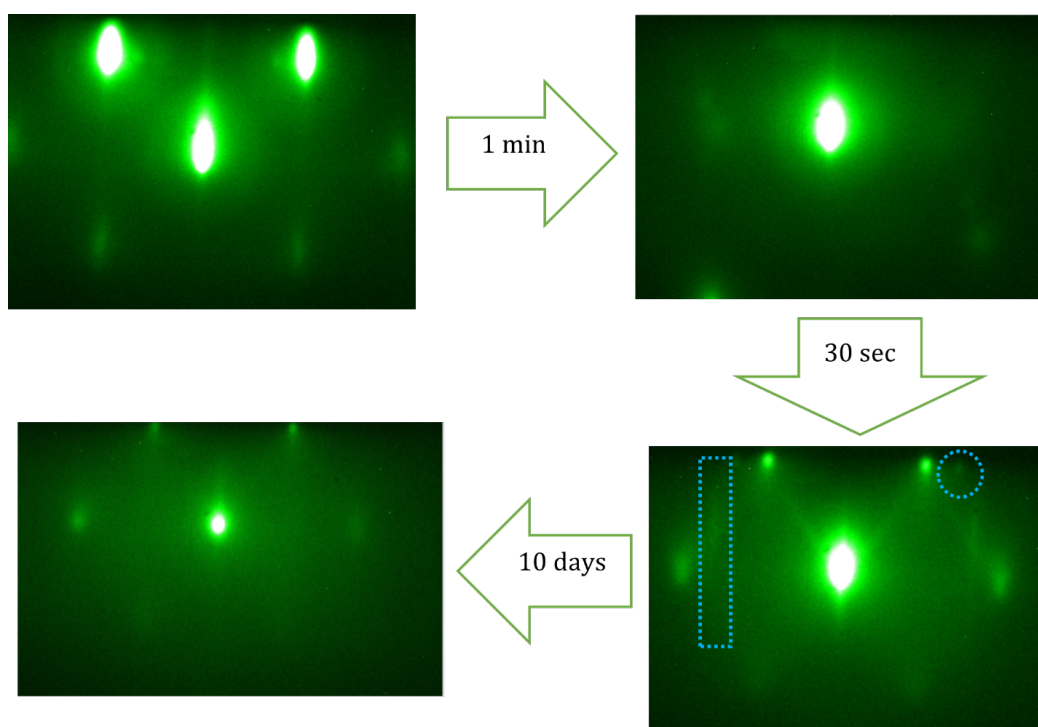


Figure 2.18: The evolution of RHEED pattern of Gr0.5, starting from the end of Al deposition.

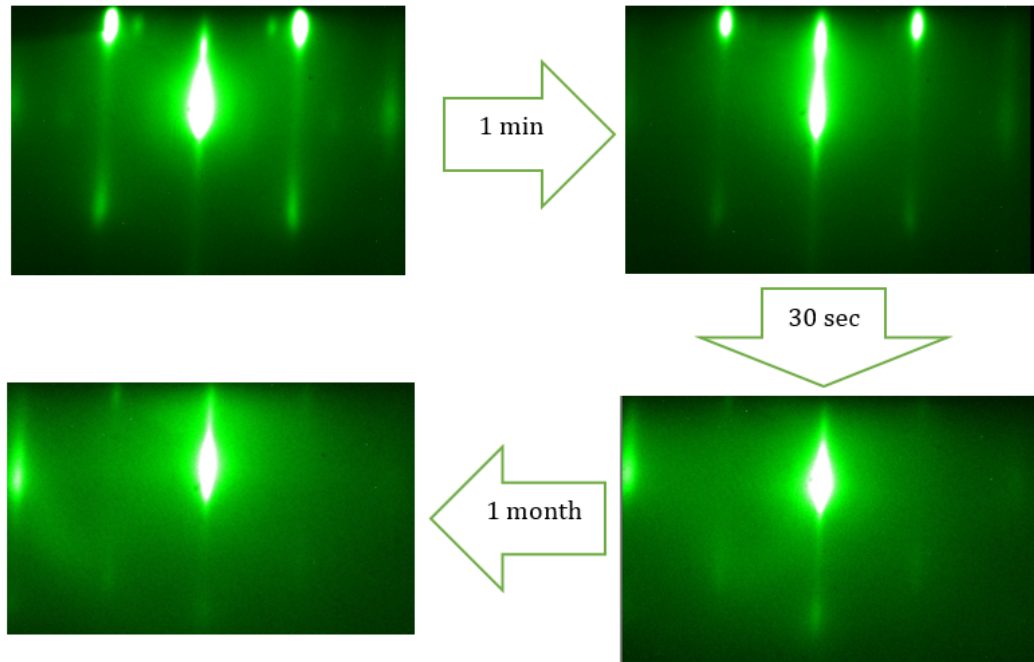


Figure 2.19: Evolution of Gr2.0 RHEED pattern over the course of a month.

## 2.5.4 Post-growth imaging

### Photos

After the Gr0.1As-Gr2.0 growths were finalized, we were ready to perform their preliminary surface morphology analysis with the tools available in our lab: a BB photography setup, and a Nomarski phase contrast microscope. We kept the uncapped growths at UHV for longer, though, for the sake of RHEED monitoring on large timescales.

The BB photos of samples capped with amorphous  $\text{As}_4$  (fig. 2.20) reveal dense arrays of point defects on their surfaces. Gr0.1As has the largest density of these features among all three wafers; furthermore, the features on this sample appear to be the most uniformly distributed. Conversely, there is a highly conspicuous area of finer roughness at the center of the Gr2.0As quarter, superimposed on the point defect pattern common for all these growths. Based on the photos at different exposures and at different wafer positions, a barely noticeable hazy area in the image of Gr0.5As is proved to be a stray reflection. Here and throughout, the words “hazy”, “wavy” and “shiny” specifically refer to the patterns observed with BB photography.



The growths without arsenic capping on top (fig. 2.21) show a significantly lower density of point defects. This indicates that the point defects largely consist of arsenic. At the same time, the top corners of both Gr0.5 and Gr2.0 appear wavy, which is most likely indicative of a more pronounced aluminum migration. As in the case of G0844, the formation of these distinct surface areas was likely due to the main shutter malfunctioning.

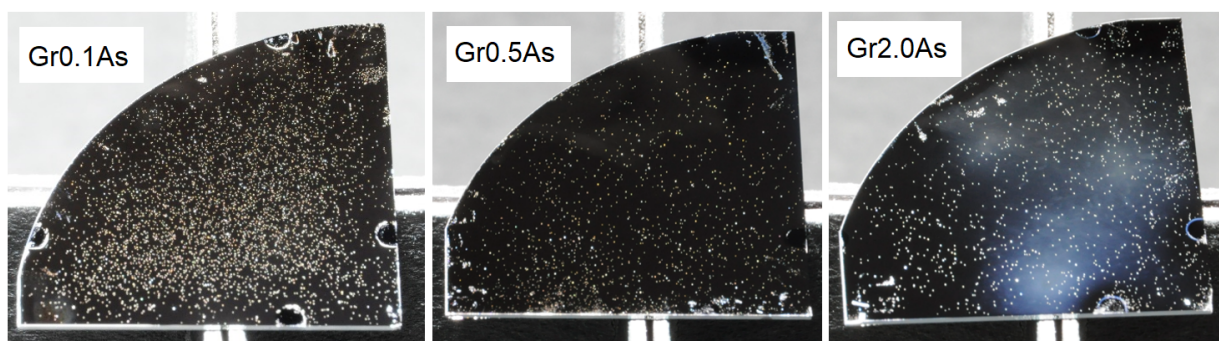


Figure 2.20: BB photos of the wafers capped with  $As_4$ .

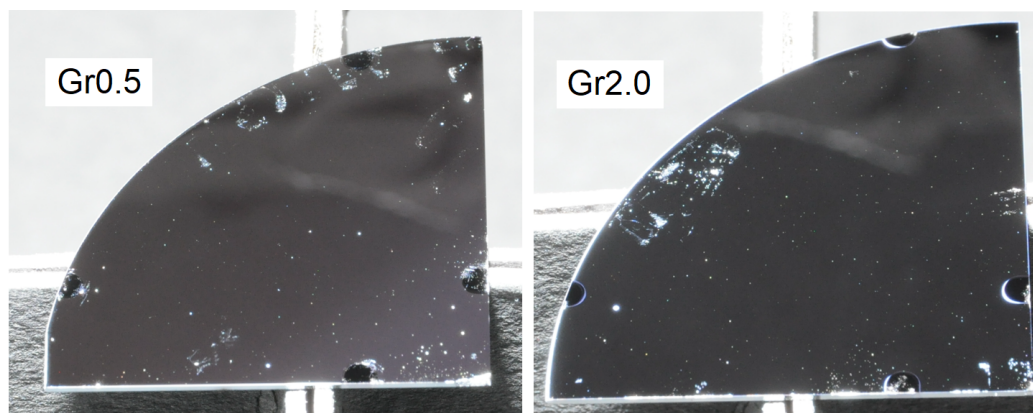


Figure 2.21: BB photos of the wafers not capped with arsenic. Bulging or large-scale roughness (“waviness”) is conspicuous in the top corners of both wafers.

## Nomarski microscopy

The Nomarski images of Gr0.1As reveal a relatively uniform density of point defects across the quarter wafer. We also observe horizontal relaxation lines that correspond to  $(0\bar{1}1)$  plane, which we determine from the quarter cleavage layout. The appearance of lines is not directly related to the epitaxy of thinnest layers but is rather due to stress releases in the substrate during thermal cycling. In Gr0.5As, the density of point defects does not significantly differ between the edges and the center (only a slightly higher density at the edges). In this case, we observe vertical relaxation lines, which correspond to the  $(0\bar{1}1)$  plane as well. In Gr2.0As, although only a part of the quarter appears hazy, the same types of features are observed across both hazy and shiny areas. Apart from the point defects of the same kind as in Gr0.1As and Gr0.5As, there is a finer grainy pattern in between the larger features. The roughness is more pronounced in the hazy areas; this is noticeable, however, only at x40 magnification. The Nomarski micrographs for all capped growths are presented in table 2.11.

The morphologies of uncapped Gr0.5 and Gr2.0 wafers (tab. 2.12) are very similar. We do not note any visual differences between the Nomarski images of the wavy and flat regions in either sample. The typical morphology in all parts of both wafers is scarce point defects and fine grain (similar to the one in the mirror-like areas of Gr2.0As). Relaxation lines are observed in either 1 or 2 directions in both wavy and mirror-like parts.




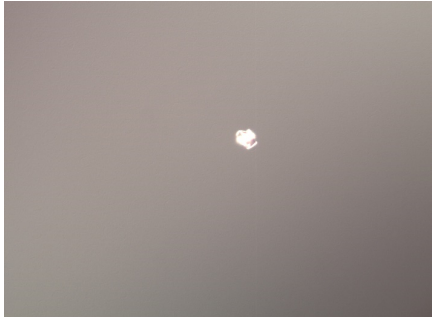


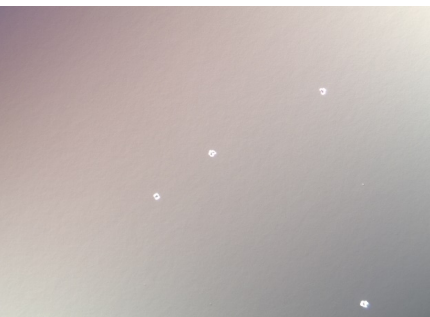
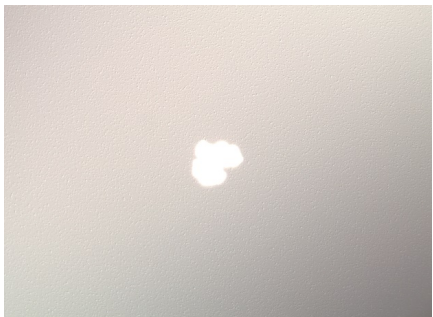
Growth	5x magnification	40x magnification
Gr0.1As, center		
Gr0.5As, bottom edge		
Gr2.0As, center (hazy area)		
Gr2.0As, bottom left corner (mirror-like area)		

Table 2.11: Nomarski images of the wafers capped with amorphous arsenic. Unlike Gr0.5, Gr0.1As and Gr0.5As are relatively uniform.


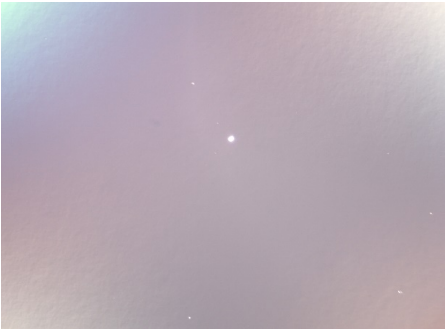


Area	Gr0.5	Gr2.0
Wavy		
Shiny		

Table 2.12: Nomarski images of the uncapped wafers (x40 magnification), showing no significant morphology differences in the areas differently affected by the Al migration.

### 2.5.5 Surface morphology studies with atomic force microscopy

The subsequent growth morphology analysis with AFM allowed us to better understand the feature formation on the samples, depending on whether they were capped or not, and at what rate aluminum was deposited.

#### Capped, mostly mirror-like samples

On the small scale ( $1 \mu\text{m} \times 1 \mu\text{m}$ ), the surface of Gr0.1As appears very grainy in AFM (tab. 2.13). Each grain has the lateral size of 40-100 nm and the height of about 12-15 nm. There also appear to be  $\sim 10$  nm deep trenches that separate grains. On the larger scale ( $25 \mu\text{m} \times 25 \mu\text{m}$ ), there are  $\sim 500$ -nm wide and  $\sim 10$ -nm deep pits that occur with the density of  $1\text{-}2/625 \mu\text{m}^{-2}$  (i. e. 1-2 times per scan) and are separated by  $>15 \mu\text{m}$  along

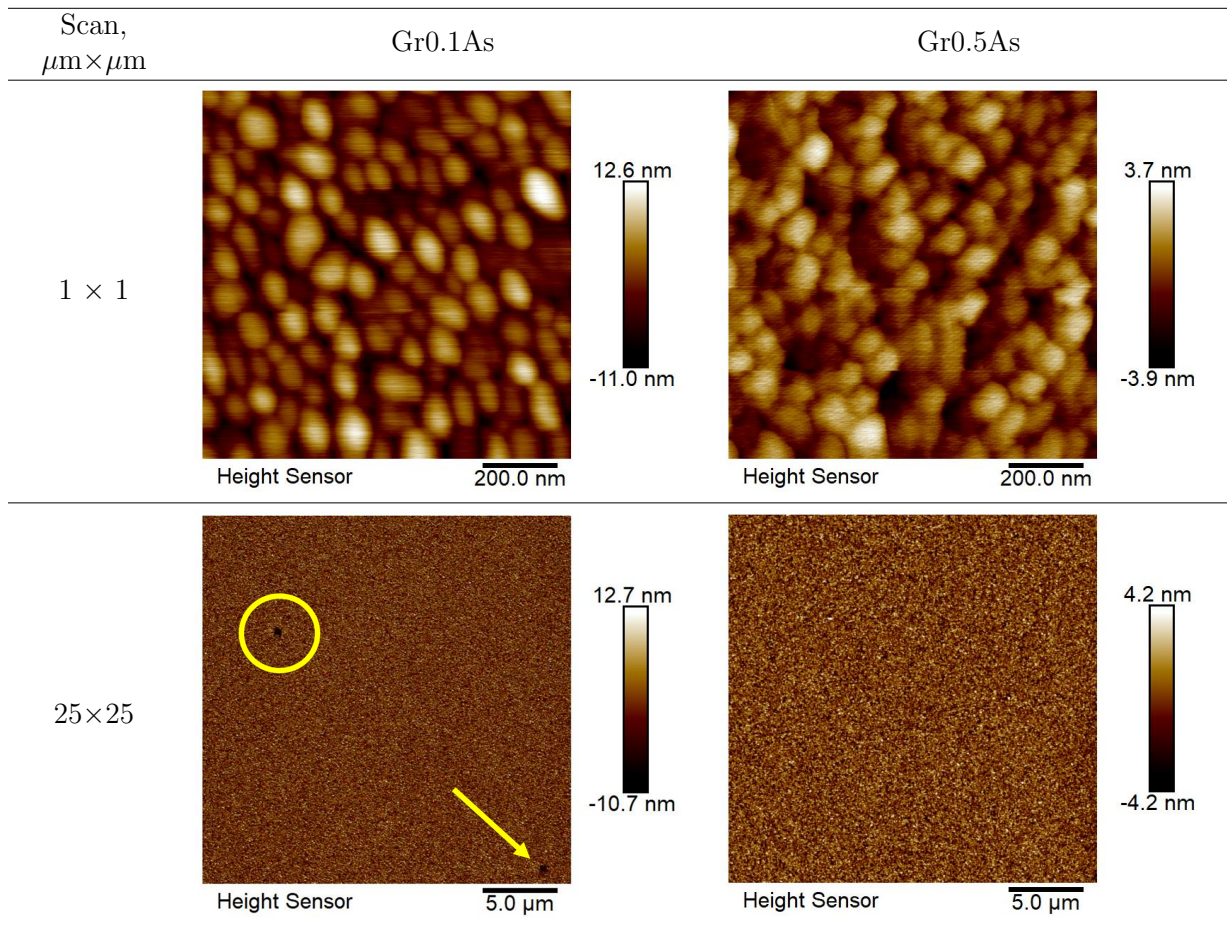


Table 2.13: AFM scans of the mirror-like areas of Gr0.1As and Gr0.5As. Grains look very similar but are bigger in Gr0.1As. This sample also has wide pits on the larger scale (highlighted), unlike Gr0.5As.

horizontal or vertical directions. We identify the point defects observed previously with Nomarski microscopy with these features.

As a reminder, all surface of Gr0.5As is most likely mirror-like; however, there is a suspicious haze along the round edge which is attributed to a stray reflection. For the definitely mirror-like part of Gr0.5As, the grainy pattern at  $1 \mu\text{m} \times 1 \mu\text{m}$  looks very similar to the one of Gr0.1As: the lateral size of the grains is very close (40–80 nm) but the distance “grain top – trench bottom” is much smaller: under  $\sim 8$  nm. Another important difference is the absence of the big pits on the large scale. The RMS surface

roughness in the areas without pits is on the scale of 2.19 nm. The hazy part of Gr0.5As looks the same as the mirror-like one in AFM; the only difference is the vertical scale of the scan being from about -6 nm to 6 nm, indicating slightly higher grains in the hazy area.

### Capped, mostly hazy sample

In Gr2.0As,  $\sim 10$ -nm deep pits surrounded by 10–15 nm tall mounts are scattered across both the hazy and the mirror-like areas, being more prevalent in the hazy one (fig. 2.22). The distance between such clusters is about  $5 \mu\text{m}$  (linearly, along x or y axis) in the mirror-like part, and  $\sim 1 \mu\text{m}$  in the hazy part, being the smallest observed so far. Unlike in Gr0.1As, the features between the big pits are elongated horizontally and resemble noodles rather than point defects (fig. 2.23). The pit-free regions are also shallower than the ones from other wafers (6.0 nm top to bottom, RMS roughness under 1 nm). The areas free from both noodles and pits are only several monolayers thick (RMS roughness  $\sim 0.3$  nm).

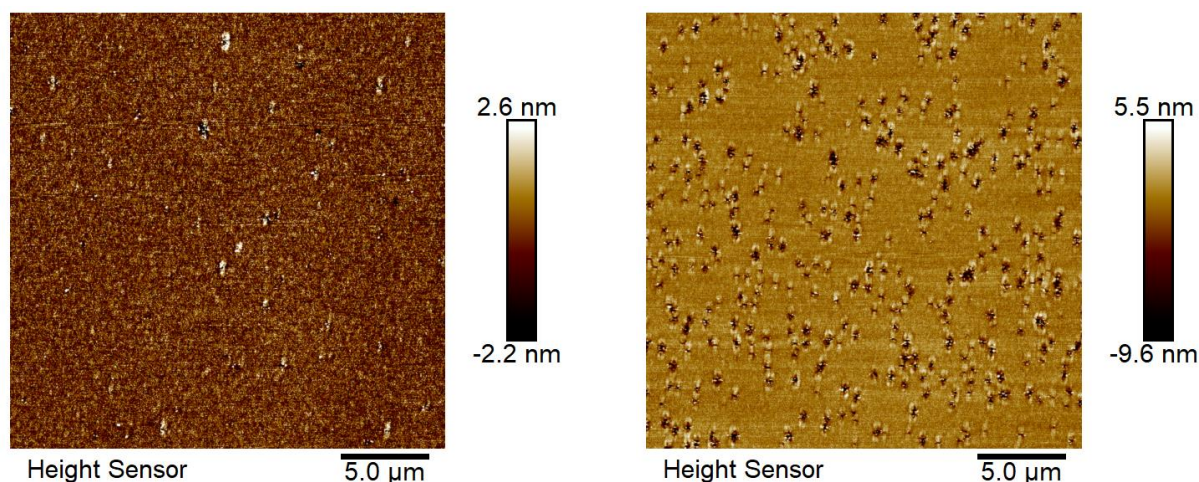


Figure 2.22:  $25 \mu\text{m} \times 25 \mu\text{m}$  scans of the mirror-like (left) and hazy (right) areas of Gr2.0As.

### Uncapped samples

In the photos discussed in the previous subsections, the top parts of both Gr0.5 and Gr2.0 look wavy, whereas their bottom parts look flat. However, the AFM scans in the two distinct regions do not indicate any significant difference in morphology between the wavy and flat regions on the microscale.

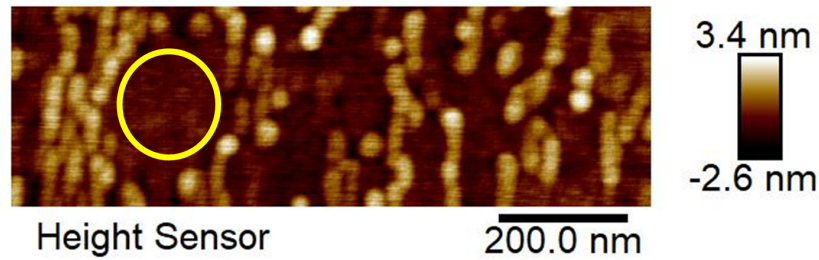


Figure 2.23: Horizontally elongated shallow features from the mirror-like part of Gr2.0As. RMS roughness  $\approx 0.3$  nm in the circled area is indicative of atomic-level flatness.

At the same time, there are differences in morphology between Gr0.5 and Gr2.0 overall. In the 2D scans from the figure 2.24, “khaki”-like patterns dominate, with a roughly uniform (Gr0.5) and nonuniform (Gr2.0) density of features. The features of Gr0.5 are alternating pits and mounts 60-120 nm in width and up to 8-9 nm in height. The surface of Gr2.0 is mostly intact, with sporadic  $\sim 100 \times 40$  nm elongated clusters of a mount and a trench around it with peak-to-peak heights of a few nm. The RMS roughness of the flat area is only about 0.2 nm, which proves that the surface in these regions consists of 1-2 ML thick atomic terraces.

The important difference from the capped samples discussed earlier is the complete absence of wide pits on the  $25 \mu\text{m} \times 25 \mu\text{m}$  AFM scans.

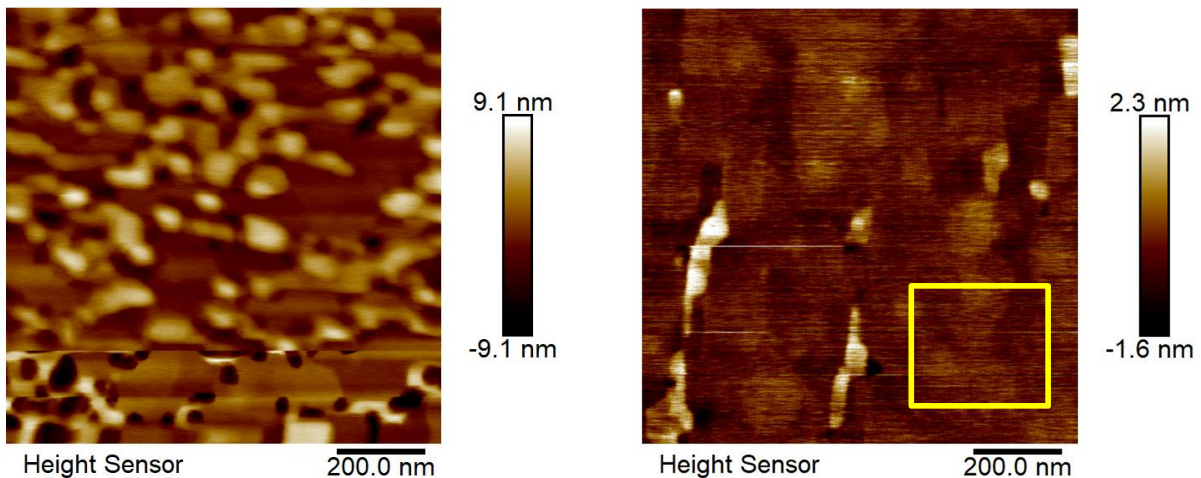


Figure 2.24: The AFM scans of the top (wavy) parts of Gr0.5 (left) and Gr2.0 (right). The RMS roughness below 0.2 nm in the frame area is indicative of atomic flatness.

## Surface morphology comparison

Overall, we observe relatively large feature-free areas with the atomic-level roughness only in one of the uncapped samples (Gr2.0). However, some less prevalent atomically flat areas can be spotted in Gr0.5 and Gr2.0As as well. All of these samples correspond to either the fastest (2 Å/s) or capping-free growth modes. The structure with the best surface flatness, Gr2.0, is also the only one that was kept at 400°C after the deposition of  $\text{In}_{0.75}\text{Ga}_{0.25}\text{As}$  to prevent unwanted As adsorption.

Table 2.14 summarizes all types of microscopic-level features identified in the samples. This data enables us to establish the key connection between the growth mode and the feature type: faster growth rates lead to less uniform feature distributions. Indeed, both horizontally stretched chains of sharp peaks from Gr2.0As, and sparse clusters of mounts of Gr2.0 coexist with atomically smooth terraces. The nonuniformity clearly correlates with a low level of thermalization due to reduced heat flux from Al cells.

When it comes to the large,  $\sim 500$  nm wide pits, they were observed only in the capped wafers on the scale of tens of microns. This proves their formation to be directly linked to the  $\text{As}_4$  deposition, which is consistent with the Nomarski microscopy results.



Feature type	Found in	Capping	3D view
Closely packed point defects	Gr0.1As, Gr0.5As	Capped	
Elongated, interconnected features with sharp but shallow peaks	Gr2.0As	Capped	
Alternating mounts and pits of comparable sizes	Gr0.5	Uncapped	
Sparse clusters of a mount and a trench surrounding it	Gr2.0	Uncapped	

Table 2.14: Summary of the distinct feature types identified with AFM in Gr0.1As–Gr2.0 samples.

## 2.6 Summary of chapter 2

In summary, we carried out a thorough investigation of the III-V heterostructure metalization with aluminum. A first extensive literature review on this topic was carried out to identify the mechanisms of aluminum formation and atomic dynamics. Then, numerous experiments were conducted to gain additional understanding of the effects of temperature and capping, underrepresented in previous studies.

From the literature, we identified and analyzed the following physical mechanisms of the Al film formation on a wide class of III-V superconductors:

1. Low temperatures inhibit group-V diffusion [34].
2. Group-V elements form covalent bonds with Al and other group-IIIs particularly well when the surface reconstruction is group-V-rich. The covalent bonds suppress the exchange reactions between Al and group-III elements from the semiconductor layer [34]. Therefore, even a sub-ML of arsenide (antimonide) can ensure an abrupt interface [36, 38–41, 49] that does not degrade over a long period of time [40]. An As(Sb)-rich semiconductor surface reconstruction can lead to similar results [32, 35, 38].
3. Good choice of surface reconstruction symmetry based on the symmetry of the crystal plane fixes the Al growth direction: the reconstruction symmetry should be low enough so that the grains of equal formation energy, but different orientation do not form [32].
4. There is a threshold value for semiconductor lattice constants that marks the change in the dominant Al growth direction [39].
5. Reducing strain at the top of the semiconductor buffer favors the growth of Al along the axes with lower surface energies, with [111] having the lowest one [37, 38].
6. There exists an optimal thickness of the interlayer buffer used to prevent the exchange reaction that gives the best interface abruptness [36].

Our experiments complemented this list with two general conclusions: (1) minimizing the cumulative heat transfer into the wafer during Al deposition is the critical factor to achieve a high quality of the metal layer and its interface with the underlying semiconductor; and (2) in situ capping with As<sub>4</sub> is a viable alternative to Al layer oxidation reported in [38, 40].

More specifically, the key results of our original study are the following:

1. With the use of the Al deposition rate ( $3 \text{ \AA}/\text{s}$ ) much higher than reported in literature, we demonstrated depositions of flat 10 nm Al layers on top of  $\text{In}_{0.75}\text{Ga}_{0.25}\text{As}$  with a pristine metal-semiconductor interface. The layer structure of the growth G0680 was confirmed with the cross-sectional SEM, and then with atomic-resolution STEM & EELS. A significantly lower quality was reported for the growth G0697.
2. Capping with amorphous  $\text{As}_4$  was proved effective for the better-quality growth (G0680). The chemical processes that the capping layer undergoes on different timescales remain to be investigated.
3. A series of heterostructures with a broad range of Al deposition rates (0.1, 0.5,  $2 \text{ \AA}/\text{s}$ ), and with or without  $\text{As}_4$  capping, were grown with thorough monitoring of temperature dynamics, growth mode, and surface quality before, during and after the Al deposition. In all cases, faster rates yielded growths of better quality:
  - (a) An analytic model for the first-order heat transfer dynamics during and after Al deposition was constructed from the BET data. The duration of deposition – and not the Al cell temperature – was proven to determine the overall thermal effect on the wafer. This has lead us to the conclusion that using faster growth rates of Al is beneficial for the mitigation of wafer heating.
  - (b) Two phases of aluminum deposition (strained and relaxed) were identified with RHEED, with the strained phase being thicker (up to  $15 \text{ \AA}$ ) for faster growths. The strained part of the structure is speculated to possibly consist of lattice-matched AlAs rather than Al due to the presence of residual As adsorbate on  $\text{In}_{0.75}\text{Ga}_{0.25}\text{As}$ . Overall, faster Al growths were proven to be significantly closer to 2-dimensional than slower ones.
  - (c) Long-term RHEED monitoring of the uncapped structures revealed two distinct surface evolution scenarios. The surface of the Al layer grown at a low rate completely rearranged within a minute after the end of deposition, whereas the surface reconstruction of the one grown faster remained unchanged. After this, both surfaces retained their structure for weeks even at UHV.
  - (d) An ex-situ surface morphology study with Nomarski microscopy and AFM revealed  $\sim 500 \text{ nm}$  wide point defects separated by ones to tens of microns on all samples capped with  $\text{As}_4$ . Smaller, nanoscale features of the sample surfaces were resolved with AFM and classified. The features proved to be less uniformly distributed and more spatially dispersed in the samples with faster Al growth rates. The degree of surface flatness in feature-free areas proved to be higher in these heterostructures, too (up to the atomic level). The lesser surface thermalization of faster growths is consistent with their lower degree of heating.

# Chapter 3

## Algorithm and software design for a spin-qubit quantum architecture simulation

### 3.1 Motivation

Silicon is known to be a very attractive platform for scalable spin-based quantum computation. First of all, this material currently dominates microelectronics industry. Secondly, its most prevalent isotope  $^{28}\text{Si}$  has zero nuclear spin; therefore, a significant source of decoherence — electron-nuclear interactions — is naturally suppressed in the material. The additional suppression in isotopically purified samples leads to such particularly outstanding numbers as spin lifetimes on the order of seconds [50].

The development the field has seen since the seminal proposals for universal one- and two-qubit gate implementations in semiconductor quantum dots [51], and the prototypical quantum computer architecture [52], is twofold. First of all, initial reports on state preparation, coherent manipulation and readout in GaAs [21, 53] led to subsequent improvements towards highly controlled spin qubits in Si quantum dot arrays [54, 55], very high fidelities of single-qubit [56, 57] and two-qubit [57] operations. Together with the improvement of measurement techniques, it already led to the development of controllable, CMOS-compatible systems [4, 58], and a universal two-qubit programmable processor [22] in silicon. The recent report on high-fidelity gate operations at high ( $\sim 1\text{K}$ ) temperatures [59] gives even more reassurance that accessible small-scale Si quantum computers are to be seen in the near future. Secondly, a significant number of scalable network designs

for spins in silicon quantum dots or donors were proposed [23, 60–63]. The achievement of fault-tolerant quantum computation with the network-level error correction (surface code) algorithms [23, 60, 64] is becoming more realistic as the gate operations approach (or even already exceed [56]) the necessary error thresholds.

The scalable computer architecture, previously developed in our research group and published in [65], offers to bridge these two streams of development by utilizing a node-network approach. This computer design features a network of compute nodes, capable of performing all necessary quantum operations, separated on a micron scale and connected with electron shuttling lines. This allows for a gradual experimental implementation (i. e. starting with small numbers of nodes, and then scaling up) without sacrificing the logic of a high-level network architecture, which is impossible to achieve in the dense designs proposed elsewhere [61, 62]. While there is experimental progress in developing MOS quantum dot devices in our group [66], it is beneficial to simulate the operation of compute nodes before the prototypical implementations are created. This will allow to choose the optimal gate geometries, determine the voltage operation range, and design the optimal voltage and ESR field pulses to experimentally realize quantum computation. The presentation of the developed software and its node simulation capabilities are the main topics of this chapter.

Section 3.2 gives a short summary of our architecture [65] with the focus on the quantum control of individual computational nodes, and places this architecture among other proposals in the field. Sections 3.3 and 3.4 are dedicated to our custom-built Python package “QuDiPy” for semiconductor quantum dot network simulations, its theoretical foundations, scope, and the application to the node operation simulation. Section 3.5 gives a summary of the main results.

Since the development of QuDiPy is a large collaborative project, other people authored some of the code discussed in this chapter; see Statement of Contributions for explanation.

## 3.2 Spin qubit quantum computer architecture in silicon

The article [65] published in our group proposes a node-network architecture for a large-scale surface code quantum processor. The minimal compute node requires only seven quantum dots for the operation. Entanglement between nodes is distributed by loading spin singlets locally, and then shuttling individual electrons on a  $\mu\text{m}$  scale.

A prototypical device design for the node is shown in figure 3.1. Accumulation gates (golden) electrostatically define distinct quantum dots in the 2DEG that forms under the Si/SiO<sub>2</sub> interface. The tunnel barriers between all neighboring dots within a node are directly controlled with the voltages on tunnel gates (grey). Each node is connected to a distant ion-implanted region (electron reservoir) and other nodes with  $\sim 1 \mu\text{m}$  long chains of shuttling dots (red ovals) without explicit tunnel gates between them. The large separation of the nodes from reservoirs enables us to minimize number of interconnects and, subsequently, capacitive cross-talk between components, charge noise and power dissipation. This is thus a competitive advantage of our architecture over the ones proposed in [61, 62]. The feasibility of coherent shuttling over micrometer scales was previously confirmed in the work [67] with the design of constant-adiabaticity voltage pulses.

Unitary operations on the data and ancilla qubits are realized with the pulses of gate voltages, and the oscillating global magnetic field produced by a microresonator. Compared to the EDSR-based processor realization [22], our proposal does not require micromagnets and thus offers a better scalability. To deterministically address individual qubits, we manipulate the electric field from the plunger and tunnel gates to induce local deviations of electron  $g$ -factors. This phenomenon is a consequence of a nonzero spin-orbit interaction in silicon. This approach, based on the one implemented in refs. [54, 61], enables us to drive distinct single-qubit rotations despite the global nature of the ESR field. Two-qubit  $\sqrt{\text{SWAP}}$  gates are realized by the direct control of exchange interaction with tunnel gate voltages.

The measurements of ancilla qubits are carried out with radio-frequency (RF) dispersive readout [58, 68–70] in conjunction with the Pauli spin blockade. The method is based on sensing the quantum capacitance of the double dot R1, R2. During the measurement, the state of the double dot is conditioned on the state of the ancilla by means of a CNOT operation. Pauli principle determines the possibility of electron tunneling from R1 to R2 and thus the final spin-charge state of R1, R2 (triplet T(1,1), or singlet S(0,2)). It is discerned from a resonant frequency shift in an RF readout line.

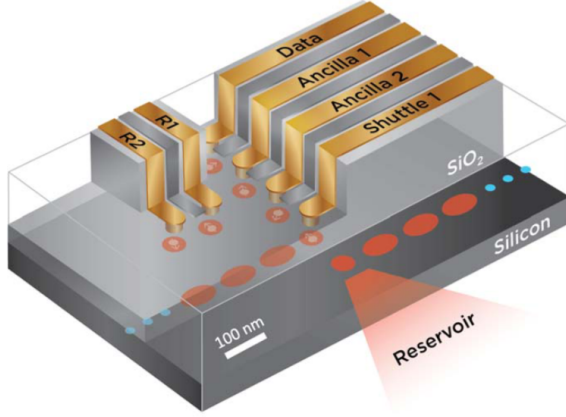


Figure 3.1: Device-level proposal for a compute node. Accumulation gates for shuttling dots, and the tunnel gate between the readout dot R1 and ancilla qubits are not shown but implied. Reproduced from [65].

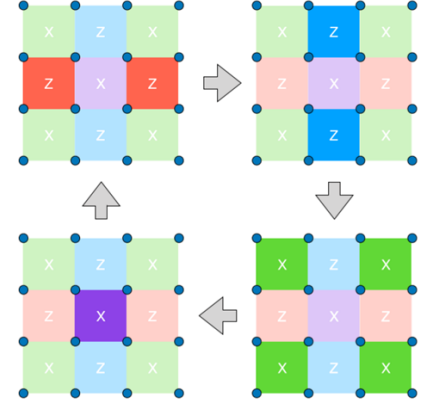


Figure 3.2: 4-step cycle of the surface code for error correction. X or Z stabilizer gates are applied simultaneously on groups of four nodes (highlighted with different colors). Reproduced from [65].

The error-correction scheme is based on a surface code algorithm, applied on a square lattice of nodes (sketched in figure 3.2), is closely related to the surface code proposals from other sources [23, 61]. The implementation of the stabilizer circuit from figure 3.3 for a group of 4 data qubits includes 4 stages. During stages 1 and 2, two-electron singlet states are loaded from the reservoirs, transferred to the nodes, and the individual spins are distributed among the ancillas. At stage 3, a maximally-entangled four-electron GHZ state is formed:

$$|\text{GHZ}\rangle = \frac{1}{\sqrt{2}} (|0000\rangle + |1111\rangle).$$

It is used as shared entanglement resource for ancilla qubits in different nodes, necessary to apply X or Z stabilizers at the stage 4. The conditional application of quantum gate operations based on measurement results, explained in detail in the appendix of this proposal [65], ensures a deterministic ancilla state preparation and data qubit stabilization. The ancillas are emptied to the reservoirs once measured to make room for newly prepared states, used in the next step of the stabilization cycle.

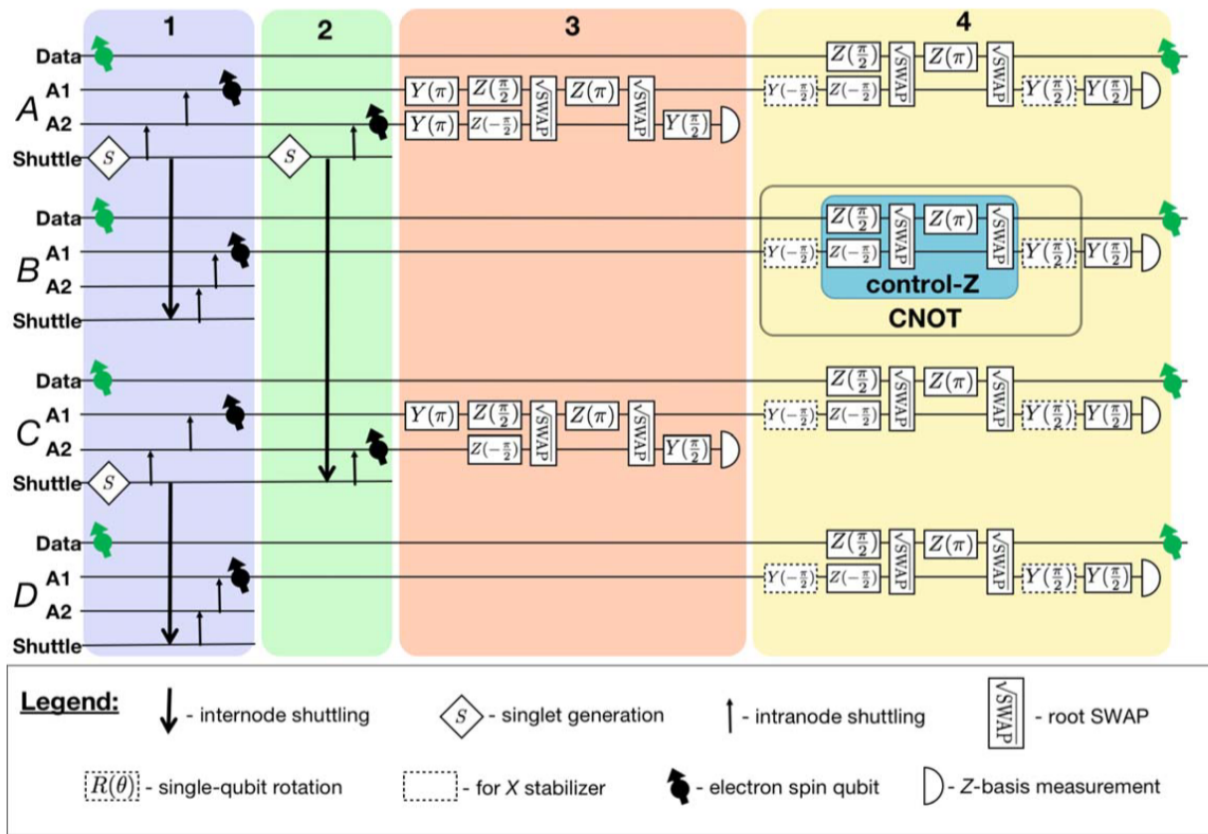


Figure 3.3: Quantum circuit for the data qubit stabilization of a group of four nodes. Reproduced from [65].



## 3.3 QuDiPy: a quantum dot simulation package

To simulate the operation of the proposed quantum computer architecture, we have been developing an open-source Python package for the simulation of quantum dot systems named QuDiPy<sup>1</sup> (“Quantum Dots in Python”). Code modules that require the most CPU and memory resources rely on the heavily optimized algorithms from NumPy [71] and SciPy [43] Python libraries, and are planned to be optimized for distributed computing on CPU and GPU clusters.

### 3.3.1 Simulation of the node operation

Figure 3.4 outlines how the modules of QuDiPy are interconnected to design voltage and ESR field pulses for controlled node operations such as quantum gate applications or electron transfers.

A node (center of the diagram) consists of a chain of quantum dots defined by the positive voltages  $V_1, V_2, \dots$  on plunger gates. The voltages on tunnel gates  $W_1, W_2, \dots$  control the electron confinement, tunnel coupling and exchange interaction between pairs of neighboring dots. The full network of such nodes shares two global magnetic fields. First one is the static Zeeman field  $\vec{B}_0$  (purple) directed along the Si/SiO<sub>2</sub> interface (perpendicular to the plane of the diagram), which we choose to be the  $z$  direction for convenience. The global radio-frequency ESR field, produced by the microresonator located above all gates, lies in the  $xy$  plane, i.e. plane of the diagram (both the resonator and the field it produces are denoted with orange). The resonator frequency  $f_{\text{RF}}$  is chosen to be constant, but the envelope of the field oscillations  $\vec{B}_{\text{RF}}(t)$  and phase  $\phi(t)$  are time-dependent.

Suppose there is a quantum algorithm that should be implemented. Circuit module (top left corner) is designed to load and process scripts that define the corresponding quantum circuits, and transform them to matrix representation. Circuit module communicates this reference information to Control module, whose role is to generate the appropriate sequence of voltage and ESR control pulses. The approaches towards optimal pulse design for spin quantum gates constitute a significant part of the original results presented in this thesis and are thus dedicated separate chapters 4 and 5. Coherent electron shuttling is achieved with the constant adiabaticity pulse design, described in the reference [67].

Control module relies on the connection between the gate voltages and the quantum parameters of the electron system. To establish this dependency, we use a third party

---

<sup>1</sup>Link to GitHub repository: <https://github.com/mainCSG/QuDiPy>

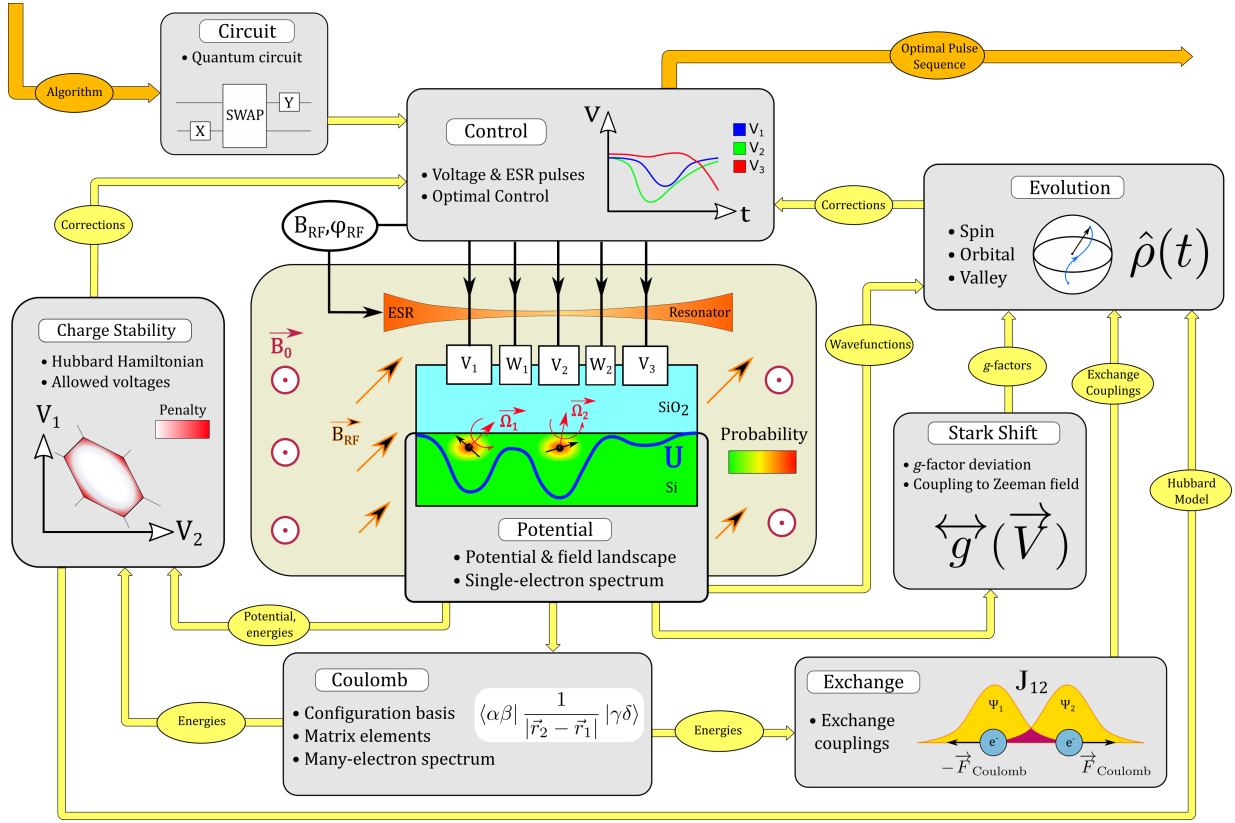


Figure 3.4: Pulse desing for quantum node operations with a network of QuDiPy modules. When the modules request only specific information from other ones, it is shown in yellow ellipses.

solver `nextnano++` [72], capable of extracting the potential landscape from the simulation of a chosen semiconductor structure, gate geometry and supplied voltages. The Potential module of QuDiPy processes the `nextnano++` data to acquire 2-dimensional horizontal slices of potential energy  $U(x, z)$  and electric field  $\vec{E}(x, z)$  at the selected distance  $y_0$  below the Si/SiO<sub>2</sub> interface. Refer to the subsection 3.4.1 for a more detailed description of how the data is extracted and processes. The module uses this information further to find single-electron wavefunctions and energies of the system.

The purpose of Coulomb module (bottom) is to quantify the magnitude of Coulomb interaction between the electrons, which serves as a starting point for the development of the effective models of the system. This module relies on a full CI calculation method outlined in our group’s paper [1]; the summary of the method is given in subsection 3.4.2.

At first, the module evaluates Coulomb matrix elements in the optimal configuration basis, and then constructs and diagonalizes the second quantization Hamiltonian of the many-electron system.

Charge Stability module (left) relies on the single-electron and many-electron energy spectra of the system, calculated by Potential and Coulomb modules. The energies are used to calculate the system Hubbard model parameters [73] like chemical potentials, tunnel couplings, and direct Coulomb repulsion terms between pairs of electrons. Hubbard model is used to determine the correspondence between gate voltages and the charge configuration of the quantum dot system. The voltage values that favor undesired charge transitions are associated with a certain scalar function. This information is directly returned to the Control module, where it serves as a component of the cost function minimization problem. This control problem will be rigorously defined in section 4.2 of the following chapter.

Exchange and Stark Shift modules (bottom right) are used to quantify parameters of another model Hamiltonian that describes spin states of the electrons only. Stark Shift module uses the electric potential and field landscapes as well as the single-electron wavefunctions to find the  $g$ -factor deviations for each electron. The cartoon in the middle of the diagram shows one of the outcomes of  $g$ -factor variations across the dots: spin precessions around different axes with distinct angular velocities  $\vec{\Omega}_1, \vec{\Omega}_2$ . This allows us to address individual spins during the pulses of global ESR field, as will be shown explicitly in the section 4.3. Exchange module calculates exchange couplings between pairs of quantum dots (essential components for 2-qubit gates in our architecture) from the many-electron energies evaluated in the Coulomb module. Its cartoon reminds that the strength of exchange interaction is determined by the Coulomb repulsion of the electrons  $\vec{F}_{Coulomb}$ , and the overlap of their wavefunctions.

The Evolution module takes the outputs of Potential, Charge stability, Stark shift and Exchange modules for a given sequence of voltages and ESR magnetic field parameters, and simulates the time dynamics of the electron system. Electron state evolution under the spin Hamiltonian determines the quantum gate operations, whereas the evolution under Hubbard or real-space Hamiltonian represents electron shuttling between the dots. Based on the process and outcomes of the evolution (such as fidelity of the final state with respect to the expected one), corrections necessary for pulse optimization are supplied to Control module.

The cycle repeats until the desired level of optimality is achieved. In practice, such modules as Coulomb, Charge Stability, Exchange, or Stark shift may rely on the `nextnano++` data processed and interpolated in advance instead of doing calculations from scratch; in this case, they can construct time-dependent effective spin and Hubbard Hamiltonians

right away. The finalized pulse sequence can then be used to test experimental devices, which constitutes our long-term goal.

### 3.3.2 Scope of the simulator

The capabilities of our simulator are not limited to the design of optimal control pulses. From the very beginning, effort has been made to make QuDiPy a general-purpose toolkit for simulating electron dynamics in semiconductor quantum dots. Its capabilities, either already implemented or planned, are expected to cover a wide variety of theoretical and experimental areas of our research towards the development of a scalable spin-based quantum computer in silicon, and, hopefully, other projects relying on quantum control of electrons in semiconductors. For example, it is capable of simulating arrays of dots of any lengths, processing both analytically and numerically defined electric potential landscapes, and extracting constant interaction model [74] parameters from a given charge stability diagram. It is also equipped to simulate GaAs devices.

Table 3.1 (pages 62–64) covers the scope of each module from the diagram 3.4 described earlier, and the external software QuDiPy is interfaced with.

Module	Completed	In progress	Planned
Circuit	<ul style="list-style-type: none"> <li>- Encode, save, load and draw custom quantum circuits</li> <li>- Simulate evolution under ideal circuits</li> </ul>		
Potential	<ul style="list-style-type: none"> <li>- Process 1D/2D electric potential and/or field landscapes from numerical data and analytical formulas for any numbers of gate voltages</li> <li>- Find single-electron wavefunctions and energies</li> </ul>		Process 3D potential data and find eigenvalues/ eigenfunctions directly

Coulomb	<ul style="list-style-type: none"> <li>- Choose optimal harmonic basis for full CI calculation</li> <li>- Evaluate Coulomb interaction matrix elements (CMEs) in the optimal basis</li> </ul>	<ul style="list-style-type: none"> <li>- Construct and diagonalize second quantization Hamiltonian</li> <li>- Speed up the evaluation of CMEs using symmetry considerations</li> </ul>	<ul style="list-style-type: none"> <li>- Choose harmonic basis with optimal origin and azimuth</li> <li>- Deploy the code on distributed systems to efficiently simulate long qubit chains</li> </ul>
Stark shift	Extract electron $g$ -factors from potential and electric field landscape	Extract $g$ -factors from dot chains of any lengths	
Exchange		Calculate exchange interaction for each pair of quantum dots	Map energy spectrum of multiple electrons onto Heisenberg Hamiltonian
Charge stability	<p>Generate charge stability diagrams from:</p> <ul style="list-style-type: none"> <li>- General capacitance matrix</li> <li>- Hubbard model</li> </ul>	<ul style="list-style-type: none"> <li>- Extract transition lines and triple points from a given charge stability diagram to build a general capacitance matrix</li> <li>- Construct a Hubbard Hamiltonian parameters from a potential landscape</li> <li>- Determine operable window of gate voltages from Hubbard model data</li> </ul>	

Evolution	<p>Simulate dissipative dynamics under the pure spin Hamiltonian, including:</p> <ul style="list-style-type: none"> <li>- partly unpopulated dot chains of any lengths</li> <li>- qubit measurements, loads</li> <li>- fidelity, purity, single-electron subsystems being monitored</li> </ul>	<p>Simulate electron shuttling along a 1D chain of dots:</p> <ul style="list-style-type: none"> <li>- real space Hamiltonian</li> <li>- spin-orbit-valley effective Hamiltonian</li> </ul>	<p>Simulate shuttling in 2D and 3D</p>
Control	<ul style="list-style-type: none"> <li>- Load custom control pulses</li> <li>- Design pulses of chosen shape for single-qubit gates</li> <li>- Find constant adiabaticity pulses for 1D electron transport</li> </ul>	<ul style="list-style-type: none"> <li>- Design pulses of chosen shape for two-qubit gates</li> <li>- Engineer high-fidelity voltage pulses by incorporating interdot couplings</li> <li>- Find constant adiabaticity pulses for 2D and 3D Hamiltonians</li> </ul>	<ul style="list-style-type: none"> <li>- Design optimal voltage and ESR pulses with gradient ascent</li> <li>- Optimize gradient ascent code for parallel and GPU-based computation</li> </ul>
Connection with external software	<p>Import electric potential and field data from <b>nextnano++</b></p>	<p>Output the control pulses for multiplexing the network of nodes, emulated in Cadence<sup>®</sup> Virtuoso software</p>	

Table 3.1: Functionality and intended use of QuDiPy modules. The implementation process of each listed capability consists of code development and testing, creation of tutorials and unit tests (if applicable), and peer review by 1-2 fellow developers. The Python modules corresponding to the “completed” status have undergone all these stages (but may still be improved in the future), the ones “in progress” are missing some of the stages. The “completed” and “in progress” statuses in this table are up to date for December 22, 2021.

## 3.4 Theoretical foundations of the simulator

### 3.4.1 Potential data extraction and manipulation

As noted before, the Potential module of QuDiPy obtains the electric potential and field data from the `nextnano++` [72] software. It is a Poisson (P) and Schrodinger-Poisson (SP) solver for 3-dimensional nanoscale semiconductor-based devices (refer to the resource [75] for a summary of P / SP methods). While being very feature-packed, the functionality of simulators of this kind does not incorporate the effective electron isolation from highly doped regions, achieved in our architecture. More precisely, it is impossible to fix the discrete values of electron charge in each quantum dot: first, both Poisson and Schrodinger-Poisson methods yield continuous charge values, and second, `nextnano++` simulation populates the energy levels that lie below the Fermi level even for isolated dots. Physically, though, the dots are protected from this (up to a certain degree) due to the decoupling from electron reservoirs.

To bypass this limitation, we carry out all nanodevice simulations at the voltages just below the charge accumulation threshold. We use Poisson method for this, since P and SP methods give the same results for the case of no electron in a dot. In this case, we expect to observe a consistent dependency of effective spin and Hubbard parameters on the potential landscapes and thus gate voltages. The work [67] analyzes in more detail the effect of this simplification on the potential relief, shape of single-electron wavefunctions and their overlap. The charge accumulation regime at higher voltages allows us to determine the depth  $y_0$  under the Si/SiO<sub>2</sub> interface where the electron is localized. The potential and field landscapes  $U(x, z)$ ,  $\vec{\mathcal{E}}(x, z)$  are extracted at this depth for all voltages in the operable window.

Both spin and Hubbard model describe a quantum system in terms of single-electron or pairwise interactions, or couplings. To approximately separate the effects of individual electrons or their pairs, we *mask* certain parts of the potential landscape between its saddle points, representing tunnel barriers between the dots. This ensures that the eigenproblem for the “masked” potentials correctly describes a specified subsystem of electrons. Figure 3.5 gives an example of splitting an analytically defined potential landscape, constructed from three overlapping Gaussians:

$$U(x, z) = \min \left( -U_1 e^{-\frac{(x-d)^2+z^2}{a^2}}, -U_2 e^{-\frac{x^2+z^2}{a^2}}, -U_3 e^{-\frac{(x+d)^2+z^2}{a^2}}, \right) \quad (3.1)$$

with  $U_1 = U_2 = U_3 = 10 \text{ Ry}^*$ , dot separation  $d = 7.5 \text{ a}_B$ , and dot width  $2a = 4.6 \text{ a}_B$ . Here,

the effective Rydberg parameters for silicon are introduced:

$$a_B = \frac{\epsilon_0 \epsilon_r \hbar^2}{\pi m^* e^2} = 2.16 \text{ nm}, \quad Ry^* = \frac{e^2}{8\pi \epsilon_0 \epsilon_r a_B} = 6.84 \cdot 10^{-21} \text{ J} = 42.77 \text{ meV}. \quad (3.2)$$

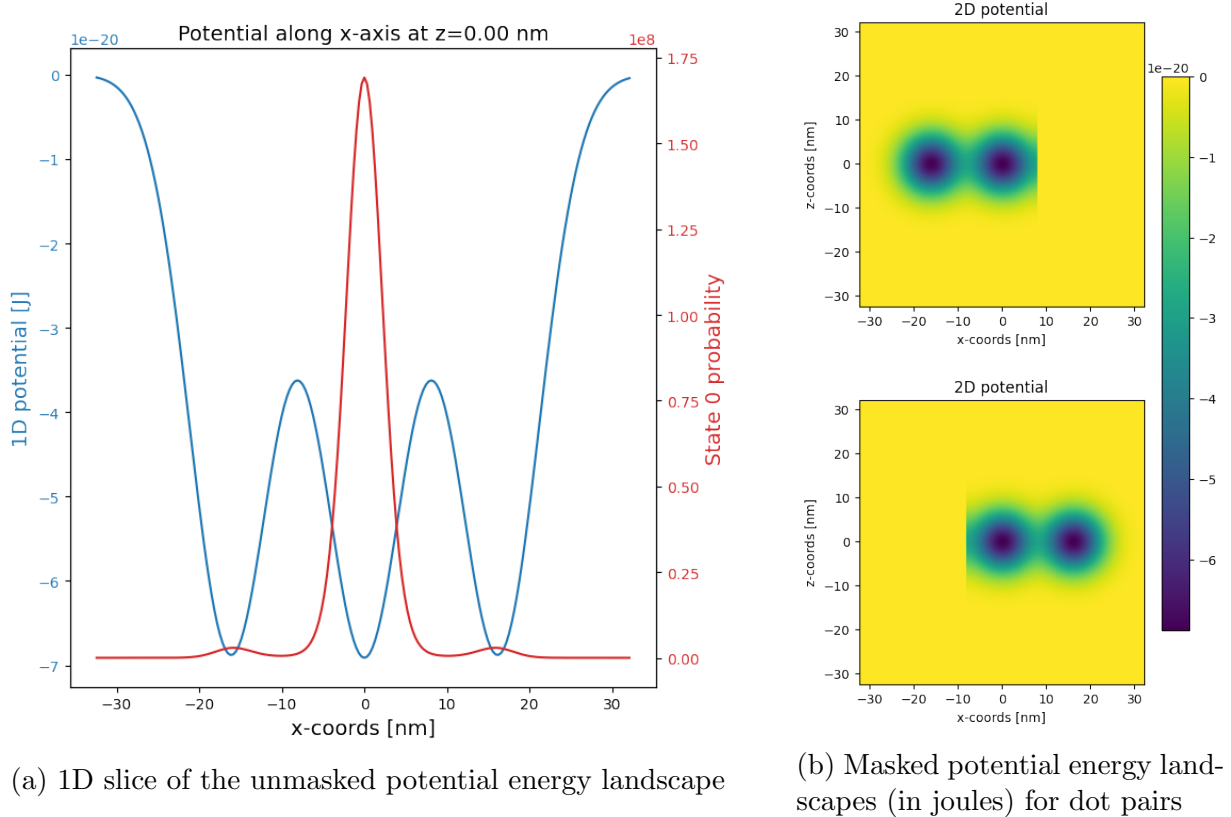


Figure 3.5: Pre-processing of the 2-dimensional analytical potential (3.1). (a): 1D slice of the 3-dot potential along the  $x$  axis with the single-electron ground state probability. (b): masked potentials for individual pairs of quantum dots.

In the subfigure 3.5a, the single-electron ground state probability density  $|\Psi_0(x)|^2$  is overlaid on top of the 1D slice of a 3-electron potential landscape. The density is clearly distributed across all three quantum dots; therefore, the single-electron spectrum  $\{\Psi(x, z)\}$  of  $U(x, z)$  cannot adequately describe isolated electrons. This justifies the need to manually separate certain dots by masking them with high energy values (subfigure 3.5b) to obtain correct wavefunctions. The  $x$  coordinates for mask borders correspond to the local maxima



of the potential function from subfigure 3.5a. Because the positions and shapes of the tunnel barriers are influenced by all gate voltage values, our choice of masking procedure preserves the information about cross-coupling between the dots while making the wavefunctions of the subsystems directly computable.

### 3.4.2 Determination of the many-electron energy spectrum

Solving a many-electron problem is the primary task of Coulomb module in QuDiPy. The many-electron Hamiltonian with Coulomb interaction energy terms for all pairs of electrons can be written in the second quantization form:

$$\hat{H} = \sum_i \varepsilon_i c_i^\dagger c_i + \frac{1}{2} \sum_{ijkl} \langle ij|v|kl\rangle c_i^\dagger c_j^\dagger c_l c_k, \quad v = \frac{e^2}{4\pi\epsilon_0\epsilon_r|\vec{r}_2 - \vec{r}_1|}. \quad (3.3)$$

Here,  $\{|i\rangle\} \equiv \{|\Psi_{i'}(\vec{r})\rangle\} \otimes \{|\chi_{m_s}\rangle\}$  is the single-electron spin-orbit eigenbasis with the energy eigenvalues  $\{\varepsilon_i\}$  for the specified potential energy landscape (and thus single-electron Hamiltonian). The magnetic quantum number for each electron can have the values  $m_s = \pm\frac{1}{2}$ .

Since Coulomb potential becomes divergent at small separations between electrons, the evaluation of Coulomb interaction matrix elements (CMEs)  $\langle ij|v|kl\rangle$  with high precision is a nontrivial problem. To achieve this, we develop a modified Linear Combination of Harmonic Orbitals (LCHO) [5] full configuration interaction (CI) method, presented in our article [1]. For this, we approximate the orbital components of single-electron functions by a 2D basis of radially symmetric harmonic orbitals (HOs):

$$\phi_{nm}(x, z) = \phi_n(x)\phi_m(z), \quad \phi_q(s) = \frac{1}{\sqrt{2^q q!}} \left(\frac{m^* \omega}{\pi \hbar}\right)^{\frac{1}{4}} \exp\left(-\frac{m^* \omega s^2}{2\hbar}\right) H_q\left(\sqrt{\frac{m^* \omega}{\hbar}} s\right), \quad (3.4)$$

where  $H_q(s)$  is a Hermite polynomial of the order  $q$ , and  $\omega$  is the harmonic frequency. We emphasize that unlike in [5], all quantum dots are described by a single basis in our proposal, which is expected to give computational speedup. Then, the approximation to the lowest  $K$  single-electron orbital states  $|\Psi_j\rangle$  is given by a truncated basis transform:

$$|\Psi_j\rangle \approx \sum_{i=1}^M A_{ij} |\phi_i\rangle, \quad A_{ij} = \langle \phi_i | \Psi_j \rangle \quad (3.5)$$

where  $i, j$  are composite indices for  $\{n, m\}$ , and  $M = M_x M_z$  is the total number of 2D HO states  $|\phi_i\rangle$  in the truncated basis. Obviously, the relation (3.5) approaches identity for

larger  $M, K$ ; typically,  $M \gg K$  is required for good convergence. Thus, if we calculate the CMEs in the HO basis  $\langle \alpha\beta | v | \gamma\delta \rangle$ , we can directly find their expressions in the single-electron basis with the formula:

$$\langle ij | v | kl \rangle = \langle \chi_i | \chi_k \rangle \langle \chi_j | \chi_l \rangle \sum_{\alpha=1}^M \sum_{\beta=1}^M \sum_{\gamma=1}^M \sum_{\delta=1}^M A_{i\alpha}^* A_{j\beta}^* A_{k\gamma} A_{l\delta} \langle \alpha\beta | v | \gamma\delta \rangle, \quad (3.6)$$

where each Greek letter is a composite index of the type  $|\alpha\rangle \equiv |n_\alpha m_\alpha\rangle$ , etc. The prefactors  $\langle \chi_i | \chi_k \rangle, \langle \chi_j | \chi_l \rangle$  emphasize that the spin state of electrons does not change upon scattering on the purely orbital Coulomb potential.

The key revelation is that a fully analytic expression exists for CMEs in the harmonic basis. First of all, their values are strictly zero if either  $n_\alpha + n_\beta + n_\gamma + n_\delta$ , or  $n_\alpha + n_\beta + n_\gamma + n_\delta$  are odd numbers. Otherwise, the expression reads as:

$$\begin{aligned} \langle \alpha\beta | v | \gamma\delta \rangle &= \langle n_\alpha m_\alpha n_\beta m_\beta | v | n_\gamma m_\gamma n_\delta m_\delta \rangle \\ &= \frac{e^2}{4\pi\epsilon_0\epsilon_r} \int d\vec{r}_1 d\vec{r}_2 \phi_\alpha^*(\vec{r}_1) \phi_\beta^*(\vec{r}_2) \frac{1}{|\vec{r}_2 - \vec{r}_1|} \phi_\gamma(\vec{r}_1) \phi_\delta(\vec{r}_2) \\ &= \sqrt{\frac{m^*\omega}{\hbar}} \frac{e^2}{4\pi\epsilon_0\epsilon_r} \frac{\sqrt{\pi} (-1)^{n_\alpha + m_\alpha + n_\gamma + m_\gamma}}{\sqrt{n_\alpha! m_\alpha! n_\beta! m_\beta! n_\gamma! m_\gamma! n_\delta! m_\delta!}} \sum_{p_1=0}^{\min(n_\alpha, n_\gamma)} p_1! \binom{n_\alpha}{p_1} \binom{n_\gamma}{p_1} \\ &\quad \times \sum_{p_2=0}^{\min(m_\alpha, m_\gamma)} p_2! \binom{m_\alpha}{p_2} \binom{m_\gamma}{p_2} \sum_{p_3=0}^{\min(n_\beta, n_\delta)} p_3! \binom{n_\beta}{p_3} \binom{n_\delta}{p_3} \\ &\quad \times \sum_{p_4=0}^{\min(m_\beta, m_\delta)} p_4! \binom{m_\beta}{p_4} \binom{m_\delta}{p_4} (-1)^p \frac{(2p-1)!! (2p-a-1)!! (a-1)!!}{2^{2p} p!}, \end{aligned} \quad (3.7)$$

where the variables  $a = n_\alpha + n_\beta + n_\gamma + n_\delta - 2p_1 - 2p_3$ ,  $2p = a + m_\alpha + m_\beta + m_\gamma + m_\delta - 2p_2 - 2p_4$  are introduced, and  $k!! = k(k-2) \cdots 3 \cdot 1$  is the double factorial for odd  $k$  with  $(-1)!! \equiv 1$ .

Once all CMEs in the single electron spin-orbit basis are found using formulas (3.5) and (3.6), we use the full CI approach to find the many-electron eigenenergies and eigenstates. If the total number of electrons in the quantum dots is  $N$ , we construct all possible  $N$ -electron configurations of all the  $2K$  spin-orbital states. Then, the Hamiltonian 3.3 is explicitly rewritten in the configuration basis and diagonalized. Since the total number of such configuration states scales according to  $n_c = \binom{2N}{K} = \frac{(2N)!}{K!(2N-K)!}$ , this part of the calculation is very numerically intensive. However, as noted before, scattering on Coulomb potential does not change the electron spin state, and the CME value (3.6) does not otherwise depend on the actual spin projections  $|\uparrow\rangle$  or  $|\downarrow\rangle$ . This means that the absolute value

of total spin  $|S_z|$  is a conserved quantum number of the many-electron system, and so its energy spectrum is degenerate. Therefore, we can restrict the configuration basis to an appropriate  $|S_z|$  subspace. This considerably speeds up the calculations, as only the lowest energy levels are sufficient to construct spin and Hubbard Hamiltonians (we elaborate on this matter in subsection 3.4.3).

The computation advantages of our LCHO-CI approach are twofold. First of all, the harmonic frequency  $\omega$  factors out of the expression for CMEs in the HO basis (3.7). This means that a typically very large matrix of CMEs  $C_{\text{HO}}$  can be calculated only once for  $\omega = 1$ , and then simply scaled by  $\sqrt{\omega}$ . Secondly, since we have not imposed any restrictions on the value of  $\omega$  from the beginning, we have freedom to optimize it to achieve better overlap between single-electron and harmonic bases. This is done by solving a trivial single-variable minimization problem:

$$\min_{\omega} f_{\min}(\omega) = \min_{\omega} 1 - \frac{1}{N'} \sum_i^{N'} \sum_j^M |\langle \xi_i | \phi_j(\omega) \rangle|^2, \quad (3.8)$$

where  $N' < N$  is a user-defined number of single-electron states to use. Truncating the orbital eigenbasis does not significantly alter the optimal values of  $\omega$  but allows for a faster minimization. The improvement to the overlap by orders of magnitude is showcased in figure 3.6, where a double quantum dot defined by an analytic quartic potential:

$$U(x, z) = \frac{m^* \omega_0^2}{2} \left[ \frac{1}{4d^2} (x^2 - d^2)^2 + z^2 \right] \quad (3.9)$$

is simulated. The parameters used for the figure are  $N' = 6$ ,  $m^* = 0.191m_0$  (silicon),  $\hbar\omega_0 = 0.375$  meV, and  $d = 50$  nm. Different numbers of HO basis states are indicated with color: as expected, higher values give better overlap with the single-electron basis.

Unfortunately, if the harmonic frequencies along  $x$  and  $z$  are different:  $\omega_x \neq \omega_z$ , they do not factor out of expression (3.7). Although we prove in the appendix of the paper [1] that the CMEs can be still analytically expressed in terms of the arithmetic-geometric

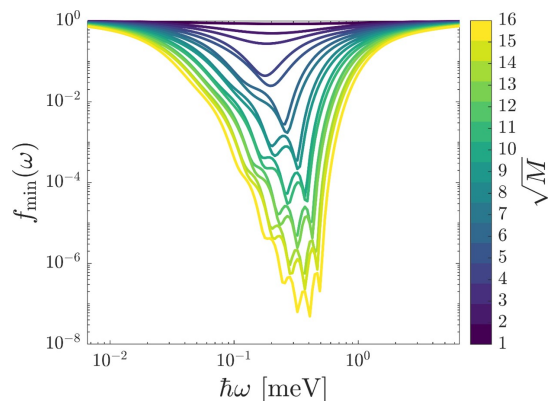


Figure 3.6: Dependence of the optimization function  $f_{\min}(\omega)$  on  $\omega$  and the size of the harmonic orbital basis ( $M_x M_y = M$ ). Reproduced from [1]

mean function  $M(\omega_x, \omega_z)$ , we lose the computational advantage of pre-calculating  $C_{\text{HO}}$  only once. The efficient algorithm for the HOs with  $\omega_x \neq \omega_z$  would be particularly relevant for the elongated chains of quantum dots such as in our computer architecture [65]. It is also a necessity for upgrading to a full 3D simulation, since the electrons are localized much stronger vertically (along  $y$  axis) than horizontally (in  $xz$  plane). For this, we suggest further computational improvement for the CME matrix evaluation by pointing out that expression (3.7) is invariant under the following transformations:

$$\begin{aligned}
(1) \quad n_\alpha &\Leftrightarrow n_\gamma, & (2) \quad m_\alpha &\Leftrightarrow m_\gamma, \\
(3) \quad n_\beta &\Leftrightarrow n_\delta, & (4) \quad m_\beta &\Leftrightarrow m_\delta, \\
(5) \quad \begin{cases} n_\alpha &\Leftrightarrow n_\beta, \\ n_\gamma &\Leftrightarrow n_\delta, \end{cases} & (6) \quad \begin{cases} m_\alpha &\Leftrightarrow m_\beta, \\ m_\gamma &\Leftrightarrow m_\delta, \end{cases} & (3.10) \\
(7) \quad \text{All at once: } n_\iota &\Leftrightarrow m_\iota, \quad \iota \in \{\alpha, \beta, \gamma, \delta\}.
\end{aligned}$$

If we roughly estimate that each symmetry allows us to calculate two times fewer matrix elements, then the number of required mathematical operations will be reduced by a factor of  $2^7 = 128$  (the correct number is somewhat smaller). Meanwhile, the code runtime is guaranteed to decrease even more, since smaller numbers of loops require lesser memory allocations. We anticipate an even more significant speed-up if memory-efficient algorithms for sparse matrices are utilized. The code implementation of (3.10) is being tested now, but the preliminary results already give the computational time reduction by three orders of magnitude. Conceptually, this translates  $\sim 10$  hours of  $C_{\text{HO}}$  evaluation with Matlab using conventional algorithm with  $M = 16^2$ , reported in [1], to  $\sim 30$  seconds.

Therefore, with the appropriate implementation of the symmetries (3.10), the direct evaluation of  $C_{\text{HO}}$  will no longer be a bottleneck for a full CI calculation in any system. Remarkably, all transformations from (3.10) except (7) remain applicable for the HOs with  $\omega_x \neq \omega_z$ . The efficient evaluation of CMEs in this case paves the way to high-precision full CI calculations for arbitrary potential landscapes in 2 and, possibly, 3 dimensions.

### 3.4.3 Construction of effective Hamiltonians

#### Spin parameters

The extraction of voltage-dependent spin parameters from `nextnano++` potential landscapes is relatively straightforward. In particular, Stark Shift module of `QuDiPy` does

not even require any many-electron calculations. The deviation  $g$ -factor of the  $i^{\text{th}}$  electron depends quadratically on the out-of-plane component of the electric field [54, 65]:

$$\frac{g_i(\mathcal{E}_y)}{g_i(\mathcal{E} = 0)} - 1 = \eta_2 \langle \psi_i | \mathcal{E}_y^2 | \psi_i \rangle, \quad \eta_2 \approx 2.2 \text{ nm}^2 \text{ V}^{-2} \text{ for silicon.} \quad (3.11)$$

Each single-electron wavefunction  $|\psi_i\rangle$  for  $i \in \{1, \dots, N\}$  is directly calculated as a ground state in the potential energy landscape  $U_i(x, z)$  with all potential wells except the  $i^{\text{th}}$  one being masked.

Unlike in the previous case, Exchange module needs two-electron spectra to evaluate exchange couplings.  $U(x, z)$  is “partitioned” into  $N - 1$  functions  $U_{j,j+1}(x, z)$ , where all but the  $j^{\text{th}}$  and  $j+1^{\text{st}}$  dots are masked. For each of the potentials  $U_{j,j+1}$ , a two-electron energy spectrum  $\{E_{j,j+1}^{(2)}\}$  is found. The corresponding exchange parameter for the  $j^{\text{th}}$  pair is calculated as the difference between the ground and first excited state energies:

$$J_j = E_{j,j+1,e}^{(2)} - E_{j,j+1,g}^{(2)}. \quad (3.12)$$

For conciseness, we will henceforth denote the ground state energies of the appropriate systems as  $\varepsilon_{\dots}^{(\dots)}$ .

## Hubbard parameters

Next, we construct a simplified Hubbard Hamiltonian for an  $N$ -dot chain based on the work [73]:

$$H_\mu = - \sum_{\sigma=\uparrow,\downarrow} \left[ \sum_{i=1}^N \mu_i n_{i,\sigma} + \sum_{j=1}^{N-1} t_{j,j+1} \left( c_{j,\sigma}^\dagger c_{j+1,\sigma} + h.c. \right) \right] + \sum_{i=1}^N u_i n_{i,\uparrow} n_{i,\downarrow} + \sum_{\sigma_1, \sigma_2 \in \{\uparrow, \downarrow\}} \sum_{j=1}^{N-1} u'_j n_{i,\sigma_1} n_{j,\sigma_2} \quad (3.13)$$

Here,  $\mu_i$  is the chemical potential of the  $i^{\text{th}}$  electron,  $t_{j,j+1}$  is the tunnel coupling (or hopping) for the  $j^{\text{th}}$  pair of dots,  $u_i$  and  $u'_{i,j}$  are the onsite and interdot Coulomb repulsion energies, respectively. In general, the number operator  $n_{i,\sigma} = c_{i,\sigma}^\dagger c_{i,\sigma}$  counts the electrons occupying the highest orbital, but we restrict it to the case when no more than 2 electrons can be in the dot, in agreement with all node operations in our architecture [65]. Additionally, in the Hamiltonian 3.13, we ignore second-order contributions from exchange,

pair hopping and occupation-modulated hopping. Furthermore, we treat all  $t_{j,j+1}$  terms as real variables, ignoring their possible complex phases. On the contrary, we keep all terms for the interdot Coulomb repulsion  $u'_{i,j}$  (i.e. *not only* for the adjacent dots), since this is a long-range interaction. Indeed, the results in the paper [73] suggest that for a 2-electron system,  $u'_{1,2}$  is typically an order of magnitude larger than  $t_{1,2}$ . However, we can always truncate such terms with  $|i - j| > 1$  when high precision is not required.

The values of chemical potentials and Coulomb repulsion terms are greatly influenced by the strengths of electron-electron interactions; hence, their evaluation requires many-body energy spectra of quantum dot subsystems. The procedure, however, is straightforward and naturally derives from the definitions of these parameters. It is summarized in table 3.2. Whenever a tilde is drawn on top of the potential energy landscape  $\tilde{U}_{k_1, k_2, \dots}$  or the ground-state energy  $\tilde{\varepsilon}_{k_1, k_2, \dots}$ , it means that the dots with indices  $k_1, k_2, \dots$  are masked. If the tilde is not drawn,  $k_1, k_2, \dots$  dots are the only ones that are *unmasked*.  $\varepsilon_\Sigma$  is the ground state energy of the unmasked potential  $U(x, z)$ .

To calculate the tunnel coupling  $t_{j,j+1}$ , we employ a simple 2-level system model, analogous to the one used in references [67, 76, 77]. Electron tunneling is a single-electron effect and can thus be described by single-electron energies only. Therefore, all superscripts “(1)” will be dropped henceforth. First, we calculate single-electron energies of each isolated dot within the  $j^{\text{th}}$  pair:

$$U_j(x, z) \rightarrow \varepsilon_j, \quad U_{j+1}(x, z) \rightarrow \varepsilon_{j+1},$$

and define their average energy value and detuning:

$$\bar{\varepsilon} = \frac{\varepsilon_j + \varepsilon_{j+1}}{2}, \quad \Delta\varepsilon = |\varepsilon_j - \varepsilon_{j+1}|. \quad (3.14)$$

Then, a two-level model Hamiltonian for the  $j^{\text{th}}$  dot pair in the presence of tunnel coupling will read as:

$$H_{\text{TL}} = \begin{pmatrix} \bar{\varepsilon} + \frac{\Delta\varepsilon}{2} & -t_{j,j+1} \\ -t_{j,j+1} & \bar{\varepsilon} - \frac{\Delta\varepsilon}{2} \end{pmatrix} \quad (3.15)$$

It is easy to verify that the eigenenergies of this Hamiltonian are:

$$E_{e,g} = \bar{\varepsilon} \pm \frac{\sqrt{\Delta\varepsilon^2 + 4t^2}}{2}, \quad E_e - E_g = \sqrt{\Delta\varepsilon^2 + 4t^2}. \quad (3.16)$$

However, the same single-electron spectrum (up to an additive constant  $\bar{\varepsilon}$ ) can be found directly by masking all dots except  $j^{\text{th}}$  and  $j+1^{\text{st}}$  ones in the original potential landscape  $U(x, z)$ :

$$U_{j,j+1}(x, z) \rightarrow \{E_{j,j+1,1}, E_{j,j+1,2}, \dots\} \quad (3.17)$$

By combining the results (3.14), (3.16) and (3.17), we obtain the final formula for the tunnel coupling:

$$t_{j,j+1} = \frac{1}{2} \sqrt{\left(E_{j,j+1,2}^{(1)} - E_{j,j+1,1}^{(1)}\right)^2 - \left(\varepsilon_j^{(1)} - \varepsilon_{j+1}^{(1)}\right)^2} \quad (3.18)$$

	Definition	Procedure
$\mu_i$	Energy needed to remove an electron from the $i^{\text{th}}$ dot	<ol style="list-style-type: none"> <li>All <math>N</math> electrons in place, solve <math>N</math>-electron problem: <math>U(x, z) \rightarrow \varepsilon_{\Sigma}^{(N)}</math></li> <li>Mask only the <math>i^{\text{th}}</math> dot, solve <math>N - 1</math>-electron problem: <math>\tilde{U}_i(x, z) \rightarrow \varepsilon_i^{(N-1)}</math></li> <li><math>-\mu_i = \varepsilon_{\Sigma}^{(N)} - \varepsilon_i^{(N-1)}</math></li> </ol>
$u_i$	Energy contribution due to Coulomb repulsion between two electrons in the $i^{\text{th}}$ dot	<ol style="list-style-type: none"> <li>Isolate the <math>i^{\text{th}}</math> dot: <math>U_i(x, z)</math></li> <li>Find energy of a single electron with either spin (no interaction): <math>\varepsilon_i^{(1)}</math></li> <li>Find two-electron energy (with interaction): <math>\varepsilon_i^{(2)}</math></li> <li><math>u_i = \varepsilon_i^{(2)} - 2\varepsilon_i^{(1)}</math></li> </ol>
$u'_{ij}$	Energy contribution due to Coulomb repulsion between one electron in the $i^{\text{th}}$ dot, and one electron in the $j^{\text{th}}$ dot	<ol style="list-style-type: none"> <li>Find energies of noninteracting electrons in two isolated dots: <math>U_i(x, z) \rightarrow \varepsilon_i^{(1)}, \quad U_j(x, z) \rightarrow \varepsilon_j^{(1)}</math></li> <li>Mask all dots except <math>i^{\text{th}}, j^{\text{th}}</math>, find 2-electron energy: <math>U_{i,j}(x, z) \rightarrow \varepsilon_{i,j}^{(2)}</math></li> <li><math>u'_{i,j} = \varepsilon_{i,j}^{(2)} - \left(\varepsilon_i^{(1)} + \varepsilon_j^{(1)}\right)</math></li> </ol>

Table 3.2: Algorithm for the extraction of electron chemical potentials and Coulomb repulsion terms from the potential energy landscape  $U(x, y)$ .

Once the values of all variables  $\mu, t, u, u'$  are known, the Hubbard model Hamiltonian 3.13 can be diagonalized. The obtained spectrum contains the information about energetic favorability of the system spin-charge states. This data is used to restrict the plunger and tunnel gate voltage pulses to the regime of charge configuration stability. The corresponding cost function minimization formalism is presented in section 4.2 of the following chapter.

### 3.4.4 Spin dynamics simulation

#### Spin Hamiltonian

Since the qubit operations in our architecture [65] include not only unitary gates but also measurements and qubit loads, we design a spin evolution simulation algorithm capable of dealing with variable numbers of qubits. Let us consider a chain of  $N$  quantum dots, with no more than 1 electron in each of them. Then, in the lab frame, the system spin Hamiltonian reads as follows:

$$\begin{aligned}
 H_L = & \sum_{j=1}^N \hat{\delta}_j \underbrace{\frac{g_j(t)}{2} \mu_B B_0 Z_j}_{\text{Zeeman}} + \sum_{j=1}^{N-1} \hat{\delta}_j \hat{\delta}_{j+1} \underbrace{\frac{J_j(t)}{4} \vec{\sigma}_j \cdot \vec{\sigma}_{j+1}}_{\text{exchange}} \\
 & + \sum_{j=1}^N \delta_j \underbrace{\mu_B B_{\text{RF}}(t) [\cos(\omega_{\text{RF}} t + \phi(t)) X_j + \sin(\omega_{\text{RF}} t + \phi(t)) Y_j]}_{\text{radio frequency field}}, \quad (3.19)
 \end{aligned}$$

where the following parameters are introduced:

- $\hat{\delta}_j = 1$  if there is an electron in the  $j^{\text{th}}$  dot, and  $\hat{\delta}_j = 0$  if the dot is empty. Since removing an electron is equivalent to measuring it without knowing the outcome, we will drop these factors throughout the text. Instead, we will establish an appropriate measurement procedure at the end of this subsection to describe the systems where some of the dots are unpopulated;
- $B_0$  and  $B_{\text{RF}}(t)$  are the static Zeeman field and the envelope of ESR radio frequency (RF) field, respectively;
- $\omega_{\text{RF}} = 2\pi f_{\text{RF}}$  and  $\phi(t)$  are the RF field frequency and phase, respectively;
- $J_j(t)$  is the voltage-controlled parameter of exchange between  $j^{\text{th}}$  and  $j+1^{\text{st}}$  dots;



- $\vec{\sigma}_j = \{X_j, Y_j, Z_j\}$  is the Pauli vector of the  $j^{\text{th}}$  spin;
- $g_j(t) \equiv 2 + \delta g_j(t)$  is the voltage-controlled in-plane  $g$ -factor of  $j^{\text{th}}$  electron. Since the out-of-plane  $g$ -factor is coupled to a much weaker ESR field, its deviations do not lead to physically significant effects and are thus ignored.

Each term in equation (3.19) is a Kronecker product of  $N$  matrices  $2 \times 2$ . To simplify notation, we drop the identity operators in Kronecker products, e.g.:

$$Z_k \equiv \left( \bigotimes_{i=1}^{k-1} \mathbb{1}_i \right) \otimes Z_k \otimes \left( \bigotimes_{i=k+1}^N \mathbb{1}_i \right), \quad \text{where} \quad \mathbb{1} = \begin{pmatrix} 1 & 0 \\ 0 & 1 \end{pmatrix} \quad (3.20)$$

We adhere to this convention throughout this section.

For the simulation, the Hamiltonian (3.19) and density matrix  $\rho$  are transformed into rotation frame (cf. sec. 1.2) in the following way:

$$\rho_{\text{R}} \equiv \rho = R \rho_{\text{L}} R^\dagger, \quad H_{\text{R}} = R H_{\text{L}} R^\dagger + i \hbar \dot{R} R^\dagger, \quad (3.21)$$

$$R = \bigotimes_{j=1}^N \exp \left\{ \frac{i}{2} \omega_{\text{RF}} t Z_j \right\} = \bigotimes_{j=1}^N \left( \cos \frac{\omega_{\text{RF}} t}{2} + i \sin \frac{\omega_{\text{RF}} t}{2} Z_j \right) = \begin{pmatrix} e^{\frac{i}{2} \omega_{\text{RF}} t} & 0 \\ 0 & e^{-\frac{i}{2} \omega_{\text{RF}} t} \end{pmatrix}^{\otimes N} \quad (3.22)$$

By substituting (3.22) into (3.21) and neglecting fast-oscillating terms, we obtain the spin Hamiltonian (normalized by  $\hbar$ ) in the rotating wave approximation:

$$\begin{aligned} \mathcal{H} = H_{\text{R}} / \hbar = \sum_{j=1}^N \left\{ \frac{1}{2} \left[ \left( 1 + \frac{\delta g_j(t)}{2} \right) \omega - \omega_{\text{RF}} \right] Z_j + \frac{\Omega(t)}{2} (\cos \phi(t) X_j + \sin \phi(t) Y_j) \right\} + \\ + \sum_{j=1}^{N-1} \frac{J_j(t)}{4\hbar} \vec{\sigma}_j \cdot \vec{\sigma}_{j+1}, \quad (3.23) \end{aligned}$$

Here,  $\omega = \frac{2\mu_{\text{B}} B_0}{\hbar}$  is the Larmor frequency,  $\Omega(t) = \frac{2\mu_{\text{B}} B_{\text{RF}}(t)}{\hbar}$  is the Rabi frequency.

Even though we essentially describe a single node with  $N$  dots, it is equally possible to construct such Hamiltonian for any network of interconnected nodes so long as all  $\delta g_i$  and  $J_j$  parameters are calculated prior.

## Quantum master equation

To simulate the time evolution of the spin system, we use a master equation in Lindblad form [78] in the rotation frame:

$$\frac{d\rho}{dt} = i [\rho, \mathcal{H}] + \sum_{\alpha=1}^3 \sum_{j=1}^N 2L_{\alpha,j} \rho L_{\alpha,j}^\dagger - \left\{ L_{\alpha,j}^\dagger L_{\alpha,j}, \rho \right\}, \quad (3.24)$$

Here, the Lindblad operators are defined in the following way:

$$L_{1,j} = \sqrt{\frac{p_j}{2T_1}} \sigma_{+,j} \quad L_{2,j} = \sqrt{\frac{1-p_j}{2T_1}} \sigma_{-,j} \quad L_{3,j} = \frac{Z_j}{2\sqrt{T_2}}, \quad (3.25)$$

The first two operators describe the spin relaxation to the states  $|\uparrow\rangle$  and  $|\downarrow\rangle$ , respectively, with the characteristic relaxation time  $T_1$  and  $p_j$  being the statistical probability of finding  $j^{\text{th}}$  electron in the state  $|\uparrow\rangle$ . The third Lindblad operator represents dephasing with the characteristic time  $T_2$ . Since Zeeman splitting determines the largest energy scale in the system, we assume Boltzmann distribution for  $p_j$ :

$$E_{|\uparrow\rangle} - E_{|\downarrow\rangle} \approx \hbar\omega; \quad p_j = p \approx \frac{1}{\exp\left(\frac{\hbar\omega}{k_B T_e}\right) + 1} \quad \text{for all } j, \quad (3.26)$$

where  $T_e$  is the electron temperature,  $k_B = 1.380\,649 \cdot 10^{-23} \frac{J}{K}$  is the Boltzmann constant.

By combining formulas (3.23), (3.24) and (3.25), we can already write the expression for the master equation. However, we rewrite some terms in (3.24) first using the identities:

$$\sigma_{+,j} \sigma_{-,j} = 2 \cdot \mathbb{1} + 2Z_j, \quad [\sigma_{+,j}, \sigma_{-,j}] = 4Z_j,$$

to achieve an additional computational speedup. With this, we obtain the final expression for the master equation and the corresponding initial value problem (IVP), numerically solved by the Evolution module of QuDiPy:

$$\begin{aligned} \frac{d\rho}{dt} = F(\rho, t) = & i \left[ \rho, \frac{\omega}{4} \sum_{k=1}^N \delta g_k(t) Z_k + B_{\text{RF}}(t) \left( \cos \phi(t) \frac{\mu_B}{\hbar} \sum_{k=1}^N X_k + \sin \phi(t) \frac{\mu_B}{\hbar} \sum_{k=1}^N Y_k \right) \right] \\ & + \left[ \rho, \sum_{k=1}^{N-1} \frac{i}{4\hbar} \vec{\sigma}_k \cdot \vec{\sigma}_{k+1} J_k(t) \right] + \left[ \rho, \frac{i}{2} (\omega - \omega_{\text{RF}}) \sum_{k=1}^N Z_k \right] + \frac{1}{2T_2} \sum_{k=1}^N Z_k \rho Z_k \\ & + \frac{p}{T_1} \sum_{k=1}^N \sigma_{+,k} \rho \sigma_{-,k} + \frac{1-p}{T_1} \sum_{k=1}^N \sigma_{-,k} \rho \sigma_{+,k} + \frac{2p-1}{T_1} \sum_{k=1}^N Z_k - \left( \frac{2}{T_1} + \frac{1}{2T_2} \right) N\rho; \\ \rho(t=0) = & \rho_0. \end{aligned} \quad (3.27)$$

The computational speedup for the master equation simulation is achieved in the following way. At the beginning, an auxiliary function constructs an array of time-independent Pauli matrices  $(X_k, Y_k, Z_k, \sigma_{\pm,k})$  and the expressions colored in (3.27) for all  $k \in [1, n]$ , where  $n \in [1, N_0]$ . The reason why the matrices for different values of  $n$  are calculated is that  $N$  is not fixed, i.e. the electrons could be measured or loaded. The function that constructs the right-hand side of (3.27) at each point of time retrieves the values of pre-calculated matrices and multiplies them by time-dependent parameters  $B_{\text{RF}}(t), \delta g_k(t), J_k(t)$ , etc. This significantly speeds up the computation since Kronecker products are not recalculated at each iteration. Our simulator numerically integrates the IVP (3.27) using the 4<sup>th</sup> order Runge-Kutta method. If desired, a better precision can be achieved with higher-order methods, with the optimization describe above being applicable to all of them.

### Qubit measurements and loads

The implementation of the measurement of the  $k^{\text{th}}$  qubit depends on whether its measurement outcome  $|M_k\rangle$  is known or not. In these two cases, the system density matrix is redefined in the following way:

$$\begin{aligned} \text{Outcome known: } \rho &\rightarrow \text{Tr}_k \left( \frac{\langle M_k | \rho | M_k \rangle}{\text{Tr} \langle M_k | \rho | M_k \rangle} \right). \\ \text{Outcome not known: } \rho &\rightarrow \text{Tr}_k \rho, \end{aligned} \quad (3.28)$$

Here,  $\text{Tr}$  denotes trace, and  $\text{Tr}_k$  denotes a partial trace with respect to the  $k^{\text{th}}$  qubit. The Hamiltonian and Lindblad operators are changed according to the substitution:

$$\mathcal{H} \rightarrow \frac{1}{2} \text{Tr}_k (\mathcal{H}), \quad L_{\alpha, j \neq k} \rightarrow \frac{1}{2} \text{Tr}_k (L_{\alpha, j \neq k}), \quad (3.29)$$

with  $N$  being replaced by  $N - 1$ . The factor  $\frac{1}{2}$  appears because  $X, Y, Z$  are traceless, and  $\text{Tr}(\mathbb{1}) = 2$ . Note that the Hamiltonian transforms as a whole, whereas the Lindblad operators need to be redefined individually. Therefore, in practice it is easier to recalculate each  $L_{\alpha, j}$  individually with formula (3.25) for  $j = \overline{1, N - 1}$ .

It is simpler to describe loads of new qubits into the system when we populate the neighboring dots one by one left to right or vice versa. For example, when we load an

electron in a state  $\rho_{N+1}$  from the right, the matrices for  $N$  qubits are changed as follows:

$$\begin{aligned} \rho \rightarrow \rho \otimes \rho_{N+1}, \quad \mathcal{H} \rightarrow \mathcal{H} \otimes \mathbb{1} + \frac{1}{2} \left[ \left( 1 + \frac{\delta g_{N+1}(t)}{2} \right) \omega - \tilde{\omega} \right] Z_{N+1} + \frac{J_N(t)}{4\hbar} \vec{\sigma}_N \cdot \vec{\sigma}_{N+1} \\ + \frac{\Omega(t)}{2} \left( \cos \phi(t) X_{N+1} + \sin \phi(t) Y_{N+1} \right) \end{aligned} \quad (3.30)$$

and  $N$  is replaced by  $N+1$  afterwards. The Lindblad operators  $L_{\alpha, N+1}$  defined by (3.25) are added to the set, and the existing ones with  $j \leq N$  are changed simply as  $L_{\alpha, j} \rightarrow L_{\alpha, j} \otimes \mathbb{1}$ . If qubits are loaded in the reverse order, or the order of loads is mixed, formula (3.30) can still be used provided that transforms (3.28) and (3.29) are modified. If we record the physical locations of electrons in the chain  $\{l_k\}$  with respect to their  $k^{\text{th}}$   $2 \times 2$  contributions to the total density matrix, the only necessary correction is using  $\text{Tr}_{l_k}$  instead of  $\text{Tr}_k$ .

### Additional capabilities

If specified, the simulator can additionally return the values of matrix purity  $\text{Tr}(\rho^2)$  and fidelity with respect to the specified reference matrix  $\rho'$  (initial, expected after the pulse, etc.):

$$\mathcal{F}(\rho, \rho') = \left( \text{Tr} \sqrt{\rho^{\frac{1}{2}} \rho' \rho^{\frac{1}{2}}} \right)^2 \quad (3.31)$$

The other feature is to output the one-qubit density submatrices and their Bloch vectors during the pulse (by tracing out the contributions of irrelevant electrons, according to formula (3.28)).

## 3.5 Summary of chapter 3

In summary, a software package was developed for modeling semiconductor quantum dots and, particularly, simulating node operations in a Si quantum computer architecture [65]. The main results presented in this chapter are as follows:

1. A modified Linear combination of harmonic orbital, configuration interaction (LCHO-CI) algorithm for solving many-electron problems in 2D quantum dot networks, reported in our article [1], is presented. An additional 2-3 order of magnitude improvement to the efficiency of the algorithm published earlier is suggested, offering the prospect of high-precision simulations of elongated dot networks with modest computational capabilities.
2. A method of processing electric potential and field landscapes to extract effective parameters, produced by realistic nanodevice geometries, is proposed. The method relies on the system orbital energy spectra and is capable of automatically separating contributions of individual electron subsystems without losing cross-coupling information. It is utilized to construct effective spin and Hubbard Hamiltonians of the electron system.
3. The quantum master equation formalism is adapted to efficiently simulate the dissipative evolution of spin qubits, their measurements and loads within the computer architecture [65].
4. The proposed algorithms are incorporated into an open-source, versatile and efficient quantum dot simulation package QuDiPy, which is currently under development. The voltage and ESR pulse engineering for the controlled operation of computational nodes from the architecture [65] are among the capabilities of QuDiPy.

# Chapter 4

## A novel constrained method for efficient deterministic control pulse engineering in a silicon spin-qubit architecture

### 4.1 Introduction

The field optimal pulse design for the best possible control of quantum systems has gained significant progress over the past decades [79]. However, the realization of high-fidelity quantum gates in our spin qubit architecture is associated with an inherent challenge. Indeed, the effective parameters of the Hamiltonian (3.23) that determine the evolution of the electron spin state (deviation  $g$ -factors, exchange couplings) nontrivially depend on the physically controlled parameters (plunger and tunnel gate voltages). This makes the control problem highly nonlinear so that advanced pulse engineering techniques should be used.

The approaches for quantum gate preparation [80] mostly rely on pulse temporal discretization (GRAPE, Krotov method) or on optimizing its spectrum in a chosen basis (GOAT, CRAB). Each of these methods has the advantage of being general and yielding the pulse profile at all points in time. However, it comes at a high cost of multivariate optimization with multiple acts of matrix exponentiation, numerical integration of systems of differential equations, or direct search, depending on the method. One possibility to reduce the computational cost is to devise an approach that is less general by optimizing

over a narrow space of functions. The *goal* of this chapter is to develop a novel method of pulse engineering, applicable to our choice of silicon spin qubit architecture [65], that relies on an optimal set of constraints. They ensure that the voltage pulse sequences can be engineered efficiently and unambiguously within the physical limitations of the system operation.

Section 4.2 formally defines a control problem for engineering optimal pulses of the desired kind. The definition incorporates physical mechanisms that lead to non-optimality and thus should be minimized. In section 4.3, we engineer high-fidelity single and two-qubit gates with the spin evolution being controlled by time-dependent effective parameters: exchange couplings, deviation  $g$ -factors, and the global ESR field. We develop approaches to minimize the duration of control pulses that realize quantum circuits of certain types in section 4.4. The approaches include choosing between equivalent qubit rotations, running gates in parallel and/or simultaneously on the same sets of qubits. In both sec. 4.3 and 4.4, we design time dependencies for the effective parameters only, presuming that individual one or two-qubits gates can be in principle realized physically with high fidelity. We reserve the discussion of how to map the time-dependent effective parameters to the experimentally controlled gate voltages for the section 4.5, where a general voltage and ESR pulse engineering algorithm is presented. In particular, the realization of direct mapping between physical and effective parameters of spin evolution puts our work beyond the control schemes capable of only designing effective pulses, such as the one from [81] proposed for a similar computer architecture. Section 4.6 presents illustrative simulations of voltage pulses using the developed approaches. Section 4.7 gives a summary of the results.

All the following sections of this chapter consist of original author's contributions unless noted otherwise.

## 4.2 Pulse engineering method

### 4.2.1 Control problem definition

We formulate an optimal control problem for the voltage and ESR pulse sequences as a minimization problem for a scalar non-negative cost function:

$$f \in [0, \infty) : \quad f \left( \vec{V}(t), \vec{W}(t), B_{\text{RF}}(t), \phi(t) \right) \rightarrow \min, \quad (4.1)$$

where  $\vec{V}, \vec{W}$  is a shorthand notation for  $n$  plunger gate voltages and  $n - 1$  tunnel gate voltages, respectively, and  $T$  is the duration of the pulse. In practice,  $f$  is a weighted sum of simpler cost functions, where each of them describes a different mechanism that leads to non-optimality:

$$f = \sum_i w_i f_i, \quad \sum_i p_i = 1, \quad (4.2)$$

where the weighting factors  $w_i$  are to be chosen empirically. We will discuss the individual contributions that apply to our architecture in the next subsections.

The control parameters can be additionally subject to a set of constraints:

$$\vec{C}_L \leq \vec{\Phi} \left( t, \vec{V}(t), \vec{W}(t), B_{\text{RF}}(t), \phi(t) \right) \leq \vec{C}_R. \quad (4.3)$$

The vectors of bounds  $\vec{C}_L, \vec{C}_R$  follow a general notation, where the case  $C_{L,i} \equiv C_{R,i}$  corresponds to an equality constraint, and a one-sided inequality is realized at  $C_{L/R,i} \equiv \mp \infty$ . The constraints can naturally arise from the physics of the processes in a quantum system, or be user-defined. Importantly, if the set of constraints (4.3) is complete enough to *uniquely* define each of the functions  $\vec{V}(t), \vec{W}(t), B_{\text{RF}}(t), \phi(t)$ , then the problem (4.1) is reduced to the minimization over a discrete set of variables instead of a space of time-dependent functions:

$$f \in [0, \infty) : \quad f \left( \vec{C}_L, \vec{C}_R \right) \rightarrow \min_{\{\vec{C}_L, \vec{C}_R\}}. \quad (4.4)$$

Therefore, a clever choice of constraints may significantly simplify and speed up the optimization problem.

### 4.2.2 Activation function

Before defining an explicit expression for the cost function, it is important to establish rules about which control parameter configurations are to be considered non-optimal, and



how to quantify non-optimality. This is convenient to achieve with the aid of an activation function  $\Xi$ , whose purpose is to discard or select (and transform if needed) the value of another function based on the values of its arguments. When applied on a relevant physical quantity  $\mathcal{K}$  that may or may not correspond to a non-optimal regime, it will decide whether or not to add the contribution to the total cost (4.1). Parenthetically, the concept of activation functions is one of the mainstays of artificial neural networks [82], where they are used to conditionally propagate information through neurons based on the values stored in other neurons.

Suppose there is a system parameter  $x \in [0, 1]$  which should be kept close to zero at all times. To ensure that, we add a term of the following kind to the cost function:

$$\Xi_p(x, \alpha) = \left( \frac{x - 1 + \alpha}{\alpha} \right)^p \Theta(x - 1 + \alpha) = \begin{cases} \left( \frac{x-1+\alpha}{\alpha} \right)^p, & x > 1 - \alpha; \\ 0, & x \leq 1 - \alpha, \end{cases} \quad (4.5)$$

where  $\Theta(x)$  is the Heaviside step function. This expression penalizes values of  $x$  that approach 1 (fig. 4.1). Such a choice of the activation function has a number of advantages:

- The values of  $\Xi_p(x, \alpha)$  span the range  $[0, 1]$  at  $x \in [0, 1]$  with  $\Xi_p(1, \alpha) \equiv 1$ . This is convenient when we want to ensure that  $f \in [0, 1]$  for the physically relevant values of control parameters. Nevertheless, the function is well defined for  $x > 1$  as well, so there will be no discontinuity should the gradient optimization go past the value  $x = 1$ .
- $\Xi_p(1 - \alpha, \alpha) = 0$ , which gives the meaning of a cutoff parameter to  $\alpha$ : activation is nonzero only if  $x$  lies within less than  $\alpha\%$  of its maximal value.
- $\Xi_p(x, \alpha)$  is a nonincreasing function of  $x$ , and the parameter  $p$  allows for tweaking its speed of growth with  $x$ . For simplicity we will always use the values  $p > 1$ : this ensures the function is differentiable at  $x = 0$ , as opposed to the case of  $p \leq 1$  (this is important not to accumulate unexpected numerical error during a gradient-based optimization procedure)

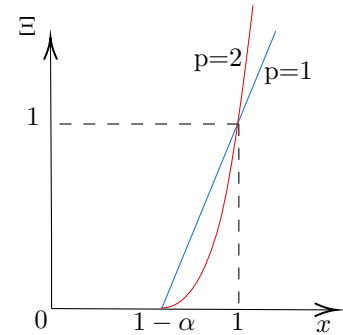


Figure 4.1: Activation function  $\Xi_p(x, \alpha)$ .

The derivative of such activation function reads as:

$$\frac{\partial \Xi_p(x, \alpha)}{\partial x} \equiv \Xi'_p(x, \alpha) = \frac{p(x-1+\alpha)^{p-1}}{\alpha^p} \Theta(x-1+\alpha) = \begin{cases} \frac{p(x-1+\alpha)^{p-1}}{\alpha^p}, & x > 1 - \alpha; \\ 0, & x \leq 1 - \alpha, \end{cases} \quad (4.6)$$

In the field of deep learning,  $\Xi_p(x, \alpha)$  without the horizontal shift is known as a rectified linear unit (ReLU [82]) raised to a power  $p$ .

### 4.2.3 Expression for the cost function

The most important optimality criterion for pulse engineering is high fidelity with respect to the desired quantum transition. We consider only unitary evolution (i.e. case of no dissipation) throughout this chapter. Then, if the evolution operator of the system under its effective Hamiltonian (3.23) is  $U(t)$ , and the matrix of the quantum gate we want to implement is  $U_0$ , then the corresponding expression for fidelity at time  $T$  (i.e. at the end of the pulse) reads as follows:

$$\mathcal{F}[U(T), U_0] = \frac{1}{\dim U} |\text{tr } U^\dagger(T)U_0|, \quad \mathcal{F} \in [0, 1] \quad (4.7)$$

Optimization methods discussed previously (GRAPE, Krotov, etc.) commonly use the infidelity  $f_0 = 1 - \mathcal{F}$  as the first component of the cost function expression (4.2). However, this inevitably complicates the problem in our case, since  $U(t)$  nontrivially depends on the system Hamiltonian, which in turn contains the effective parameters ( $g$ -factors, exchange couplings) not directly controlled experimentally. This difficulty can be avoided if the condition of exact correspondence between  $U(T)$  and  $U_0$  (possibly, up to a desired error  $\varepsilon > 0$ ) is imposed:

$$1 - \mathcal{F}[U(T), U_0] < \varepsilon.$$

This condition implicitly specifies a set of constraints of the type (4.3); their explicit forms for different quantum gates will be derived in the next sections.

Therefore, the cost function in our case will contain only the terms related to the physical limitations of either the quantum system itself, or the experimental facilities:

$$f = w_{\text{CS}}f_{\text{CS}} + w_{\text{BF}}f_{\text{BF}} + w_{\text{VW}}f_{\text{VW}}, \quad w_{\text{CS}} + w_{\text{BF}} + w_{\text{VW}} = 1. \quad (4.8)$$

The first term in the expression above ensures that the configuration of charges in the quantum dots does not change during the pulse; the second and third terms impose limits on the RF radiation losses and sweep rates of voltages, respectively. The expressions for each of the terms  $f_{\text{CS}}, f_{\text{BF}}, f_{\text{VW}}$  are derived below. Photon-assisted tunneling between the electron orbital states is yet another physical phenomenon that needs to be suppressed; however, we do not include the corresponding cost function term in expression (4.8).

## 4.2.4 Stability of charge configuration

Although our goal is to control the evolution of the electron spin states, it is important to remember that voltage sweeps always directly affect their orbital states. Excessive voltage changes can attract new electrons to quantum dots, remove the existing ones, or force them to tunnel from one dot to the other. Therefore, the stability of charge configuration is of utmost importance to ensure the reliability of quantum gate operation. Unfortunately, the charge stability regions are not known *a priori* and thus cannot be specified by the user before the simulation. Therefore, we propose a novel approach relying solely on the Hubbard model parameters that do not explicitly depend on voltage values.

Suppose the Hubbard Hamiltonian (3.13) is diagonalized on a set of  $M$  distinct Fock states:

$$\{|\vec{\nu}_i, \vec{\zeta}_i\rangle\}, \quad i = 1 \dots M. \quad (4.9)$$

Here,  $\vec{\nu}_i$  and  $\vec{\zeta}_i$  are integer-valued row vectors that denote the charge and spin configurations of  $N$  quantum dots, respectively. For example,  $\vec{\nu}_i = (0, 2, 1, 1)$  means that there is no electron in the 1<sup>st</sup> dot, two electrons in the 2<sup>nd</sup> one, and one electron each in the 3<sup>rd</sup> and 4<sup>th</sup> ones. We assign distinct integer values starting from 0 for each individual spin state:  $|0\rangle$  (vacuum state, i.e. no electron in the dot),  $|\uparrow\rangle$ ,  $|\downarrow\rangle$ ,  $|\uparrow\uparrow\rangle$ ,  $|\uparrow\downarrow\rangle$ ,  $\dots$ , and use them as the components for each  $\vec{\zeta}$ . Using this notation,  $\vec{\zeta}_i = (0, 3, 2, 2)$  means that there is no electron in the 1<sup>st</sup> dot, the pair of electrons in the 2<sup>nd</sup> dot has the spin state  $|\uparrow\uparrow\rangle$ , whereas the rest of the dots have one electron each with the spin  $|\downarrow\rangle$ . Such a choice of notation permits the following values for each of  $\vec{\zeta}_i$  components:

$$2^{(\vec{\nu}_i)_k} - 1 \leq (\vec{\zeta}_i)_k < 2^{(\vec{\nu}_i)_{k+1}} - 1, \quad k = 1 \dots N. \quad (4.10)$$

This choice of notation also implies that the set of vectors  $\{\vec{\zeta}_i\}$  spans the entire Fock basis (4.9), and that each  $\vec{\nu}_i$  can be calculated from  $\vec{\zeta}_i$ :

$$\{|\vec{\nu}_i, \vec{\zeta}_i\rangle\} \leftrightarrow \{|\vec{\zeta}_i\rangle\}, \quad (4.11)$$

$$\vec{\nu}_i = \lfloor \log_2 (\vec{\zeta}_i + 1) \rfloor, \quad (4.12)$$

where the floor and logarithm functions are taken element-wise. However, the  $|\vec{\nu}, \vec{\zeta}\rangle$  notation will be used further for better clarity.

In this basis, the Hubbard Hamiltonian eigenfunction that corresponds to the energy

value  $E_k$  will have the form:

$$\begin{aligned} \left| \psi_k(\vec{V}, \vec{W}) \right\rangle &= \sum_{i=1}^M \mathcal{C}_{ki}(\vec{V}, \vec{W}) |\vec{\nu}_i, \vec{\varsigma}_i\rangle : \\ H_{\text{Hub}} \left| \psi_k(\vec{V}, \vec{W}) \right\rangle &= E_k(\vec{V}, \vec{W}) \left| \psi_k(\vec{V}, \vec{W}) \right\rangle, \quad k = 0, \dots, K-1. \end{aligned} \quad (4.13)$$

where  $\mathcal{C}(\vec{V}, \vec{W})$  is the basis transform matrix  $\{|\vec{\nu}, \vec{\varsigma}\rangle\} \rightarrow \{|\psi\rangle\}$  at the gate voltage values  $(\vec{V}, \vec{W})$ , and  $K$  is the number of eigenfunctions we consider. If we define the vector operator  $\hat{\nu}$  that counts the number of electrons in each dot, we can calculate the vector of charges (in the units of  $e$ ) observable in state  $|\psi_k\rangle$ :

$$\vec{q}_k = \langle \psi_k | \hat{\nu} | \psi_k \rangle = \sum_{i,m} \mathcal{C}_{mk}^* \mathcal{C}_{ki} \langle \vec{\nu}_m, \vec{\varsigma}_m | \hat{\nu} | \vec{\nu}_i, \vec{\varsigma}_i \rangle = \sum_{i=0}^{M-1} \vec{\nu}_i |\mathcal{C}_{ik}|^2 \quad (4.14)$$

where the asterisk means complex conjugation. The vector of charges rounded to the nearest integers element-wise defines a charge stability configuration:

$$\vec{Q}_k = \lfloor \vec{q}_k \rfloor \quad (4.15)$$

The total integer charge in the state  $|\psi_k\rangle$  equals the 1-norm of the corresponding charge stability vector:

$$\mathcal{Q}_k = \left\| \vec{Q}_k \right\|_1 = \sum_{i=1}^N \left| \left( \vec{Q}_k \right)_i \right| \equiv \sum_{i=1}^N \left( \vec{Q}_k \right)_i. \quad (4.16)$$

Physically, for each  $(\vec{V}, \vec{W})$ , the charge configuration corresponding to the ground state ( $k=0$ ) is observed. This determines distinct regions of the charge stability diagram.

When we move away from the center of a charge stability region, the energy spacing between the ground and excited states becomes smaller until we reach the border of the region, where  $E_0 = E_1$ . Therefore, the ratios between the ground and excited state energies:

$$\mathcal{K}_{\text{cs}}(k, \vec{V}, \vec{W}) = E_0(\vec{V}, \vec{W}) / E_k(\vec{V}, \vec{W}), \quad k \in \{1, 2, \dots, M-1\}, \quad (4.17)$$

are the physical measures of how well the quantum system is protected from charge transitions at voltage values  $(\vec{V}, \vec{W})$ . Remarkably, the quantities  $\mathcal{K}_{\text{cs}}$  are universal and applicable to any voltage configurations, numbers of electrons in the system, and Fock basis sizes.

Before we define the corresponding cost function, though, we should take into account several important considerations. First of all, the desired charge configuration  $\vec{Q}^{(0)}$  is typically known *a priori* and corresponds to the system ground state within one specific charge stability region. Therefore, to ensure that the minimum of the cost function is always centered at the desired charge stability region, the spectrum should be first rearranged according to  $\vec{Q}^{(0)}$ . Let the index  $k_0$  correspond to the state  $|\psi_k\rangle$  whose charge stability vector (4.15) matches the desired one. Then, formula (4.17) transforms into:

$$\mathcal{K}_{\text{CS}}(k, k_0, \vec{V}, \vec{W}) = \frac{E_{k_0}(\vec{V}, \vec{W})}{E_k(\vec{V}, \vec{W})}, \quad (4.18)$$

$$k_0 : \vec{Q}_{k_0} \equiv \vec{Q}^{(0)}, \quad k \neq k_0, \quad k, k_0 \in \{0, 1, \dots, M-1\}.$$

Secondly, different charge transitions occur with different probabilities. In particular, tunneling between the dots, which does not change the total charge of the system, is much more likely than the attraction of new electrons or removal of the existing ones. To take this into account, we split the values of  $k$  according to the corresponding  $\vec{Q}_k$  and their relations to  $\vec{Q}^{(0)}$ : tunneling is likely only if the vectors  $\vec{Q}_k$  and  $\vec{Q}_{k_0}$  are different by only two adjacent elements, and the total charges are the same:

$$k = \begin{cases} k', & \text{if } [\vec{Q}_k - \vec{Q}_{k_0}] \in \pm\mathcal{C}(-1, 1, 0, 0, \dots, 0) \\ k'', & \text{otherwise.} \end{cases} \quad (4.19)$$

where  $\mathcal{C}$  denotes a set of cyclic permutations. Since the tunneling from  $\vec{Q}_{k_0}$  to  $k''$ -states is forbidden, and the system of quantum dots is well isolated from the charge sources, we can allow the voltages to step into such neighboring regions during the pulse: this will not lead to electron removal or accumulation. We achieve this by effectively increasing the energies of such states by  $\beta \times 100\%$  while leaving the energies of  $k'$ -states unchanged:

$$E'_k = E_{k'}, \quad E''_k = E_{k''}(1 + \beta). \quad (4.20)$$

Since the condition  $E_{k_0} < E''_k$  is now satisfied at a wider range of voltage values, the transformation (4.20) effectively pushes the  $\vec{Q}_{k_0}$  borders with  $\vec{Q}_{k''}$  inside the  $\vec{Q}_{k''}$  regions but does not significantly alter the borders with  $\vec{Q}_{k'}$  ones, see Fig. 4.2. This redefines the values of (4.18) in the following way:

$$K_{\text{CS}}(k', k_0, \vec{V}, \vec{W}) = \frac{E_{k_0}(\vec{V}, \vec{W})}{E'_{k'}(\vec{V}, \vec{W})}, \quad K_{\text{CS}}(k'', k_0, \beta, \vec{V}, \vec{W}) = \frac{E_{k_0}(\vec{V}, \vec{W})}{E''_k(\beta, \vec{V}, \vec{W})}. \quad (4.21)$$

and enables us to finally write the expression for the corresponding cost function:

$$f_{\text{cs}} = \frac{1}{(M-1)T} \int_0^T \left[ \sum_{k'} \Xi_p \left( K_{\text{cs}} \left( k', k_0, \vec{V}(t), \vec{W}(t) \right), \alpha' \right) + \sum_{k''} \Xi_p \left( K_{\text{cs}} \left( k'', k_0, \beta, \vec{V}(t), \vec{W}(t) \right), \alpha'' \right) \right]. \quad (4.22)$$

The prefactor  $\frac{1}{(M-1)T}$  ensures that the cost function always lies within  $[0, 1]$  within the extended charge stability region  $\vec{Q}_{k_0}$ . The integration is necessary for the cost function to incorporate the non-optimality during the whole duration of the pulse. We introduce two distinct cutoff parameters  $\alpha', \alpha''$  to emphasize the difference between the tunneling and non-tunneling charge transition probabilities in the system.

Although  $\alpha'', \beta$  can be chosen only empirically, it is important to establish a link between  $\alpha'(k')$  with the tunnel coupling  $t_{k', k_0}$  between the dots where  $\vec{Q}_{k_0} \rightarrow \vec{Q}_k$  transition is allowed to occur. Clearly, bigger cutoffs are required for bigger couplings in order to preclude tunneling. To achieve this, we use the relation between the quantum-mechanical excess charge (in units of  $e$ ) on the two neighboring dots, their detuning  $\epsilon = E_2 - E_1$ , and tunnel coupling  $t$  [76, 77]:

$$\left\{ \begin{array}{l} \langle n_1 \rangle - N_1 \\ \langle n_2 \rangle - N_2 \end{array} \right\} = \frac{1}{2} \left[ 1 \mp \frac{\epsilon}{\sqrt{\epsilon^2 + 4t^2}} \tanh \left( \frac{\sqrt{\epsilon^2 + 4t^2}}{2k_{\text{B}}T_e} \right) \right], \quad (4.23)$$

where  $T_e$  is the system temperature. The formula is applicable along the line perpendicular to a boundary between the charge stability regions where tunneling is happening. The figure 4.3 shows the experimental charge sensor data fitted with this function. As expected, wider functions correspond to higher values of tunnel coupling.

To quantify the characteristic width of the curve (4.23), we find the zero of the function:

$$F(t, \epsilon) = \frac{\epsilon}{\sqrt{\epsilon^2 + 4t^2}} \tanh \left( \frac{\sqrt{\epsilon^2 + 4t^2}}{2k_{\text{B}}T_e} \right) - \frac{1}{2}$$

around  $\epsilon^{(0)} = 0$  with one iteration of Newton's method:

$$\epsilon_{1/2} = \epsilon^{(0)} - \frac{F(t, \epsilon^{(0)})}{\partial_{\epsilon} F(t, \epsilon^{(0)})} = \frac{t}{2} \coth \frac{t}{k_{\text{B}}T_e} \approx \frac{k_{\text{B}}T_e}{2} + \frac{t}{6k_{\text{B}}T_e}. \quad (4.24)$$

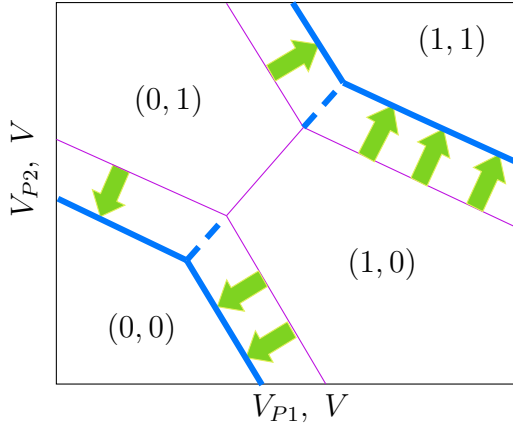


Figure 4.2: Extending the charge stability boundaries to the regions with different total charges, where tunneling is forbidden: case of  $\vec{Q}^{(0)} = (1, 0)$

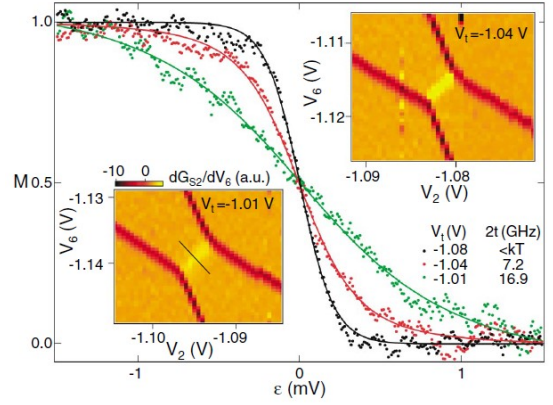


Figure 4.3: Number of electrons in the left dot of a 2-dot system at different values of detuning  $\epsilon$  and tunnel coupling  $t$ . Reproduced from [77]

If we require that the spacing between  $E'_k$  and  $E_{k_0}$  be at least  $\lambda$  times larger than  $\epsilon_{1/2}$  in the optimality region, we obtain the value of the cutoff parameter:

$$\alpha'(k_0, k') = \lambda \frac{\epsilon_{1/2}}{E'_k} = \lambda \frac{t_{k_0, k'} \coth(t_{k_0, k'}/k_B T_e)}{2E'_k(\vec{V}, \vec{W})}, \quad (4.25)$$

This result, combined with formula (4.22), gives the final expression for the cost function associated with the charge stability preservation:

$$f_{cs}(\lambda, \alpha'', \beta) = \frac{1}{(M-1)T} \int_0^T dt \left[ \sum_{k''} \Xi_p \left( K_{cs} \left( k'', k_0, \beta, \vec{V}(t), \vec{W}(t) \right), \alpha'' \right) + \sum_{k'} \Xi_p \left( K_{cs} \left( k', k_0, \vec{V}(t), \vec{W}(t) \right), \lambda \frac{t_{k_0, k'} \coth(t_{k_0, k'}/k_B T_e)}{2E'_k(\vec{V}(t), \vec{W}(t))} \right) \right], \quad (4.26)$$

with the parameters  $\lambda, \alpha'', \beta$  being user-defined.

## 4.2.5 Restriction on absorbed RF electromagnetic energy

The dissipation of the electromagnetic energy from the ESR resonator is yet another mechanism that may lead to non-optimality. We assume that only the magnetic field component is significant in the region where the quantum dots are located. Indeed, the suppression of RF electric field component is essential to avoid photon-assisted tunneling processes. This is achieved in our group with a sophisticated resonator design.

We write the total energy of the ESR magnetic field in the sample, averaged over a single oscillation:

$$\mathcal{W}_{total} = \frac{1}{2\mu_0} \langle B_{RF}^2(t) \cos^2 \omega_{RF} t \rangle_{T_{RF}} \mathcal{V} \approx \frac{B_{RF}^2(t)}{4\mu_0} \mathcal{V}, \quad (4.27)$$

where  $T_{RF} = 2\pi/\omega_{RF}$  is the period of the RF field oscillation, and  $\mathcal{V}$  is the volume of the sample affected by this field. Following the definition of the Q-factor:

$$Q = \omega_{RF} \frac{\mathcal{W}_{total}}{P_{loss}},$$

we find the amount of power lost (i.e. absorbed) at each point of time during the pulse:

$$P_{loss}(t) = \frac{\omega_{RF} \mathcal{V}}{4\mu_0 Q} B_{RF}^2(t). \quad (4.28)$$

The maximal allowed value of this quantity  $P_{max}$  depends on the resonator design and the experimental setting (especially, refrigeration), and thus should be user-defined before the simulation. Alternatively, the maximal values of either the ESR field  $B_{RF,max}$  or the Rabi frequency  $\Omega_{max}$  can be specified. Then, the corresponding dimensionless physical quantity and the cost function read as follows:

$$K_{RF}(t) = \frac{\omega_{RF} \mathcal{V}}{4\mu_0 Q P_{max}} B_{RF}^2(t) = \left( \frac{B_{RF}(t)}{B_{RF,max}} \right)^2 = \left( \frac{\Omega(t)}{\Omega_{max}} \right)^2, \quad (4.29)$$

$$f_{RF} = \frac{1}{T} \int_0^T \Xi_p(K_{RF}(t), \alpha) dt. \quad (4.30)$$



## 4.2.6 Restriction on voltage sweep rates

The upper bound for a time derivative of the voltage on a gate (either plunger or tunnel)  $|\partial_t \mathcal{V}_{max}|$  is necessary to model a realistic voltage pulse generator, whose bandwidth is always limited. This parameter depends on the device and thus should be user-defined as well. This corresponds to the following dimensionless quantities for plunger and tunnel gates, and the cost function:

$$K_{V_i}(t) = \left( \frac{\partial_t V_i(t)}{\partial_t \mathcal{V}_{max}} \right)^2, \quad K_{W_i}(t) = \left( \frac{\partial_t W_i(t)}{\partial_t \mathcal{V}_{max}} \right)^2, \quad (4.31)$$

$$f_{vw} = \frac{1}{(2N-1)T} \int_0^T dt \left( \sum_{i=1}^N \Xi_p(K_{V_i}(t), \alpha) + \sum_{i=1}^{N-1} \Xi_p(K_{W_i}(t), \alpha) \right). \quad (4.32)$$

Here, the prefactor  $\frac{1}{(2N-1)T}$  ensure that  $f_2 \in [0, 1]$  for the allowed values of voltage time derivatives.

## 4.3 Design of effective parameter pulses for primitive quantum gates

### 4.3.1 Choice of the gates to design

As noted before, we model a system of  $N$  electrons with the effective spin Hamiltonian (3.23) in the rotating wave approximation. The Hamiltonian parameters control the electron spin state evolution and can thus realize quantum gate operations. In our architecture [65],  $\sqrt{\text{SWAP}}$  and single-qubit rotations are utilized as the primitive unitary gates. The operator of rotation by an angle  $\theta$  around a unit vector  $\vec{n}$  on a Bloch sphere is given by:

$$\text{ROT}(\vec{n}, \theta) = \exp\left(-i\frac{\theta}{2}\vec{\sigma} \cdot \vec{n}\right), \quad -\pi < \theta \leq \pi. \quad (4.33)$$

whereas the matrix forms of SWAP and  $\sqrt{\text{SWAP}}$  are written as follows:

$$\text{SWAP} = \begin{pmatrix} 1 & 0 & 0 & 0 \\ 0 & 0 & 1 & 0 \\ 0 & 1 & 0 & 0 \\ 0 & 0 & 0 & 1 \end{pmatrix}, \quad \sqrt{\text{SWAP}} = \begin{pmatrix} 1 & 0 & 0 & 0 \\ 0 & \frac{1+i}{2} & \frac{1-i}{2} & 0 \\ 0 & \frac{1-i}{2} & \frac{1+i}{2} & 0 \\ 0 & 0 & 0 & 1 \end{pmatrix}, \quad \left(\sqrt{\text{SWAP}}\right)^2 = \text{SWAP}. \quad (4.34)$$

In a more general case, we can consider SWAP gates, raised to any power  $k$ .

As will be shown below, all gates of type  $(\text{SWAP}_{i,i+1})^k, k \in \mathbb{R}$ , are mediated by the pairwise exchange interactions between the neighboring  $i^{\text{th}}$  and  $i+1^{\text{st}}$  dots. Therefore, each of such gates, particularly  $\sqrt{\text{SWAP}}$ , can be realized locally. Driving certain single-qubit rotations with the global ESR field, though, is a significant challenge inherent to our architecture. More specifically, the problem arises when the rotations should happen locally so that certain qubits remain unaffected during the ESR pulse. The effect of  $g$ -factor deviation is too weak by itself to detune qubits far enough off resonance. On the other hand, slight local control of individual electron  $g$ -factors does not truly detune qubits from resonance but alters the way their states change over time. Therefore, in order to achieve high fidelity of a multi-qubit state, the off-resonant qubits must evolve in a specific way so that they return to the initial state after the pulse while the resonant qubits perform desired rotations. Fortunately, this is possible to achieve if we impose proper constraints of type (4.3) on the pulses. Further in this section, we derive these constraints for each of the single and two-qubit gate we are interested in, both for the qubits that change and the ones that maintain their quantum states upon gate operations.

### 4.3.2 Idling qubits

First, it is important to determine what states qubits should have when no pulse is applied, i.e. in the “idling” regime.

Since the exchange interaction between neighboring electrons is always present, it is beneficial to keep this coupling at idle  $\Delta J$  very small by ensuring high tunnel barriers between the dots. We will estimate how small  $\Delta J$  should be in subsection 4.3.6, where we discuss the evolution of a pair of spins under the exchange part of the Hamiltonian  $\sim J\vec{\sigma}_1 \cdot \vec{\sigma}_2$ .

Ignoring the exchange terms, the Hamiltonian for a chain of qubits can be written as follows:

$$\mathcal{H}_{\text{ESR}} = \sum_{j=1}^N \mathcal{H}_j = \frac{1}{2} \sum_{j=1}^N \left\{ \left[ \left( 1 + \frac{1}{2} \delta g_j(\vec{V}, \vec{W}) \right) \omega - \omega_{\text{RF}} \right] Z_j + \Omega (\cos \phi X_j + \sin \phi Y_j) \right\}, \quad (4.35)$$

Obviously, not supplying any ESR field ( $\Omega = 0$ ) is the only way to ensure that no X or Y rotations take place. When it comes to Z rotations, such parameters as  $\omega \sim B_0$  and  $\omega_{\text{RF}}$  are global, i. e. couple to each of the qubits in the same way. This means that the idling value of deviation  $g$ -factor,  $\delta g_0$ , must be the same for all qubits. In a general case, we need to search for the set of voltage values at idle  $\Delta\vec{V}, \Delta\vec{W}$  that:

- lie deeply in the required charge stability region,
- give an identical value of  $\delta g_j = \delta g_0$  for all  $j = 1 \dots N$ .

For a particular value  $\delta g_0$ , such experimental parameters as the Zeeman field  $B_0 \sim \omega$  and the ESR frequency should be chosen to satisfy the following condition:

$$\frac{\delta g_{0,j}(\vec{V}, \vec{W})}{2} \omega = \omega_{\text{RF}} - \omega \quad \text{for all } j. \quad (4.36)$$

This condition ensures that all the coefficients in front of  $Z_j$  are set to zero, which corresponds to the absence of Z rotations.

For now, we assume that the value of  $\delta g_0$  is chosen *a priori* and is a constant of the spin system. The explicit search problem over the set of voltages  $\{\vec{V}, \vec{W}\}$  will be formulated

in section 4.5. Using the new notation, each of the single-qubit parts of the Hamiltonian can be written in a simplified form:

$$\mathcal{H}_j = \frac{1}{2} \left[ \frac{\delta g_j - \delta g_0}{2} \omega Z_j + \Omega (\cos \phi X_j + \sin \phi Y_j) \right]. \quad (4.37)$$

In the following subsections where we derive the effective pulses for single-qubit rotations, we will denote each resonant qubit with the index “+”, and each off-resonant qubit with the index “-”.

### 4.3.3 Z rotations

The manipulation of electron deviation  $g$ -factors gives a way to directly address individual qubits during rotations around  $\hat{z}$  axis on the Bloch sphere. Indeed, not supplying any ESR field ( $\Omega = 0$ ) ensures that the rotation axes of all qubits are set to  $\hat{z}$ , and the rotational speed of each of them is controlled by  $\delta g_j(t)$ . The dependency of  $\delta g_j$  on time  $t$  is implicit through its dependence on time-varying gate voltages  $\vec{V}(t), \vec{W}(t)$ .

For the non-resonant qubits, the obvious choice of deviation  $g$ -factor is  $\delta g_-(t) \equiv \delta g_0$  at all times. This ensures  $\mathcal{H}_- \equiv 0$  and no state change, since all qubits can be considered decoupled in this case. For each resonant qubit, the evolution operator is given by:

$$U_+ = \exp \left( -i \int_0^T \mathcal{H}_+(t) dt \right) = \exp \left( -\frac{i}{2} Z \cdot \omega T \int_0^1 \frac{\delta g_+(\tau) - \delta g_0}{2} d\tau \right), \quad (4.38)$$

where  $T$  is the pulse length, and  $\tau = t/T$  is the normalized time. By comparing formula (4.38) with (4.33), we obtain the requirement for the pulse length  $T$  to rotate the spin by the angle  $\theta$ :

$$\text{ROTZ}(\theta_j) : \quad \omega T \int_0^1 \frac{\delta g_{+,j}(\tau) - \delta g_0}{2} d\tau = \theta_j. \quad (4.39)$$

The index  $j$  reflects the fact that the qubits are completely decoupled from each other; therefore, Z rotations by any angles  $\theta_j$  can occur in parallel. Therefore, the duration of each such pulse is given by the following:

$$T(\hat{z}, \alpha) = \frac{4\pi\alpha}{\omega \left| \int_0^1 (\delta g_+(\tau) - \delta g_0) d\tau \right|}, \quad \text{where } \alpha = \frac{|\theta|}{2\pi}. \quad (4.40)$$

Importantly, there are no constraints on the *shapes* of  $\delta g_{+,j}(\tau)$  pulses, only the areas under their curves (integral in expression (4.39)).

### 4.3.4 X and Y rotations

Unlike in the previous case, the states of both resonant and non-resonant qubits necessarily evolve during an X or Y rotation due to the global nature of ESR field. Thus, the parameters for each of non-resonant qubits should be engineered so that their evolution operators become unity at  $t = T$ . Luckily, there exists a universal approach that achieves this irrespective of the initial states of the non-resonant qubits.

#### Resonant qubits

The rotation axis for resonant qubits should be fixed:  $\hat{x}$  for ROTX( $\theta$ ), and  $\hat{y}$  for ROTY( $\theta$ ). Therefore, their  $g$ -factors should be set to the idling values at all times:

$$\delta g_+(t) \equiv \delta g_0, \quad t \in [0, T].$$

Let us denote  $\vec{n}_0 = (1, 0, 0)^T$  for an X rotation, and  $\vec{n}_0 = (0, 1, 0)^T$  for a Y rotation. The value of ESR phase  $\phi$  should be kept constant, since it defines the axis and direction (clockwise/counterclockwise) of spin rotation. From the Hamiltonian (4.35), we determine the required values of  $\phi$  for each type of pulse:

Sign of $\theta$	+	-
ROTX	0	$\pi$
ROTY	$\pi/2$	$-\pi/2$

Table 4.1: Values of ESR phases  $\phi$  to be supplied during spin rotations around  $\hat{x}$  and  $\hat{y}$  axes.

This allows us to write the Hamiltonian for a resonant qubit for the case of either X or Y rotation as:

$$\mathcal{H}_+ = \frac{\Omega}{2} \text{sign}(\theta) \vec{\sigma} \cdot \vec{n}_0.$$

The corresponding evolution operator is:

$$U_+ = \exp\left(-i \int_0^T \mathcal{H}_+(t) dt\right) = \exp\left(-\frac{i}{2} \vec{\sigma} \cdot \vec{n}_0 T \text{sign}(\theta) \int_0^1 \Omega(\tau) d\tau\right), \quad (4.41)$$

which gives us the condition for  $T$ :

$$\text{ROTX}(\theta), \text{ROTY}(\theta) : \quad T \int_0^1 \Omega(\tau) d\tau = |\theta|. \quad (4.42)$$

This condition, along with the choice of constant phase from Table 4.1, indicates that all resonant qubits will necessarily rotate synchronously by the same angle  $\theta$  during X or Y rotations, which is due to the global nature of ESR field.

### Nonresonant qubits

In the general case, the Hamiltonian for each nonresonant qubit consists of two time-dependent parts, even when  $\phi$  is kept constant:

$$\mathcal{H}_{-,j}(t) = \frac{1}{2} \left[ \frac{\delta g_{-,j}(t) - \delta g_0}{2} \omega Z_j + \Omega(t) \vec{\sigma}_j \cdot \begin{pmatrix} \cos \phi \\ \sin \phi \\ 0 \end{pmatrix} \right]. \quad (4.43)$$

Because of this,  $[\mathcal{H}_-(t'), \mathcal{H}_-(t'')] \neq 0$  for  $t' \neq t''$ . Therefore, there is no simple way to express the spin evolution in the general case, since it is a combination of rotations around a time-varying axis. Nevertheless, we can make the rotation deterministic if we impose a constraint that  $\Omega(t)$  and all  $\delta g_-(t)$  pulses have the same shape:

$$\forall t: \quad \Omega(t) = A \cdot \omega \frac{|\delta g_-(t) - \delta g_0|}{2}, \quad A = \text{const} > 0. \quad (4.44)$$

Here, we assume (for now) that each  $g$ -factor pulse maintains its sign throughout the pulse:

$$s_j = \text{sign} [\delta g_{-,j}(t) - \delta g_0] = \text{const}.$$

This transforms the Hamiltonian expression into:

$$\begin{aligned} \mathcal{H}_{-,j}(t) &= \frac{1}{2} \frac{|\delta g_-(t) - \delta g_0|}{2} \omega \left[ s_j Z_j + A \vec{\sigma}_j \cdot \begin{pmatrix} \cos \phi \\ \sin \phi \\ 0 \end{pmatrix} \right] = \\ &= \frac{1}{2} \frac{|\delta g_-(t) - \delta g_0|}{2} \omega \sqrt{1 + A^2} \vec{\sigma} \cdot \vec{n}'_j, \quad \vec{n}'_j = \frac{1}{\sqrt{1 + A^2}} \begin{pmatrix} A \cos \phi \\ A \sin \phi \\ s_j \end{pmatrix}. \end{aligned} \quad (4.45)$$

Clearly, now the rotation axes  $\vec{n}'_j$  remains fixed, and we can write the evolution operator:

$$U_{-,j} = \exp \left( -i \int_0^T \mathcal{H}_{-,j}(t) dt \right) = \exp \left( -\frac{i}{2} \vec{\sigma}_j \cdot \vec{n}'_j \omega T \sqrt{1 + A^2} \int_0^1 \frac{|\delta g_-(t) - \delta g_0|}{2} d\tau \right). \quad (4.46)$$

Remarkably, if we require that each nonresonant spin makes an integer number of complete turns during the pulse, it will always return to its initial state irrespective of the rotation axis direction  $\vec{n}'_j$  or the sign  $s_j$ ! By comparing formulas (4.33) and (4.46), we obtain the following condition:

$$\begin{array}{l} \text{ROTX}(\theta) \\ \text{ROTY}(\theta) \end{array} : \quad |\theta_-| = \omega T \sqrt{1 + A^2} \int_0^1 \frac{|\delta g_-(t) - \delta g_0|}{2} d\tau = 2\pi\nu, \quad \nu = 1, 2, 3, \dots \quad (4.47)$$

As it is always preferable to reduce the pulse duration as much as possible, we will always choose  $\nu = 1$ , which corresponds to one complete turn. From formula (4.44) it also follows that in this case, the ESR field  $\Omega(\tau) \sim |\delta g_-(\tau) - \delta g_0|$  will be smallest possible, which is also desirable.

### Combining results

Combining formulas (4.44), (4.47) and (4.42), we obtain the set of conditions that must be satisfied simultaneously during the pulse:

$$\text{ROTX}(\theta), \text{ROTY}(\theta) : \quad \begin{cases} \omega T A \int_0^1 \frac{|\delta g_-(t) - \delta g_0|}{2} d\tau = |\theta|, \\ \omega T \sqrt{1 + A^2} \int_0^1 \frac{|\delta g_-(t) - \delta g_0|}{2} d\tau = 2\pi, \end{cases} \quad (4.48)$$

Dividing the equations one by the other gives us the constraint on the value of  $A$ :

$$\frac{A}{\sqrt{1 + A^2}} = \frac{|\theta|}{2\pi} \implies A = \frac{1}{\sqrt{\left(\frac{2\pi}{\theta}\right)^2 - 1}}. \quad (4.49)$$

This gives us the pulse duration that corresponds to an  $X$  or  $Y$  rotation:

$$T(\hat{x}, \alpha) = T(\hat{y}, \alpha) = \frac{4\pi}{\omega \int_0^1 |\delta g_-(\tau) - \delta g_0| d\tau} \sqrt{1 - \alpha^2}, \quad (4.50)$$

and the expression for the RF magnetic field pulse:

$$\Omega(t) = \frac{\omega}{2} |\delta g_-(t) - \delta g_0| \cdot \frac{\alpha}{\sqrt{1 - \alpha^2}}, \quad (4.51)$$

in terms of  $\alpha = |\theta|/2\pi$ .

### 4.3.5 Arbitrary rotations

Using the same principles as for X and Y rotations, it is straightforward to engineer effective pulses for arbitrary rotations  $\text{ROT}(\vec{n}_0, \theta)$ .

As before, we impose a constraint that the deviation  $g$ -factor and magnetic field pulses have the same shape:

$$\frac{\omega}{2} s_{\pm} (\delta g_{\pm}(t) - \delta g_0) = A_{\pm} \frac{S(t)}{T}, \quad \Omega = \beta \frac{S(t)}{T}. \quad (4.52)$$

Here,  $A_+$ ,  $A_-$  and  $\beta$  are some nonnegative constant factors, whereas  $S(t) \geq 0$  is a dimensionless continuous shape function with the average value being equal to 1:

$$\langle S(t) \rangle = \frac{1}{T} \int_0^T S(t) dt = \int_0^1 S(\tau) d\tau = 1. \quad (4.53)$$

We additionally require  $S(t) \equiv 0$  before and after the pulse: this ensures return of qubits to their idling states. It is important to note that formulas (4.52) easily generalize to the case of functions  $S(t)$  being of variable sign. For this, the only correction that needs to be applied is ensuring that the magnitude of ESR field always remains positive. This means that whenever  $S(t)$  acquires negative values, they should be reinterpreted as a phase shift by  $\pi$  with  $\Omega(t) \sim |S(t)|$ . For simplicity, we will derive the results for  $S(t) \geq 0$  and then generalize them.

From the chosen normalization of the shape function, we can immediately determine the properties of its maximal value  $S_{max}$ :

1. From  $\langle S \rangle = 1$  and  $S(0) = S(T) = 0$ , it immediately follows that  $S_{max} \geq 1$  when  $S(t) \geq 0$ .
2.  $S_{max}$  is of the order of unity for the typical simplistic pulse shapes. For example, a square pulse has  $S_{max} = 1$ , any triangular pulse has  $S_{max} = 2$ , and a Gaussian pulse with half-width  $\sigma$  has  $S_{max} \approx \frac{1}{2\pi\sqrt{\sigma}}$  (the equality holds at  $T \rightarrow \infty$ ).

The Hamiltonian for a single qubit now reads:

$$\mathcal{H}_{\pm,j} = \frac{1}{2} \frac{S(t)}{T} \left[ s_{\pm,j} A_{\pm} Z_j + \beta (\cos \phi X_j + \sin \phi Y_j) \right] = \frac{1}{2} \frac{S(t)}{T} \sqrt{A_{\pm}^2 + \beta^2} \vec{\sigma}_j \cdot \vec{n}_{\pm,j}, \quad (4.54)$$

$$\vec{n}_{\pm,j} = \left( \frac{\beta}{\sqrt{A_{\pm}^2 + \beta^2}} \cos \phi, \frac{\beta}{\sqrt{A_{\pm}^2 + \beta^2}} \sin \phi, \frac{A_{\pm} s_j}{\sqrt{A_{\pm}^2 + \beta^2}} \right)^T. \quad (4.55)$$



Our goal is to ensure that the resonant spins rotate around the axis  $\vec{n}_0 \text{sign}(\theta_0)$  by the angle  $|\theta_0|$ . From the parametrization of  $\vec{n}_0$  in spherical coordinates:

$$\vec{n}_0 = (n_{0x}, n_{0y}, n_{0z})^T = (\sin \chi_0 \cos \psi_0, \sin \chi_0 \sin \psi_0, \cos \chi_0)^T, \quad (4.56)$$

we immediately obtain the following condition for phase and the resonant qubit parameters:

$$\phi = \psi_0 = \text{atan2}(n_{0y}, n_{0x}), \quad (4.57)$$

$$\frac{A_+ s_{+,j}}{\sqrt{A_+^2 + \beta^2}} = \cos \chi_0 \text{sign}(\theta_0) = n_z \text{sign}(\theta_0). \quad (4.58)$$

Since  $A_{\pm} \geq 0$ , this formula immediately gives us the requirement on the sign of  $g$ -factor pulse for all resonant qubits:

$$s_{+,j} = \text{sign}(n_z) \text{sign}(\theta_0) \quad \text{for all } j. \quad (4.59)$$

We determine the angles of rotation from the evolution operator:

$$U_{\pm,j} = \exp\left(-i \int_0^T \mathcal{H}_{\pm,j}(t) dt\right) = \exp\left(-\frac{i}{2} \underbrace{\int_0^1 S(\tau) d\tau}_{=1} \sqrt{A_{\pm}^2 + \beta^2} \vec{\sigma}_j \cdot \vec{n}_{\pm,j}\right). \quad (4.60)$$

Therefore, the angles of rotation for the resonant ( $\theta_0$ ) and nonresonant ( $2\pi$ ) qubits are connected with the corresponding constants in the following way:

$$\sqrt{A_+^2 + \beta^2} = |\theta_0|, \quad \sqrt{A_-^2 + \beta^2} = 2\pi. \quad (4.61)$$

By combining formulas (4.58) and (4.61), we obtain the following expressions for the constants  $A_+$ ,  $A_-$ ,  $\beta$ :

$$A_+ = |n_{z0} \theta_0|, \quad A_- = \sqrt{(2\pi)^2 - \theta_0^2 (n_{x0}^2 + n_{y0}^2)}, \quad \beta = |\theta_0| \sqrt{n_{x0}^2 + n_{y0}^2}. \quad (4.62)$$

As in the case of X and Y rotations, the expressions hold at any signs of  $g$ -factor pulses on nonresonant qubits  $s_{-,j}$ .

By substituting (4.62) into formula (4.52), recalling (4.57) and (4.59), and generalizing to the case of  $S(t)$  having any sign, we obtain the expressions for effective pulses that

realize  $\text{ROT}(\vec{n}, \theta)$  gate (“0” indices are dropped for conciseness):

$$\text{ROT}(\vec{n}, \theta) : \begin{pmatrix} \delta g_+(t) - \delta g_0 \\ \delta g_-(t) - \delta g_0 \\ \Omega(t) \end{pmatrix} = \frac{S(t)}{T} \begin{pmatrix} \frac{2n_z\theta}{\omega} \\ \pm \frac{2}{\omega} \sqrt{(2\pi)^2 - \theta^2 (n_x^2 + n_y^2)} \\ |\theta| \sqrt{n_x^2 + n_y^2} \text{sign } S(t) \end{pmatrix} \quad (4.63)$$

$$\phi(t) = \text{atan2}(n_y \text{sign } S(t), n_x \text{sign } S(t))$$

These final expressions summarize the constraints sufficient for the arbitrary spin rotation engineering with 100% theoretical fidelity:

1. same shape function  $S(t)$  for deviation  $g$ -factors and ESR field magnitude,
2. piecewise constant ESR phase (more precisely, constant within all time intervals where  $S(t)$  maintains its sign).

By taking an average of the left and right hand sides of the matrix identity in (4.63), we obtain the formula for pulse duration from the  $g$ -factor values:

$$T(\vec{n}, \alpha) = \frac{4\pi}{\omega} \times \begin{cases} \frac{\alpha |n_z|}{\left| \int_0^1 (\delta g_+(\tau) - \delta g_0) d\tau \right|}, & n_z \neq 0, \\ \frac{\sqrt{1 - \alpha^2(n_x^2 + n_y^2)}}{\left| \int_0^1 (\delta g_-(\tau) - \delta g_0) d\tau \right|}, & n_z \neq 1, \end{cases} \quad \alpha = \frac{|\theta|}{2\pi}. \quad (4.64)$$

(note that the two expressions give the same result in case  $0 < |n_z| < 1$ ). One can easily verify that the special cases of  $n_z = 1$  (Z rotation),  $n_x = 1$  and  $n_y = 1$  (X and Y rotations) correspond to the formulas (4.40) and (4.50).

### 4.3.6 SWAP<sup>k</sup> pulses

Now we discuss the case when no single-qubit rotations occur, which corresponds to the values

$$\delta g_j \equiv \delta g_0 \text{ for all } j \in \{1, \dots, N\}.$$

In this case, the spin chain is described by the Heisenberg Hamiltonian (normalized by  $\hbar$ ):

$$\mathcal{H}_{ex}(t) = \sum_{j=1}^{N-1} \mathcal{H}_{j,j+1}(t) = \sum_{j=1}^{N-1} \frac{J_j(t)}{4\hbar} \vec{\sigma}_j \cdot \vec{\sigma}_{j+1}, \quad (4.65)$$

where  $J_j(t)$  is the exchange coupling of the  $j^{\text{th}}$  pair of qubits in a chain (i.e. between the  $j^{\text{th}}$  and  $j + 1^{\text{st}}$  qubits). Their time dependency is inherited from the dependencies  $\vec{V}(t), \vec{W}(t)$ , by analogy to the case of deviation  $g$ -factors discussed earlier. It is evident from formula (4.65) that all electrons are in principle always coupled to each other. However, we can approximately treat the  $j^{\text{th}}$  and  $j + 1^{\text{st}}$  electrons as an isolated system provided that the exchange couplings to the other qubits, namely  $j - 1^{\text{st}}$  and  $j + 2^{\text{nd}}$ , are very small:

$$J_{j-1}, J_{j+1} \ll J_j.$$

By analogy to the previous discussions, we will denote the pairs of qubits that evolve under exchange (“resonant”) with the index “+”, and the pairs whose couplings are negligible (“nonresonant”) with the index “-”.

Knowing that the swap operator for the  $j^{\text{th}}$  and  $j + 1^{\text{st}}$  qubits  $\text{SWAP}_{j,j+1}$  is given by the formula:

$$\text{SWAP}_{j,j+1} = \frac{1}{2} (I_j I_{j+1} + X_j X_{j+1} + Y_j Y_{j+1} + Z_j Z_{j+1}), \quad \text{SWAP}_{j,j+1}^2 = I_j I_{j+1},$$

we can write the time evolution operator for the corresponding 2-qubit system:

$$\begin{aligned} U_{j,j+1} &= \exp \left( -i \int_0^T \mathcal{H}_{j,j+1}(t) dt \right) = \exp \left[ -iT \int_0^1 \left( \text{SWAP}_{j,j+1} - \frac{1}{2} I_j I_{j+1} \right) \frac{J_j(\tau)}{2\hbar} d\tau \right] = \\ &= \exp \left( \frac{i\Phi_j}{2} \right) \exp [-i\Phi_j \text{SWAP}_{j,j+1}] = \exp \left( \frac{i\Phi_j}{2} \right) [I_1 I_2 \cos \Phi - i \text{SWAP}_{j,j+1} \sin \Phi], \\ &\text{where } \Phi_j = \frac{T}{2\hbar} \int_0^1 J_j(\tau) d\tau. \quad (4.66) \end{aligned}$$

From this expression we conclude that when  $\Phi_j = \frac{\pi}{2}$ , a SWAP gate (up to an unimportant global phase factor  $e^{\frac{i\pi}{4}}$ ) is realized. From the exponential character of  $U_j$  we deduce that the operator of a general form  $\text{SWAP}^k$  is realized when  $\Phi_j(k) = \frac{\pi}{2}k$ . This gives us the conditions on the parameters for “resonant” and “nonresonant” pairs:

$$\text{SWAP}^k : \quad \int_0^1 J_+(\tau) d\tau = k \frac{\pi\hbar}{T}, \quad J_- = \Delta J \ll \int_0^1 J_+(\tau) d\tau, \quad (4.67)$$

where  $\Delta J$  is the exchange offset value for idling qubits. Therefore, the duration of such pulse reads as:

$$T(\text{SWAP}^k) = \frac{k\pi\hbar}{\int_0^1 J_+(\tau)d\tau} \quad (4.68)$$

The formula (4.68) gives us a way to estimate the order of magnitude of  $\Delta J$  to choose. If  $T_{err}$  is the period of time between two consecutive error correction cycles, then we must ensure that the SWAP of idling qubits occurs on a much longer timescale:

$$T_{err} \ll \frac{\pi\hbar}{\Delta J} \quad \Rightarrow \quad \Delta J \ll \frac{\pi\hbar}{T_{err}}. \quad (4.69)$$

We can also rewrite the exchange pulse using a dimensionless shape function with the unit average (cf. subsec. 4.3.5):

$$J_+(t) = C_k \hbar \frac{S(t)}{T}, \quad S(t) \geq 0, \quad \langle S(t) \rangle = 1, \quad (4.70)$$

Strictly speaking, setting  $J(0) = J(T) = 0$  is impossible since the exchange interaction is always present. Therefore, if we require that  $S(0) = S(T) \equiv 0$  as in subsec. 4.3.5, we should rewrite the formula above according to:

$$J_+(t) = \Delta J(1 - S(t)) + C_k \hbar \frac{S(t)}{T} \quad (4.71)$$

to meet the conditions at time interval boundaries. However, in all realistic scenarios we want to ensure that the period of exchange oscillations on idling qubits  $2\pi\hbar/\Delta J$  is extremely small compared to the period  $T$  of any quantum gate (cf. equation (4.67)). Thus, we expect that still using the expression in the form (4.70) will give only a negligible numerical error. In either case, by substituting (4.70) or (4.71) to (4.67), we obtain the value of constant  $C_k$  that corresponds to a  $\text{SWAP}^k$  pulse:

$$\text{SWAP}^k : \quad C_k = \pi k. \quad (4.72)$$

All the considerations above apply to a quasi-isolated subsystem of  $j^{\text{th}}$  and  $j + 1^{\text{st}}$  qubits. Therefore, any number of exchange-driven pulses of different shapes can run in parallel as long as each qubit is affected by only one gate at a time (i.e. no simultaneous gates on adjacent pairs). With this, we can write a general expression for all pairs:

$$\begin{aligned} (\text{SWAP}_j)^k : \quad J_j(t) &= \Delta J(1 - S_j(t)) + \pi k \hbar \frac{S_j(t)}{T}, \\ j &\in \{m, n : |m - n| \geq 2\} \subset \{1, \dots, N\}. \end{aligned} \quad (4.73)$$

## 4.4 Preliminary quantum circuit optimization

### 4.4.1 Rotation angle shift by $2\pi$

In order to get an idea of how the primitive quantum gates designed in previous section can be optimized for faster operation, it is instructive to compare the durations of the pulses that realize them. Suppose we want to perform a Z rotation by an angle  $\theta$  of one qubit and an X (or Y) rotation by the same angle of the other one by supplying the same  $g$ -factor pulses. Physically, in the simplest case of completely decoupled and isolated qubits, this corresponds to identical voltage sequences. By comparing the durations of the corresponding pulses from formulas (4.40) and (4.50):

$$\frac{T(\hat{z}, \alpha)}{T(\hat{x}, \alpha)} = \frac{T(\hat{z}, \alpha)}{T(\hat{y}, \alpha)} = \frac{\alpha}{\sqrt{1 - \alpha^2}}, \quad \alpha = \frac{|\theta|}{2\pi}. \quad (4.74)$$

we conclude that Z gates are shorter than their X or Y counterparts for typical rotation angles  $|\theta| \leq \pi$ , or  $\alpha < \frac{1}{2}$ . Therefore, it is relevant to discuss whether it is possible to shorten the duration of X or Y gates by some simple considerations.

Since  $T(\hat{z}, \alpha) \sim \alpha$ , it is obviously always better to choose smaller  $|\theta|$  for driving Z rotations. On the other hand, from the relations for X (or Y) rotations from (4.50) and (4.51):

$$T(\hat{x}, \alpha) \sim \sqrt{1 - \alpha^2}, \quad \Omega \sim \frac{\alpha}{\sqrt{1 - \alpha^2}}, \quad (4.75)$$

we conclude that X (or Y) rotations run faster when  $\alpha$  is closer to 1, or the angle of rotation is closer to  $\pm 2\pi$ . This counterintuitive result stems from the fact that during these gate operations, spins of nonresonant electrons revolve in parallel until they make one complete turn. Thus, loosely speaking, resonant and nonresonant qubits rotate in better registry with each other when  $\alpha$  is close to 1, which leads to smaller pulse durations required.

Since the rotations by the angles  $\theta$  and  $\theta \pm 2\pi$  always lead to physically equivalent results, a simple replacement:

$$\theta \mapsto \theta - 2\pi \operatorname{sign} \theta, \quad \Rightarrow \quad \alpha \mapsto (1 - \alpha), \quad (4.76)$$

automatically shortens the pulse duration for smaller angles without changing the physical picture of quantum evolution. However, it comes at a cost of supplying stronger ESR field, and therefore, higher energy absorption. Table 4.2 summarizes all these results and shows that the cost of replacement (4.76) is quite high for a relatively small speed-up  $\sim \alpha^{-1/2}$ .

For example, for  $\theta = \frac{\pi}{2}$  ( $\alpha = \frac{1}{4}$ ), we get an  $\sqrt{2} \cdot \frac{17}{16} \approx 1.5$  times speed-up at a price of supplying a  $4\sqrt{2} \cdot \frac{13}{16} \approx 4.6$  times stronger magnetic field, which will increase the RF energy absorption by a factor of  $16\sqrt{2} \cdot \frac{9}{16} \approx 12.7$ . Such algorithm may be experimentally feasible nonetheless, since the Rabi frequency values needed for an  $X$  or  $Y$  pulse from (4.52) are coupled to very small values of  $g$ -factor shifts:

$$\Omega \sim \omega \times 10^{-4}.$$

Quantity	Symbol	Formula	Asymptotic expansion ( $\alpha \rightarrow 0$ )
Decrease in pulse duration	$\eta_T$	$\sqrt{\frac{1-\alpha^2}{1-(1-\alpha)^2}}$	$\frac{1}{\sqrt{2\alpha}} \left(1 + \frac{\alpha}{4} + o(\alpha)\right)$
Increase in ESR field amplitude	$\eta_\Omega$	$\frac{1-\alpha}{\alpha} \sqrt{\frac{1-\alpha^2}{1-(1-\alpha)^2}}$	$\frac{1}{\sqrt{2\alpha^{3/2}}} \left(1 - \frac{3\alpha}{4} + o(\alpha)\right)$
Increase in ESR power losses	$\eta_P = \eta_\Omega^2$	$\left(\frac{1-\alpha}{\alpha}\right)^2 \frac{1-\alpha^2}{1-(1-\alpha)^2}$	$\frac{1}{2\alpha^3} \left(1 - \frac{3\alpha}{2} + o(\alpha)\right)$
Increase in energy absorbed during the pulse	$\eta_E = \frac{\eta_\Omega^2}{\eta_T}$	$\left(\frac{1-\alpha}{\alpha}\right)^2 \sqrt{\frac{1-\alpha^2}{1-(1-\alpha)^2}}$	$\frac{1}{\sqrt{2\alpha^{5/2}}} \left(1 - \frac{7\alpha}{4} + o(\alpha)\right)$

Table 4.2: Relative changes in pulse parameters upon the shift of angle of rotation by  $2\pi$ .

## 4.4.2 Hybrid gates

Consider the Hamiltonian (3.23) for a system of 2 qubits, written in a general form:

$$\mathcal{H}_{12} = a_1(t)\vec{\sigma}_1 \cdot \vec{n}_1(t) + a_2(t)\vec{\sigma}_2 \cdot \vec{n}_2(t) + c(t)\vec{\sigma}_1 \cdot \vec{\sigma}_2. \quad (4.77)$$

Let us derive the parameters which decouple the exchange interaction from spin rotations. For this, we find the commutator between the single-qubit and two-qubit parts of the Hamiltonian (Einstein's summation convention is used throughout):

$$\begin{aligned} [c(t)\vec{\sigma}_1 \cdot \vec{\sigma}_2, a_1(t)\vec{\sigma}_1 \cdot \vec{n}_1(t) + a_2(t)\vec{\sigma}_2 \cdot \vec{n}_2(t)] &= c [\sigma_{1l}\sigma_{2l}, a_1n_{1j}\sigma_{1j} + a_2n_{2j}\sigma_{2j}] = \\ &= c(2i\varepsilon_{ljk}\sigma_{1k}\sigma_{2l}a_1n_{1j} + 2i\varepsilon_{ljk}\sigma_{1l}\sigma_{2k}a_2n_{2j}) = 2ic\varepsilon_{ljk}\sigma_{1l}\sigma_{2k}(n_{2j}a_2 - n_{1j}a_1) \\ &= 2ic(t) [\vec{\sigma}_1 \times \vec{\sigma}_2] \cdot (a_1(t)\vec{n}_1(t) - a_2(t)\vec{n}_2(t)). \end{aligned} \quad (4.78)$$

Therefore, the necessary condition for the parts of the Hamiltonian to commute is

$$a_1(t) = a_2(t), \quad \vec{n}_1(t) = \vec{n}_2(t), \quad (4.79)$$

(the evolution with  $a_1 = -a_2$ ,  $\vec{n}_1 = -\vec{n}_2$ , which is yet another solution, is physically the same). Within our approach (sec. 4.3), this means that when identical  $\text{ROT}(\vec{n}, \theta)$  pulses of the same shape are applied on both qubits, a  $\text{SWAP}^k$  gate can be applied simultaneously! In other words, our architecture allows for hybrid  $\text{ROT} - \text{SWAP}$  gates to be realized directly (fig. 4.4).

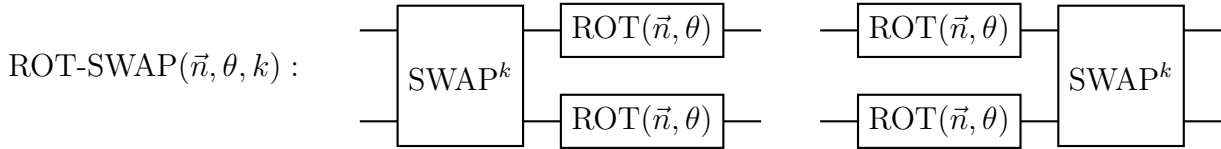


Figure 4.4: Equivalent circuits for a hybrid  $\text{ROT-SWAP}$  gate natively realizable within our spin quantum computer architecture [65]. Here and throughout, circuit diagrams are drawn using the `quantikz` package in  $\text{\LaTeX}$  [83].

Remarkably, the shape of the  $\text{SWAP}^k$  pulse  $\sim c(t)$  can be different from the shape of  $\text{ROT}(\vec{n}, \theta)$  pulses  $\sim a_1(t)$ . The expressions for time-dependent  $g$ -factor, Rabi frequency and exchange coupling from (4.63), (4.73) are applicable to the hybrid gates as well.

### 4.4.3 Parallel execution of gates

As discussed earlier, in section 4.3,  $Z$  rotations and  $\text{SWAP}^k$  gates are realized by manipulating local spin effective parameters (deviation  $g$ -factors and exchange couplings, respectively). Therefore, such gates with any parameters ( $\theta$ ,  $k$ , or the shape) can be applied in parallel provided that they act on distinct qubits. It was also shown in the previous subsection that when the pulses that realize a  $Z$  rotation on a pair of qubits are identical, any  $\text{SWAP}^k$  gate can act on them simultaneously.

When it comes to arbitrary spin rotations different from a  $Z$  rotation, a nonzero global ESR field is necessary. This imposes serious restrictions on which rotations can be run in parallel. Indeed, assume we want to implement two distinct pulses  $\text{ROT}(\vec{n}_1, \theta_1)$  and  $\text{ROT}(\vec{n}_2, \theta_2)$  on two different qubits in parallel. Then, the ESR pulse  $\beta \frac{|S(t)|}{T}$ , where the constant  $\beta$  is determined by equation (4.62), is necessarily the same for both rotations:

$$\beta = |\theta_1| \sqrt{n_{x,1}^2 + n_{y,1}^2} = |\theta_2| \sqrt{n_{x,2}^2 + n_{y,2}^2}. \quad (4.80)$$

Evidently, this expression restricts the axis and the total angle of rotation for each  $\text{ROT}(\vec{n}, \theta)$  pulse run in parallel. Therefore, in practice, one will always combine only synchronous and

identical  $\text{ROT}(\vec{n}, \theta)$  pulses, and  $2\pi$  rotations on nonresonant qubits. The exchange  $\text{SWAP}^k$  gate can be combined with a pair of either resonant or nonresonant qubits, since the pairs of both kinds evolve synchronously (cf. subsec. 4.4.2). In the latter case, it is equivalent to applying a “pure”  $\text{SWAP}^k$  gate as if no other evolution takes place. Since all exchange operations act locally, their pulse shapes are not restricted.

Tables 4.3 and 4.4 present a summary of the two groups of gates that can be applied in parallel: voltage-only driven, and voltage and ESR driven. The relevant dimensionless constants  $A', B, C$ , where  $A'$  is the only signed one, that relate the pulses to their shape functions (possibly distinct) are deduced from formulas (4.62) and (4.72), combined in one expression below:

$$\begin{aligned} \omega\left(\delta g_{\pm,j}(t) - \delta g_0\right) &= A'_{\pm,j} \frac{S_{g,j}(t)}{T}, & \Omega(t) &= \mathfrak{B} \frac{|S_{\Omega}(t)|}{T}, \\ \frac{J_{\pm,j}(t)}{\hbar} &= \frac{\Delta J}{\hbar} [1 - r_j S_{J,j}(t)] + C_j \frac{S_{J,j}(t)}{T}. \end{aligned} \quad (4.81)$$

A variable  $r$  indicates whether the  $j^{\text{th}}$  pair of qubits participates in an exchange gate or not:

$$r_j = \Theta(C_j - 0) = \begin{cases} 1, & j^{\text{th}} \text{ pair is resonant,} \\ 0, & j^{\text{th}} \text{ pair is nonresonant.} \end{cases} \quad (4.82)$$

This notations allows us to interpret the nonresonant case as an application of a  $\text{SWAP}^0$  gate so that  $C_- \equiv 0$ . As before, when the qubit index “ $j$ ” is dropped, the constant is the same for all qubits of a specified kind (“+” for resonant, and “−” for nonresonant).



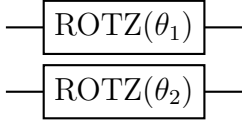
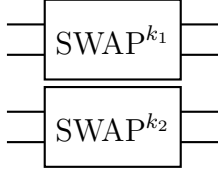
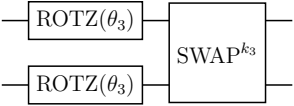
Group 1. Voltage-only driven gates				
Description	Gate layout	Relevant constants	Relevant shapes	Requirements
Idling qubits	—	$A'_- = 0$		No exchange with adjacent qubits:
Z rotations by any angles		$A'_{+,j} = 2\theta_j$	$S_{g,j}(t)$ any	$C_{j-1} =$ $C_j = 0$
Any SWAP <sup>k</sup> gates on separated pairs		$C_j = \pi k_j$	$S_{j,j}(t)$ any	Unaffected by spin rotations:  $A'_{-,j} =$ $A'_{-,j+1} = 0$
Hybrid ROT-SWAP gates: synchronous Z rotations within each		$A'_{+,j} =$ $A'_{+,j+1} =$ $2\theta_j$  $C_j = \pi k_j$	$S_{g,j}(t) =$ $S_{g,j+1}(t)$  $S_{j,j}(t)$ any	No exchange with the qubits adjacent to the pair:  $C_{j-1} =$ $C_{j+1} = 0$
Global parameters		$\beta = 0$		

Table 4.3: Voltage-only driven quantum gates (no ESR field) that can be run in parallel.

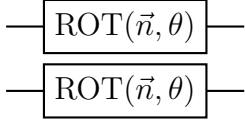

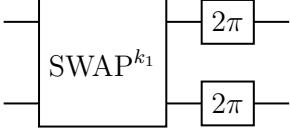
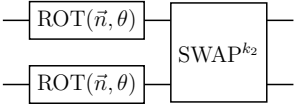
Group 2. Voltage and ESR driven gates				
Description	Gate layout	Relevant constants	Relevant shapes	Requirements
Synchronous arbitrary rotations $\text{ROT}(\vec{n}, \theta)$		$A'_+ = 2n_z\theta$	$S_g(t) = S_\Omega(t)$	No exchange with adjacent qubits: $C_{j-1} = C_j = 0$
Synchronous nonresonant $2\pi$ rotations		$A'_- = \pm 2 [4\pi^2 - \theta^2 \times (n_x^2 + n_y^2)]^{1/2}$		
ROT-SWAP gates on non-resonant qubits acting as “pure” $\text{SWAP}^k$ gates		$A'_-$ same as above $C_j = \pi k_j$	$S_g(t) = S_\Omega(t)$ $S_{j,j}(t)$ any	No exchange with the qubits adjacent to the pair: $C_{j-1} = C_{j+1} = 0$
Hybrid ROT-SWAP gates on resonant qubits		$A'_+ = 2n_z\theta$ $C_j = \pi k_j$		
Global parameters		$\beta =  \theta  \sqrt{n_x^2 + n_y^2}$ $\phi(t) = \text{atan2}(n_y \text{ sign } S(t), n_x \text{ sign } S(t))$		

Table 4.4: Quantum gates generated by both voltage and ESR field pulses that can be run in parallel.

## 4.5 Engineering of voltage pulses

### 4.5.1 Connection between physical and effective parameters

In our architecture, the potential landscape for the electrons in each computational node is defined by a series of plunger gates and tunnel gates in between. The case of  $N$  quantum dots corresponds to  $N$  plunger gates and  $N - 1$  tunnel gates in total, see figure 4.5.

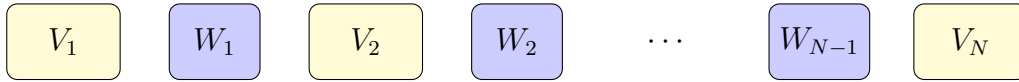


Figure 4.5: Diagram of plunger and tunnel gate arrangement in the qubit node.

In section 4.3, we developed a technique to manipulate effective parameters in the spin space, namely  $N$  deviation  $g$ -factor parameters and  $N - 1$  exchange couplings, to realize desired quantum gates. However, in an array of closely-packed dots, the effect of cross-coupling is always present. This means that changes of each plunger and tunnel gate voltage necessarily affect several dots at once (the effect on the dots in closest proximity to the gates is the most significant, though all dots are affected in the general case). Therefore, each of the effective parameters is a nontrivial function of all plunger and tunnel gate voltages:

$$\begin{aligned} \delta g_i &= \delta g_i(\vec{V}, \vec{W}), & i &= 1, \dots, N, \\ J_j &= J_j(\vec{V}, \vec{W}), & j &= 1, \dots, N - 1. \end{aligned} \quad (4.83)$$

Here and throughout, all  $g$ -factors/their deviations and exchange couplings will be grouped in vectors  $\vec{g}(\vec{V}, \vec{W})/\delta\vec{g}(\vec{V}, \vec{W})$  of length  $N$ , and a vector  $\vec{J}(\vec{V}, \vec{W})$  of length  $N - 1$ , respectively. For any set of voltages  $\{\vec{V}, \vec{W}\}$ , we can extract the dependencies (4.83) from the gate geometries emulated in `nextnano++` using the algorithm outlined in subsection 3.4.3 of the previous chapter. Thus, for the purpose of voltage pulse gate design, we consider the mapping of the physical (voltages) onto effective parameters to be described by a set of *known* functions (4.83). Even though they cannot be specified or estimated *a priori*, some relations between physical and effective parameters are expected to be true for all physically realistic scenarios. In particular, each parameter  $\delta g_i$  is much more sensitive to the voltage  $V_i$  on the plunger gate that defines the corresponding  $i^{\text{th}}$  dot than to any other voltage. Analogously, each parameter  $J_j$  is significantly more sensitive to the voltage  $W_j$

on the tunnel gate that controls the coupling of the  $j^{\text{th}}$  pair of dots:

$$\begin{aligned} \left| \frac{\partial \delta g_i}{\partial V_i} \right| &\equiv \left| \frac{\partial g_i}{\partial V_i} \right| > \sum_{l=1, l \neq i}^N \left| \frac{\partial g_i}{\partial V_l} \right| + \sum_{k=1}^{N-1} \left| \frac{\partial g_j}{\partial W_k} \right|, & i = 1, \dots, N, \\ \left| \frac{\partial J_j}{\partial W_j} \right| &> \sum_{l=1}^N \left| \frac{\partial J_j}{\partial V_l} \right| + \sum_{k=1, k \neq j}^{N-1} \left| \frac{\partial J_j}{\partial W_k} \right|, & j = 1, \dots, N-1. \end{aligned} \quad (4.84)$$

Therefore, if we construct a Jacobian matrix for the vector functions in units of frequency  $\omega \delta \vec{g}(\vec{V}, \vec{W})$  and  $\frac{1}{\hbar} \vec{J}(\vec{V}, \vec{W})$ :

$$\hat{I}(\vec{V}, \vec{W}) = \frac{\partial(\omega \delta \vec{g}, \vec{J}/\hbar)}{\partial(\vec{V}, \vec{W})} \equiv \frac{\partial(\omega \vec{g}, \vec{J}/\hbar)}{\partial(\vec{V}, \vec{W})} = \begin{pmatrix} \omega \frac{\partial g_1}{\partial V_1} & \cdots & \omega \frac{\partial g_1}{\partial V_N} & \omega \frac{\partial g_1}{\partial W_1} & \cdots & \omega \frac{\partial g_1}{\partial W_{N-1}} \\ \vdots & \ddots & \vdots & \vdots & \ddots & \vdots \\ \omega \frac{\partial g_N}{\partial V_1} & \cdots & \omega \frac{\partial g_N}{\partial V_N} & \omega \frac{\partial g_N}{\partial W_1} & \cdots & \omega \frac{\partial g_N}{\partial W_{N-1}} \\ \frac{1}{\hbar} \frac{\partial J_1}{\partial V_1} & \cdots & \frac{1}{\hbar} \frac{\partial J_1}{\partial V_N} & \frac{1}{\hbar} \frac{\partial J_1}{\partial W_1} & \cdots & \frac{1}{\hbar} \frac{\partial J_1}{\partial W_{N-1}} \\ \vdots & \ddots & \vdots & \vdots & \ddots & \vdots \\ \frac{1}{\hbar} \frac{\partial J_{N-1}}{\partial V_1} & \cdots & \frac{1}{\hbar} \frac{\partial J_{N-1}}{\partial V_N} & \frac{1}{\hbar} \frac{\partial J_{N-1}}{\partial W_1} & \cdots & \frac{1}{\hbar} \frac{\partial J_{N-1}}{\partial W_{N-1}} \end{pmatrix}, \quad (4.85)$$

then the inequalities (4.84) suggest that the matrix is strictly diagonally dominant and thus nonsingular.

Unfortunately, there is no straightforward way to construct an inverse mapping to (4.83) (i.e. effective back to physical parameters), and it is not guaranteed to be single-valued. The importance of finding this inverse mapping, though, is evident even for the simplest physical systems. Indeed, even in a double quantum dot, the voltage changes on the second plunger gate will disrupt the operation of single-qubit rotations in the first dot (and vice versa) unless the cross-coupling effects are accounted for by adjusting the shapes of voltage pulses. Therefore, the *goal* of this section is to prove that by imposing additional constraints on the time-dependent effective parameters, one can uniquely, unambiguously and efficiently determine all corresponding voltage pulses.

## 4.5.2 Voltage values for idling qubits

At first, it is important to find the optimal voltage configuration for qubits to stay in the idling state so that no undesired spin evolution happens. In particular, all effective pulses

devised in section 4.3 rely on an explicit value of  $\delta g_0$ , and no approach has been proposed so far to find it.

Technically speaking, the exact value of  $\delta g_0$  does not matter so long as it is the same for all qubits in the system; the Zeeman field and/or ESR frequency (both are global parameters) can be adjusted accordingly to satisfy the condition (4.36). However, it is natural to search for the voltage value offsets  $\Delta\vec{V}, \Delta\vec{W}$  on plunger and tunnel gates that not only give the same  $\delta g_0$  value for all qubits but also satisfy the most important constraint of the qubit operation: stability of charge configuration.

Thus, we can construct a minimization problem for a relevant cost function with additional constraints on  $\delta g_0$  and exchange coupling values  $\Delta J$ , which should obviously be very small at idle. For the cost function, we choose expression (4.26) with some simplifications:

1. As we are constructing a stationary idling state, time dependencies and integration are dropped;
2. The activation function is removed: we are looking specifically for the *most optimal* charge stability configuration, not the range of allowed voltage values.

With these considerations, the constrained minimization problem can be written as follows:

$$\left\{ \begin{array}{l} \tilde{f}_{\text{cs}}(\Delta\vec{V}, \Delta\vec{W}) = \frac{1}{(M-1)} \sum_{k \neq k_0} \frac{E_{k_0}(\Delta\vec{V}, \Delta\vec{W})}{E_k(\Delta\vec{V}, \Delta\vec{W})} \longrightarrow \min_{\Delta\vec{V}, \Delta\vec{W}}, \\ \delta g_{i+1} - \delta g_i = 0, \quad i = 1, \dots, N-1, \\ J_j - \Delta J = 0, \quad j = 1, \dots, N-1. \end{array} \right. \quad (4.86)$$

Here, the  $k_0$  is the composite index that corresponds to the desired charge configuration  $\vec{Q}^{(0)}$ . The initial guess  $\Delta\vec{V}_0, \Delta\vec{W}_0$  can be chosen at the global minimum value of the function  $\tilde{f}_{\text{cs}}$ . The choice of the constant  $\Delta J$  was discussed when the SWAP<sup>k</sup> pulses were designed in section (4.3.6).

Once the optimal solution is found, the value of  $\delta g_0$  is simply set to value:

$$\delta g_0 = \delta g_i \left( \Delta\vec{V}_{\text{opt}}, \Delta\vec{W}_{\text{opt}} \right) \quad \text{for any } i \in \{0, \quad i = 1, \dots, N\}, \quad (4.87)$$

where the offset values  $\Delta\vec{V}_{\text{opt}}, \Delta\vec{W}_{\text{opt}}$  are expected to be close to the center of the desired charge stability region. For brevity, the ‘‘opt’’ subscripts will be dropped throughout.

### 4.5.3 General formalism for voltage control pulse engineering

Once the offset values for all voltages are found, we can proceed with developing a method to map the values of effective variables  $\delta\vec{g}$ ,  $\vec{J}$  to the physically controlled voltages  $\vec{V}$ ,  $\vec{W}$ . The temporal dependencies of the effective variables that realize certain quantum operations on spin qubits are described by formulas (4.81). The freedom to choose the effective pulses is due to the dimensionless shape functions they correspond to, and the relations between the shape functions for different effective parameters. It turns out that by imposing a set of constraints of type (4.3) that the shape function  $S(t)$  is the *same for all nonzero* effective pulse parameters except piecewise constant ESR phase from expression (4.63):

$$\begin{aligned} 1 \leq i \leq N \\ 1 \leq j \leq N-1 : \quad S(t) &= \frac{\delta g_i(\vec{V}(t), \vec{W}(t)) - \delta g_0}{\langle \delta g_i(\vec{V}(t), \vec{W}(t)) - \delta g_0 \rangle} = \frac{J_j(\vec{V}(t), \vec{W}(t)) - \Delta J}{\langle J_j(\vec{V}(t), \vec{W}(t)) - \Delta J \rangle} = \frac{\Omega(t)}{\langle \Omega(t) \rangle}, \\ \phi(t) &= \text{atan2}\left(n_y \text{sign } S(t), n_x \text{sign } S(t)\right), \end{aligned} \quad (4.88)$$

we can devise a deterministic algorithm to find the voltage pulses for a wide class of shapes simultaneously.

To prove this, we start with equations (4.81) in a vectorized form :

$$\begin{aligned} \omega \left[ \delta\vec{g}(\vec{V}, \vec{W}) - \delta g_0 \vec{\mathbf{1}}_N \right] &= \vec{A}' \frac{S}{T}, \\ \frac{\vec{J}(\vec{V}, \vec{W})}{\hbar} &= \frac{\Delta J}{\hbar} \left( \vec{\mathbf{1}}_{N-1} - \vec{r} S \right) + \vec{C}' \frac{S}{T}. \end{aligned} \quad (4.89)$$

Here, the symbol  $\vec{\mathbf{1}}_N$  denotes a column vector of length  $N$  with all elements equal to 1. The constant parameters both for “resonant” and “nonresonant” qubits, grouped in vectors  $\vec{A}'$ ,  $\vec{C}'$ ,  $\vec{r}$ , are summarized in formula (4.82) and tables 4.3 and 4.4. By equating the exact differentials of both sides of the equation, we obtain:

$$\frac{\partial \left( \omega\vec{g}, \vec{J}/\hbar \right)}{\partial \left( \vec{V}, \vec{W} \right)} \begin{pmatrix} d\vec{V} \\ d\vec{W} \end{pmatrix} \equiv \hat{I}(\vec{V}, \vec{W}) \begin{pmatrix} d\vec{V} \\ d\vec{W} \end{pmatrix} = dS \left( \frac{\vec{C}'}{T} - \frac{\vec{A}'}{T} - \frac{\Delta J}{\hbar} \vec{r} \right). \quad (4.90)$$

We proved in subsection 4.5.1 that the Jacobian matrix  $\hat{I}(\vec{V}, \vec{W})$  is nonsingular in all physically realistic scenarios of quantum dot operation; therefore, its inverse exists with certainty and is unique. This enables us to multiply both sides of equation (4.90) by the

inverse  $\hat{I}^{-1}$  and divide by  $dS$  to obtain a system of ordinary differential equations for  $\vec{V}(S), \vec{W}(S)$ :

$$\frac{d}{dS} \begin{pmatrix} \vec{V} \\ \vec{W} \end{pmatrix} = \hat{I}^{-1}(\vec{V}, \vec{W}) \begin{pmatrix} \frac{\vec{A}'}{T} \\ \frac{\vec{C}}{T} - \frac{\Delta J}{\hbar} \vec{r} \end{pmatrix}. \quad (4.91)$$

Since the values of  $S = 0$  correspond to the situation when no spin qubit evolution happens, the corresponding voltages must correspond to their offset values:

$$\vec{V}(S = 0) = \Delta \vec{V}, \quad \vec{W}(S = 0) = \Delta \vec{W}. \quad (4.92)$$

The equations (4.91) and (4.92) define an initial value problem for vector functions  $\vec{V}(S), \vec{W}(S)$  that is trivially solved numerically (e. g. by one of Runge-Kutta methods) and is guaranteed to have a unique solution for fixed constants  $\vec{A}', \vec{C}, \vec{r}$  and pulse duration  $T$ . Remarkably, there is no explicit dependency on time in (4.91), which means that the obtained solutions  $\vec{V}(S), \vec{W}(S)$  are the same for *any* shape functions! The time dependency propagates into the solutions for voltage pulses from the chosen dependency  $S(t)$ :

$$\vec{V}(t) = \vec{V}(S(t)), \quad \vec{W}(t) = \vec{W}(S(t)). \quad (4.93)$$

The only requirement to make the solutions applicable to a wide enough class of shapes is to numerically integrate the system (4.91) up to reasonably large values of  $|S|$ . We established in subsec. (4.3.2) that the maximal values of  $S(t)$  are of the order of unity for all typical pulse shapes. Thus, for instance, the integration over the intervals  $[0, 10]$  forwards, and then  $[-10, 0]$  backwards is sufficient to cover a very wide class of shape functions with the property:

$$-10 \leq S_{min} < S_{max} \leq 10.$$

We can further improve our results by ignoring the exchange offset value  $\Delta J/\hbar$  compared to any  $C_j/T$ . We already discussed in subsection 4.3.6 that this approximation will give only a negligible error for all realistic quantum circuits. On the other hand, we know now that the voltage pulses  $\vec{V}(t), \vec{W}(t)$  are constructed by numerical integration, which is likely to give an error comparable to the truncation of  $\Delta J$ . Moreover, such simplification gives strictly zero error to the nonresonant qubit terms because  $C_j = r_j = 0$  for them anyway (cf. tab. 4.3). Within this approximation, the pulse duration  $T$  factors out of the expression on the right in equation (4.91), so we can rewrite it as follows:

$$\frac{d}{d(S/T)} \begin{pmatrix} \vec{V} \\ \vec{W} \end{pmatrix} = \hat{I}^{-1}(\vec{V}, \vec{W}) \begin{pmatrix} \vec{A}' \\ \vec{C} \end{pmatrix}. \quad (4.94)$$

Clearly, the solutions of this simplified system of ODEs are functions of a variable  $S/T$  rather than simply  $S$ . Consequently, if we numerically obtain the functions  $\vec{V}_0(S), \vec{W}_0(S)$  for some small value  $T = T_0$  (smaller than the typical pulse duration we could expect), all voltage functions of  $S$  at different pulse durations can be found simply by scaling the argument:

$$\vec{V}(S, T) = \vec{V}_0\left(S\frac{T_0}{T}\right), \quad \vec{W}(S, T) = \vec{W}_0\left(S\frac{T_0}{T}\right), \quad T_0 < T. \quad (4.95)$$

This leads us to the final conclusion that only one numerical integration of a vector initial value problem is enough to engineer voltage pulses of any duration  $T > T_0$  and any desired shape of the corresponding effective pulses  $S(t)$ . This result is particularly remarkable because all interdot couplings are taken into account automatically through the Jacobian matrix function.

#### 4.5.4 Constraint satisfaction

One of the most important results from the previous subsection is that the gate voltage pulses do not explicitly depend on time when expressed in terms of the shape function value  $S$ . Hence, we can redefine the cost function so that it penalizes high values of  $S$  directly:

$$f^{(S)} = w_{\text{CS}}f_{\text{CS}}^{(S)} + w_{\text{BF}}f_{\text{BF}}^{(S)} + w_{\text{VW}}f_{\text{VW}}^{(S)}, \quad w_{\text{CS}} + w_{\text{BF}} + w_{\text{VW}} = 1. \quad (4.96)$$

The physical constraints that the terms in the sum represent remain the same as discussed in subsection 4.2.3 but the expressions will change. This section will demonstrate that removing the explicit time dependency from consideration significantly simplifies the search for the shortest pulse duration  $T_{\text{opt}}$  that satisfies system constraints.

Consider a class of shape functions with the domain lying within  $[S_{\text{min}}, S_{\text{max}}]$ . Then, the charge stability component of the cost function from formula (4.26) can be rewritten as follows:

$$f_{\text{CS}}^{(S)}(T, S_{\text{min}}, S_{\text{max}}, \lambda, \alpha'', \beta) = \frac{1}{(M-1)(S_{\text{max}} - S_{\text{min}})} \int_{S_{\text{min}}}^{S_{\text{max}}} dS \times \left\{ \sum_{k'} \Xi_p \left[ K_{\text{CS}} \left( k', k_0, \vec{V}_0 \left( S\frac{T_0}{T} \right), \vec{W}_0 \left( S\frac{T_0}{T} \right) \right), \lambda \frac{t_{k_0, k'} \coth(t_{k_0, k'} / k_B T_e)}{2E'_k(\vec{V}_0(S\frac{T_0}{T}), \vec{W}_0(S\frac{T_0}{T}))} \right] + \sum_{k''} \Xi_p \left[ K_{\text{CS}} \left( k'', k_0, \beta, \vec{V}_0 \left( S\frac{T_0}{T} \right), \vec{W}_0 \left( S\frac{T_0}{T} \right) \right), \alpha'' \right] \right\}, \quad (4.97)$$



where the constants  $\lambda, \alpha'', \beta$  are user-specified; please refer to the subsec. 4.2.4 for the definition of other functions and parameters. Here, we shift from the integration over time-dependent voltage pulses  $\vec{V}(t), \vec{W}(t)$  to the integration over the possible values of effective pulses  $S \frac{T_0}{T}$ , scaled according to expressions (4.95). Therefore,  $f'_{cs}$  is a function of a single variable  $T$  (rather than a functional of  $\vec{V}(t), \vec{W}(t)$ ), and so its minimization can be expressed a simple root finding problem! In particular, it is enough to find the minimal possible value  $T_{cs}$  that sets this function to zero; the initial guess can be chosen as  $T_0$ :

$$\text{Find smallest } T_{cs} : \quad f_{cs}^{(S)}(T_{cs}, S_{min}, S_{max}, \lambda, \alpha'', \beta) = 0, \quad T_{cs}^{(0)} = T_0. \quad (4.98)$$

Analogous reasoning applies to the limitation on voltage sweep rates. The relevant quantities to minimize (voltage time derivatives) can be then written as follows:

$$\vec{\mathcal{V}}(t) = \partial_t \begin{pmatrix} \vec{V}_0 \left( S(t) \frac{T_0}{T} \right) \\ \vec{W}_0 \left( S(t) \frac{T_0}{T} \right) \end{pmatrix} = \dot{S}(t) \frac{d}{dS} \begin{pmatrix} \vec{V}_0 \left( S \frac{T_0}{T} \right) \\ \vec{W}_0 \left( S \frac{T_0}{T} \right) \end{pmatrix}, \quad \dot{S}(t) \equiv \frac{dS(t)}{dt}. \quad (4.99)$$

The expression simplifies if we take (4.94) into account:

$$\vec{\mathcal{V}}(t) = \frac{\dot{S}(t)}{T} \hat{I}_0^{-1}(S, T) \begin{pmatrix} \vec{A}' \\ \vec{C}' \end{pmatrix}, \quad \text{where } \hat{I}_0(S, T) = \hat{I} \left( \vec{V}_0 \left( S \frac{T_0}{T} \right), \vec{W}_0 \left( S \frac{T_0}{T} \right) \right). \quad (4.100)$$

When we choose a particular function  $S(t)$ , we automatically know the minimal and maximal values of its time derivative:  $\dot{S}_{min}, \dot{S}_{max}$ . Therefore, we can replace  $|\dot{S}(t)|$  with its upper limit:

$$|\dot{S}(t)| \leq \dot{S}_0 \equiv \max \left( |\dot{S}_{min}|, \dot{S}_{max} \right),$$

and replace time integration with the integration over  $S$  in formula (4.31):

$$f_{vw}^{(S)}(T, S_{min}, S_{max}, \alpha) = \frac{1}{(2N-1)(S_{max} - S_{min})} \int_{S_{min}}^{S_{max}} dS \times \hat{\Xi}_p(\circ, \alpha) \left[ \frac{\dot{S}_0^2}{\partial_t \mathcal{V}_{max}^2 T^2} \begin{pmatrix} \vec{A}'^T & \vec{C}'^T \end{pmatrix} \left( \hat{I}_0(S, T) \hat{I}_0^T(S, T) \right)^{-1} \begin{pmatrix} \vec{A}' \\ \vec{C}' \end{pmatrix} \right]. \quad (4.101)$$

The shorthand operator notation notation  $\hat{\Xi}_p(\circ, \alpha) [\dots]$  implies that the activation function  $\Xi_p(x_i, \alpha)$  is applied on each element  $x_i$  of the sum in square brackets. Again, we end up with nothing but a root finding problem for a single variable  $T$ , where we can choose the initial guess in the same way as before:

$$\text{Find smallest } T_{vw} : \quad f_{vw}^{(S)}(T_{vw}, S_{min}, S_{max}, \alpha) = 0, \quad T_{vw}^{(0)} = T_0. \quad (4.102)$$

The last constraint we consider (limit on electromagnetic radiation absorption) turns to give the simplest result. Expression (4.29) implies that the corresponding cost function is zero if the following inequality holds at all times:

$$\forall t : \quad \left( \frac{\Omega(t)}{\Omega_{max}} \right)^2 \leq 1 - \alpha \quad \Rightarrow \quad f_{\text{RF}} \equiv 0. \quad (4.103)$$

Since  $\Omega(t) = B \frac{S(t)}{T}$  for single-qubit rotations (cf. eq. (4.63)), and  $S(t)$  is a continuous function, it is sufficient to demand that (4.103) holds for  $S_{min}$  and  $S_{max}$ . From this, we immediately obtain the minimal pulse duration that satisfies this constraint:

$$T_{\text{RF}} = \frac{\beta}{\Omega_{max} \sqrt{1 - \alpha}} \max(|S_{min}|, S_{max}). \quad (4.104)$$

Combining the results (4.98), (4.102), and (4.104), we conclude that the optimal pulse duration:

$$T_{opt} = \max(T_{\text{CS}}, T_{\text{VW}}, T_{\text{RF}}) \quad (4.105)$$

can be found by only one series of simple single-variable minimizations for the whole class of shape functions that satisfy  $S_{min} \leq S(t) \leq S_{max}$ .

### 4.5.5 Choice of shape function

The results derived earlier in this section demonstrate that all voltage pulses are linked with each other through the shape function  $S(t)$  of the corresponding effective pulses. This makes it impossible to choose  $S(t)$  and pulse duration  $T$  so that all voltage pulses have some preferred shapes simultaneously. Nevertheless, it is possible to select  $S(t)$  which yields the voltage pulses with shapes being close to the desired ones. To show this, we use the fact that the dominant contribution to  $\delta g_i$  is the plunger gate voltage  $V_i$ , and the one for  $J_j$  is the tunnel gate voltage  $W_j$  for all physically realistic scenarios (see the discussion in subsection 4.5.1 for more details).

Suppose a single-qubit rotation of the  $i^{\text{th}}$  qubit should occur, and we would prefer to supply a voltage pulse  $\tilde{V}_i(t)$  to drive this rotation (of course, this pulse must satisfy  $\tilde{V}_i(0) = \tilde{V}_i(T) = \Delta V_i$ ). Then, we can extract the shape function of the corresponding  $g$ -factor pulse when other voltages remain at their idling values:

$$\tilde{S}(t) = \frac{\delta g_i(\Delta V_1, \dots, \Delta V_{i-1}, \tilde{V}_i(t), \Delta V_{i+1}, \dots, \Delta V_N, \Delta \vec{W}) - \delta g_0}{\left\langle \delta g_i(\Delta V_1, \dots, \Delta V_{i-1}, \tilde{V}_i(t), \Delta V_{i+1}, \dots, \Delta V_N, \Delta \vec{W}) - \delta g_0 \right\rangle}. \quad (4.106)$$

This shape can then be assigned to all effective parameters, which is required to make the formalism devised in subsection 4.5.3 applicable. When cross couplings are not very strong, it is reasonable to expect that the actual voltage pulse  $V_i(t)$  obtained from the numerical integration of (4.94) will not significantly differ from the desired one  $\widetilde{V}_i(t)$ . Moreover, if other plunger gates have similar geometry (which is typically the case), one would expect the voltage pulses on them  $V_l(t), l \neq i$  to be similar in shape to  $\widetilde{V}_i(t)$  if they drive single-qubit rotations on other qubits in parallel.

Analogously, if a SWAP<sup>k</sup> gate is applied on the  $j^{\text{th}}$  pair of qubits, we can infer the shape for all effective variable pulses from the exchange produced by the desired tunnel gate voltage pulse  $\widetilde{W}_j(t)$ :

$$\widetilde{S}(t) = \frac{J_j(\Delta\vec{V}, \Delta W_1, \dots, \Delta W_{j-1}, \widetilde{W}_j(t), \Delta W_{j+1}, \dots, \Delta W_N) - \Delta J}{\langle J_j(\Delta\vec{V}, \Delta W_1, \dots, \Delta W_{j-1}, \widetilde{W}_j(t), \Delta W_{j+1}, \dots, \Delta W_N) - \Delta J \rangle}. \quad (4.107)$$

When exchange and rotation gates are applied simultaneously in parallel or on the same qubits — both scenarios are realizable in our architecture, as shown in subsec. 4.4 — the shape of a single-qubit rotation gate should be given priority. The reason is that the typical durations of exchange pulses are 2–3 orders of magnitude smaller than those of spin rotations. Therefore, tunnel gates will require much smaller voltage sweeps than plunger gates, and so it is more important to optimize the voltage pulses for the latter.

## 4.6 Examples of single-qubit gate simulations

### 4.6.1 Relations between effective and physical parameters for a standalone quantum dot

Now we go on to the demonstration of the proposed pulse engineering algorithm in action. For the simplest case, we perform electric potential and field simulations in `nextnano++` for the gate geometry<sup>1</sup> outlined in figure 4.6. Please note that only for the discussion of device design, we change the coordinate axes convention used previously so that the Si/SiO<sub>2</sub> interface lies in the  $xy$  plane: this choice of axes is the standard `nextnano++` behavior. The structure models a silicon substrate (red) with a layer of SiO<sub>2</sub> (blue) on top. The 2-dimensional electron gas forms just below the Si/SiO<sub>2</sub> interface. An elongated plunger gate (green), embedded in the layer of the oxide, is used to define a single quantum dot. A grounded screening gate (yellow) localizes the electric field induced by the plunger gate (and thus the quantum dot) to the middle of the sample. The uncovered part of the plunger gate is  $40 \times 40$  nm in size; the oxide thickness between the plunger gate and the Si/SiO<sub>2</sub> interface is 10 nm.

For the simulations of control scheme proposed earlier in this chapter, we assume that an actual quantum dot array contains two identical gate structures of this kind, separated far enough so that the effects of cross coupling can be ignored. In this case, the mapping between the effective and physical parameters is conveniently described by a single function  $\delta g$ :

$$\delta g_1(V_1) = \delta g(V_1), \quad \delta g_2(V_2) = \delta g(V_2).$$

Therefore, we are free to supply voltage pulses of any shapes so long as the constraint on the shape of effective pulses is satisfied. From now on, we will be using voltage pulses with a Gaussian shape. In terms of the normalized time  $\tau = t/T$ , such pulse profiles are described by the following:

$$V(\tau) = \Delta V + \frac{V_{max} - \Delta V}{1 - e^{-\frac{1}{8\sigma^2}}} \cdot \left( e^{-\frac{(\tau-1/2)^2}{2\sigma^2}} - e^{-\frac{1}{8\sigma^2}} \right), \quad \tau = \frac{t}{T}, \quad \tau \in [0, 1] \quad (4.108)$$

Here,  $V_{max}$  is the maximum voltage value during the pulse,  $\Delta V$  is the voltage offset before and after the pulse,  $\sigma$  is the dimensionless width of the pulse relative to its length  $T$ . The

---

<sup>1</sup>The `nextnano++` simulations were performed by Rubaya Absar at the author's request

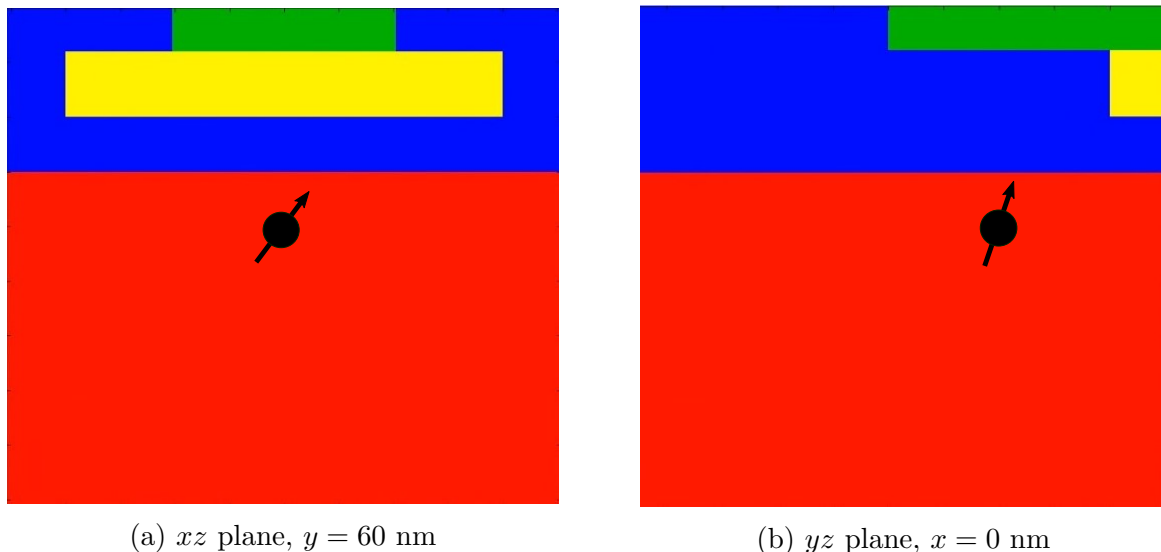


Figure 4.6: Projections of the single-dot device structure emulated in `nextnano++` on  $xz$  plane (a) and  $yz$  plane (b). Silicon substrate is shown in red,  $\text{SiO}_2$  in blue, plunger gate in green, and screening gate in yellow.

vertical shift of the Gaussian function by  $e^{-\frac{1}{s\sigma^2}}$  and subsequent normalization ensure that:

$$V(t = 0) = V(t = T) = \Delta V, \quad V\left(t = \frac{T}{2}\right) = V_{max}.$$

The simulations with `nextnano++` indicate that the charge accumulation threshold for the chosen device structure is approximately 0.7 V. For the consistent extraction of potential landscapes, we require that the voltage operation window lies just below this value (see the discussion in the subsec. 3.4.1). With this, we perform `nextnano++` simulations for the plunger gate voltage ranging from 0.5 to 0.7 V with the step of 0.025 V. Moreover, we choose  $\Delta V = 0.5$  V and  $V_{max} = 0.65$  V for all control pulses. At the values above 0.7 V, we observe charge accumulation with the density peak roughly at  $z = -0.2$  nm, which determines the position of 2DEG. The potential landscape  $U(x, y)$  and out-of-plane field  $E_z(x, y)$  profiles, extracted<sup>2</sup> at this depth for  $V = \Delta V$ , are presented in figure 4.7. The data reveals typical absolute values of the potential energy  $\sim 2$  eV and field  $\sim 60$  kV/cm in the middle of the quantum dot.

---

<sup>2</sup>Zach Merino is the author of the code for processing `nextnano++` simulation files

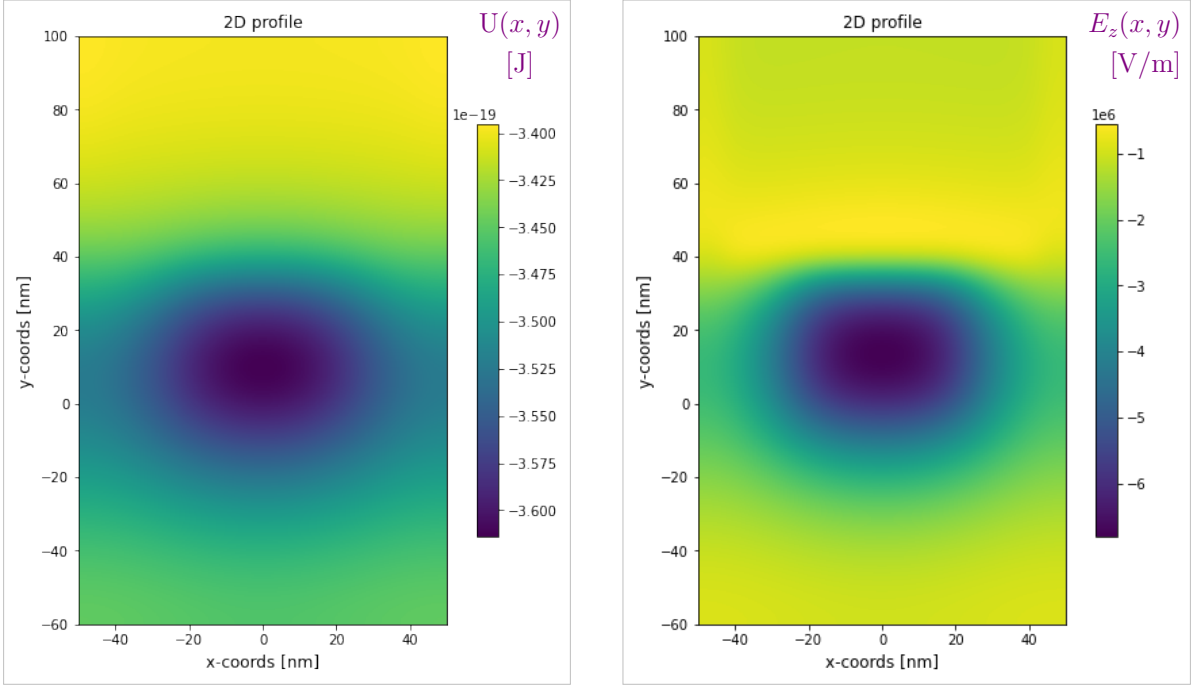


Figure 4.7: Potential energy and electric field landscapes, obtained from `nextnano++` simulation at  $z = -0.2$  nm,  $V = 0.5$  V.

The value of  $\sigma$  is directly connected to the voltage sweep rate during the pulse and thus should be limited in practice to satisfy the characteristics of a pulse generator. However, we do not impose this restriction here and choose  $\sigma = 0.1$  for all simulations.

Using formula (3.11), we calculate<sup>3</sup> the function  $\delta g(V)$  in the interval  $V \in [0.5 \text{ V}, 0.7 \text{ V}]$  from the simulated potential landscape and electric field data. The obtained dependency (plotted in fig. 4.8) proves to be almost perfectly linear with the slope  $\frac{dg}{dV} \approx 1.797 \cdot 10^{-4} \text{ V}^{-1}$ . To prevent spin evolution before and after pulses, we require that the value at voltage offset  $\delta g(\Delta V)$  corresponds to  $\delta g_0$ . For this, we set the resonator frequency to an experimentally realistic value and calculate the required static Zeeman field from the condition (4.36):

$$f_{\text{RF}} = 17 \text{ GHz}, \quad B_0 = 607.285 \text{ mT}.$$

---

<sup>3</sup>Stephen Harrigan is the author of the code used for deviation  $g$ -factor calculation

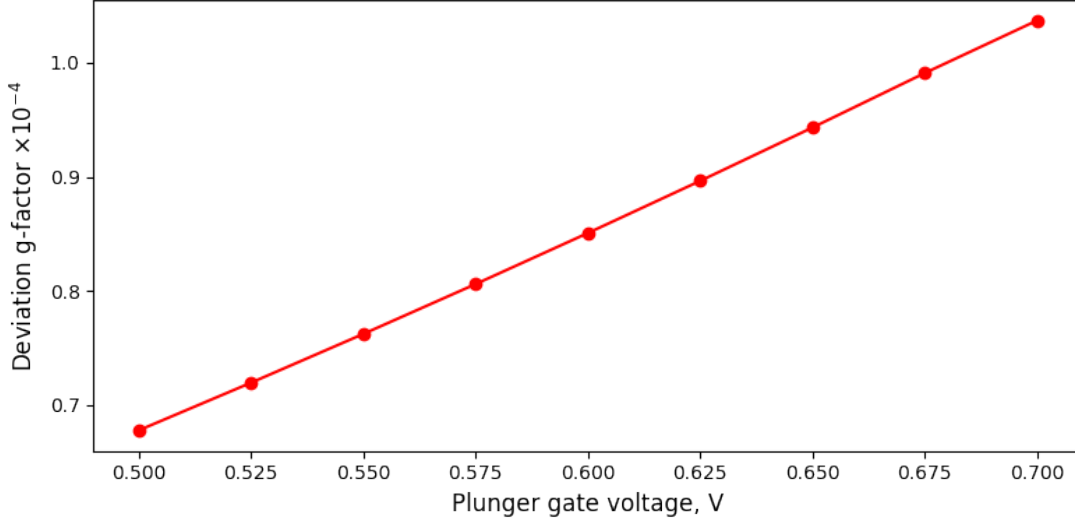


Figure 4.8: Deviation  $g$ -factor dependency on the plunger gate voltage in a single dot geometry, obtained from `nextnano++` electric potential and field data.

### 4.6.2 High-fidelity resonant and nonresonant spin rotations

To showcase the high-fidelity detuning of nonresonant qubits during ESR-driven spin rotations, we implement the quantum circuit from figure 4.9. At the beginning, a system of two qubits is in a pure  $|\uparrow\downarrow\rangle$  state. Three consecutive  $\frac{\pi}{2}$  rotations are applied onto the first qubit so that it returns into its initial state at the end; figure 4.10 gives a cartoon of this qubit evolution. In the meantime, the second qubit is kept off resonance all the time. For this, it performs nonresonant  $2\pi$  rotations during  $X$  and  $Y$  rotations of the first qubit to maintain its initial state between pulses (cf. sec. 4.3). The corresponding  $2\pi$  gates are explicitly shown in the circuit diagram 4.9 for clarity.

The data obtained in subsection 4.6.1 is almost sufficient to engineer control pulses for voltages  $V_1(t)$ ,  $V_2(t)$  and RF field  $\vec{B}_{\text{RF}}$  that realize the quantum circuit 4.9. One last necessary calculation is the pulse duration for each quantum gate (formula (4.64) is used):

$$T\left(\hat{x}, \frac{\pi}{2}\right) = T\left(\hat{y}, -\frac{\pi}{2}\right) = 17.448 \mu\text{s}, \quad T\left(\hat{z}, \frac{\pi}{2}\right) = 4.504 \mu\text{s}.$$

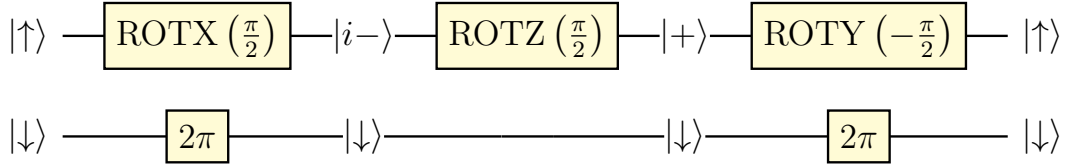


Figure 4.9: Single qubit rotation simulations of a system of two antiparallel spins. The first qubit is on resonance all the time, whereas the second qubit performs nonresonant  $2\pi$  rotations to compensate for the effect of the global ESR field.

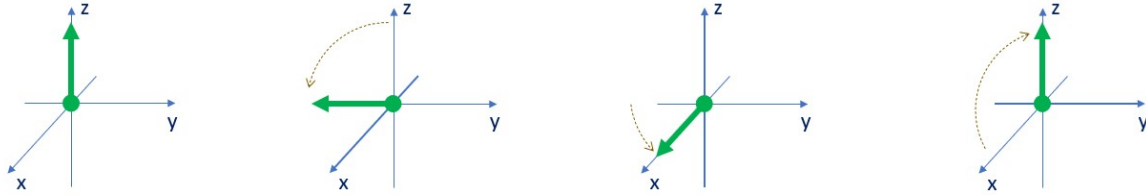


Figure 4.10: Evolution of the Bloch vector of the first electron at each step of the quantum circuit from fig. 4.9.

The simulated sequence of voltage and magnetic field pulses is presented in figure 4.11. No magnetic field is supplied during the Z rotation in the middle, whereas the voltage pulse  $V_1(t)$  drives a resonant transition on the first qubit at this time. Conversely, only the second plunger gate is active during the first and last quantum gate operations, when it is driving nonresonant  $2\pi$  rotations in conjunction with ESR field. Since the dependency  $\delta g(V)$  is almost perfectly linear (fig. 4.8), the shape of  $B_{\text{RF}}(t)$  is very similar to the Gaussian shape (4.108) of the pulse  $V_2(t)$ .

To confirm that the voltage and ESR sequence from figure 4.11 induces the desired evolution of a pure state  $|\uparrow\downarrow\rangle$ , we perform the simulation of the corresponding master equation (3.27) under the assumption of no decoherence ( $T_1 \rightarrow \infty, T_2 \rightarrow \infty$ ). The figure 4.12 summarizes the simulation results for the relevant spin system parameters. In particular, the Bloch vector dynamics of the first electron matches the expected behavior from the figure 4.10:  $\langle\sigma_{y1}\rangle$  reaches the value -1 after the first (X) rotation, proceeds to  $\langle\sigma_{x1}\rangle = 1$  after the second (Z) rotation, and returns to  $\langle\sigma_{z1}\rangle = 1$  after the last (Y) rotation. X and Y rotations clearly affect all Bloch vector components of the second qubit but always restore the value  $\langle\sigma_{z2}\rangle = -1$  when finished. The fidelity function with respect to



the initial state  $|\uparrow\downarrow\rangle$  is evaluated using formula (3.31):

$$\mathcal{F}(t) = \left( \text{Tr} \sqrt{\sqrt{\rho(t)} |\uparrow\downarrow\rangle\langle\uparrow\downarrow| \sqrt{\rho(t)}} \right)^2$$

and is shown at the bottom of figure 4.12. This function maintains the value  $\approx 0.5$  when the Bloch vector of the 1<sup>st</sup> spin rotates in the  $xy$  plane, perpendicular to the initial state vector, and approaches 1 when the system returns to  $|\uparrow\downarrow\rangle$  state. The simulated value of infidelity at the end is very low:

$$1 - \mathcal{F} \left( T\left(\hat{x}, \frac{\pi}{2}\right) + T\left(\hat{z}, \frac{\pi}{2}\right) + T\left(\hat{y}, -\frac{\pi}{2}\right) \right) = 7.135 \cdot 10^{-11},$$

and is due to the numerical error of the master equation integration. This confirms the correctness and high-fidelity yield of the control scheme developed earlier in this chapter.

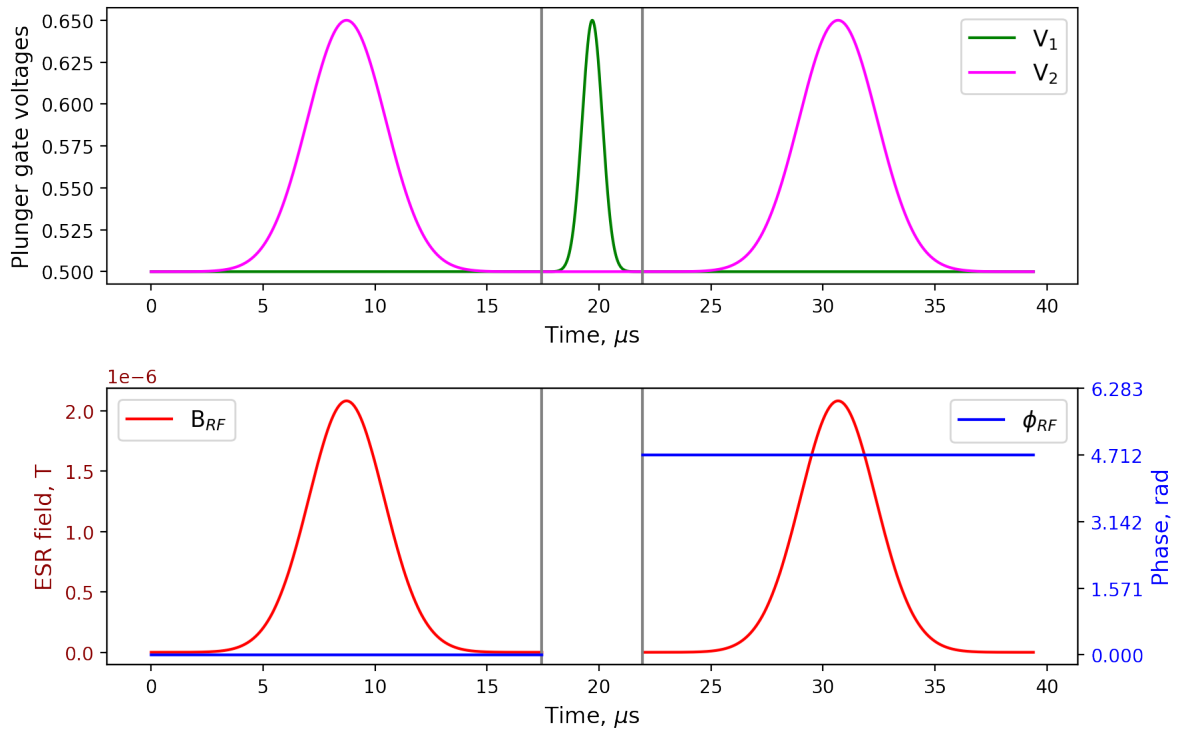


Figure 4.11: Sequence of voltage and ESR field control pulses that realizes the quantum circuit from figure 4.9. Gray vertical lines delimit distinct quantum operations. For the Z rotation in the middle, magnetic field is not supplied and is thus not shown.

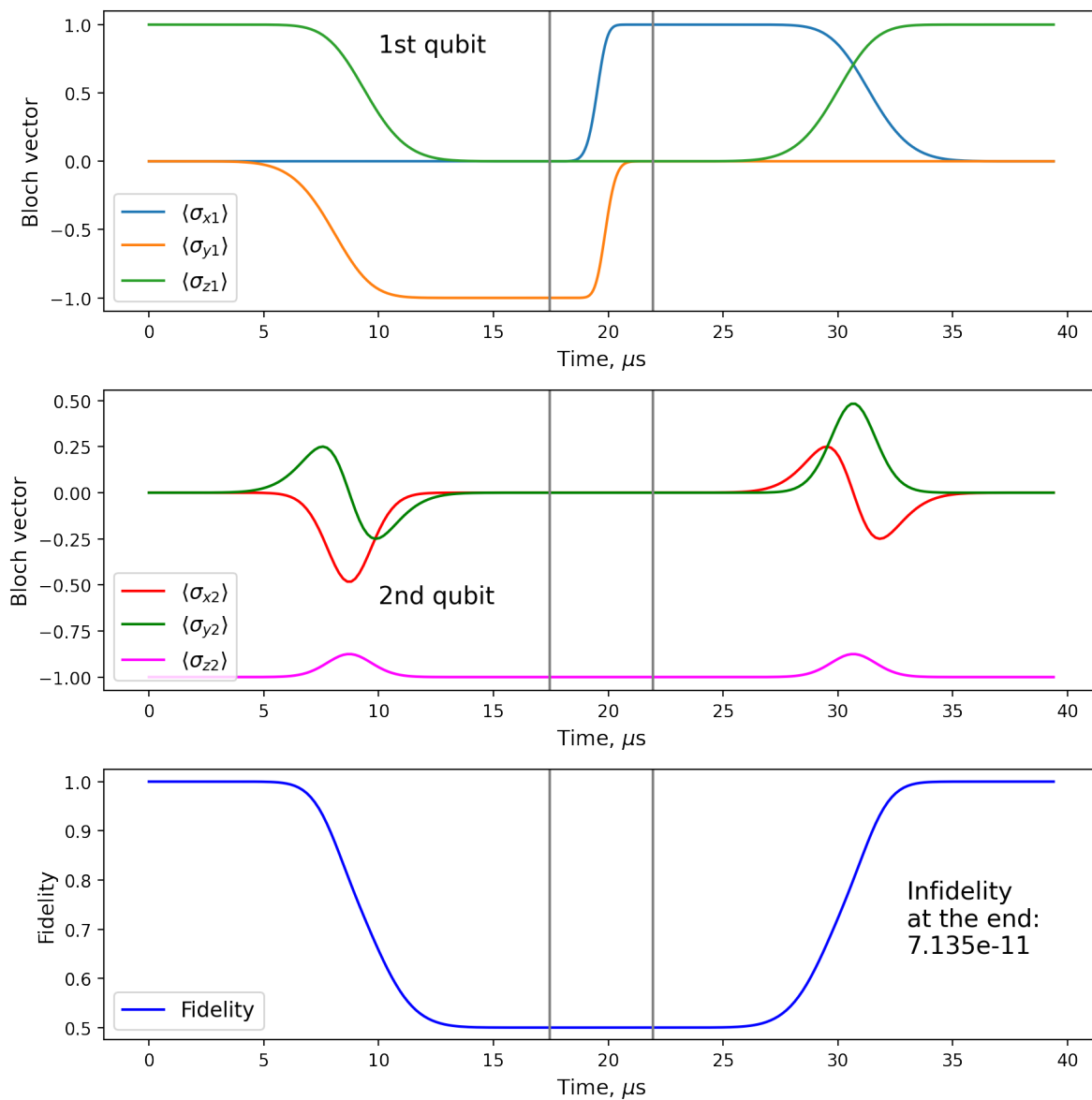


Figure 4.12: Time evolution of the 2-electron system spin state: Bloch vector components of the two spins (top and middle), and the state fidelity with respect to the initial state  $|\uparrow\downarrow\rangle$  (bottom). Gray vertical lines delimit distinct quantum operations.

## 4.7 Summary of chapter 4

In summary, a novel high-fidelity quantum control scheme is devised for the computer architecture [65]. The most important accomplishments described in this chapter include:

1. The problem of finding voltage and ESR magnetic field control pulses for the computer architecture [65] is formulated in a general case as a constrained minimization problem for a cost function. The expressions for cost function contributions that penalize charge configuration changes, fast voltage sweeps and large oscillating magnetic fields are derived.
2. A novel scheme for effective qubit control, based on the combination of global ESR control and slight local variations of  $g$ -factor, is proposed. The approach overcomes the complication of the off-resonance qubit tuning due to the weakness of Stark effect in silicon.
3. A very general form of constraints on the shapes of effective parameter pulses  $\delta g(t)$ ,  $J(t)$ ,  $\Omega(t)$  is shown to give deterministic spin evolution. Using these constraints, the effective pulses are constructed for single and two-qubit quantum gates operating with 100% theoretical fidelity.
4. Several approaches to reduce the execution time of quantum circuits within the proposed control scheme are developed. They include substitutions of spin rotations with equivalent ones, running quantum gates in parallel on different qubits, or simultaneously on the same groups of qubits.
5. A method to unambiguously construct voltage pulses  $V(t)$ ,  $W(t)$  that give the specified dependencies  $\delta g(t)$ ,  $J(t)$  is presented. The constraints that the ESR phase is constant on certain time intervals, and that all other effective parameter pulses have the same shape (up to normalization) are proven to be sufficient to achieve this.
6. The proposed voltage pulse engineering method is shown to be very numerically efficient. First of all, one numerical integration of a vector initial value problem maps the effective parameters to physically controlled ones for a very wide class of pulse shapes and durations. Secondly, cost function minimization is reduced to a computationally inexpensive single-variable root finding problem for the optimal pulse duration.

# Chapter 5

## Advanced pulse engineering with gradient ascent for a silicon spin qubit architecture

### 5.1 Motivation

Since its first development in the seminal work [84], the Gradient Ascent Pulse Engineering (GRAPE) method has attracted significant attention in the quantum computer design community. To realize desired quantum operations, the method discretizes control pulses into piecewise-constant sequences and finds the optimal values of control parameters for each interval of constancy. The method benefits from the natural properties of matrix exponentials that arise in the evaluation of evolution operators, which allow to limit the number of numerical operations during the algorithm. Ever since the publication [84], the field has seen a significant improvement in speed of convergence with the adoption of quasi-Newton Broyden–Fletcher–Goldfarb–Shanno (BFGS) [85], and later Newton-Raphson second-order [86] methods. Remarkably, all derivatives (even second order) require only linear time [87] to be computed — an uncommon property of gradient optimization methods — thereby allowing very fast minimization. The use of machine learning toolkits for automatic differentiation [88] and code deployment on graphics processing units (GPUs) [89] show a path towards even better optimization. The algorithmic and hardware improvements indicate that GRAPE is no longer prohibitively costly with respect to the computational time and memory use even for relatively large numbers of electrons.

As the GRAPE algorithm controls pulse values at individual small time intervals, it can directly incorporate any non-optimality mechanisms, including infidelity, susceptibility to decoherence and noise. This recently became the basis for such a significant achievement as single-qubit rotations with fidelities reaching incoherent noise limits in silicon quantum dots [90]. Implementing GRAPE will be a step towards even better optimized pulses than the ones designed in the previous chapter 4. In particular, it will allow us to lift stringent constraints of equal effective pulse shapes and piecewise constant ESR phase. Besides, one can naturally anticipate that these constrained pulses used as the initial guess for the GRAPE algorithms will yield intuitively comprehensible pulse shapes and magnitudes, as opposed to the case where random sequences are used for the initial guess (e.g. in [84]).

Following reference [91], the section 5.2 of this chapter introduces the the reader to the concepts of operator formalism applied to the case of piecewise constant parameters of quantum evolution. Using this formalism, the section 5.3 presents the cost function minimization problem for optimal pulse design establishes for our quantum computer architecture [65]. Section 5.4 summarizes the main results of the chapter.

Section 5.3 as well as the part of subsection 5.2.4 where the directional, scalar and mixed derivatives relevant to our control problem are derived, constitute the original contribution of the author.

## 5.2 Operator formalism for quantum system evolution

### 5.2.1 Liouville equation

As is well known, the dynamics of a spin quantum system with  $N$  electrons and the initial state  $|\psi(0)\rangle$  in the nondissipative case can be described by the Schrodinger equation for a unitary evolution operator:

$$\partial_t U(t) = -\frac{i}{\hbar} H(t)U(t) = -i\mathcal{H}(t)U(t), \quad U(0) = \mathbb{1}, \quad |\psi(t)\rangle = U(t) |\psi(0)\rangle,$$

where both the Hamiltonian  $H$  and the evolution operator  $U$  are  $2^N \times 2^N$  matrices. This is a special instance of a more general Liouville equation with an initial condition:

$$\partial_t \mathcal{G}(t) = \mathcal{L}(t)\mathcal{G}(t), \quad \mathcal{G}(0) = \mathbb{1}, \quad (5.1)$$

for the evolution of the propagator  $\mathcal{G}$  under the generator  $\mathcal{L}$ . In the simplest case, this is a bilinear control problem, i.e. the generator  $\mathcal{L}$  can be expressed as follows:

$$\mathcal{L}(t) = \mathcal{L}_0 + \sum_{k=1}^K a_k(t)\mathcal{L}_k, \quad (5.2)$$

where the scalars  $a_k(t)$  are time-dependent control parameters,  $K$  is the total number of them, and all  $\mathcal{L}_k$  are constant. The unitary dynamics corresponds to the case of  $\mathcal{G} = U$ ,  $\mathcal{L} = -i\mathcal{H}$ . The master equation in Lindblad form (3.24) is equivalent to equation (5.1) with the following parameters [80]:

$$\begin{aligned} \mathcal{L}(t) &= -i\mathcal{H}(t) + \Gamma, & \mathcal{H}(t) &= \mathbb{1}_{2^N} \otimes \mathcal{H}(t) - \mathcal{H}^\top(t) \otimes \mathbb{1}_{2^N} \\ \Gamma &= \sum_{\alpha=1}^3 \sum_{j=1}^N 2L_{\alpha,j}^* \otimes L_{\alpha,j} - \left( \mathbb{1}_{2^N} \otimes L_{\alpha,j}^\dagger L_{\alpha,j} + L_{\alpha,j}^\top L_{\alpha,j}^* \otimes \mathbb{1}_{2^N} \right). \end{aligned} \quad (5.3)$$

In this case, the propagator acts on a vectorized density matrix  $\mathbf{col}[\rho]$ , which is a column vector of the length  $2^{2N}$  created by stacking individual columns of  $\rho$ :

$$\mathbf{col}[\rho](t) = \mathcal{G}(t)\mathbf{col}[\rho](0). \quad (5.4)$$

The expression above stem from the following identity for the product of 3 matrices, which is easy to verify:

$$\mathbf{col}[A\rho B] = (B^\top \otimes A)\mathbf{col}[\rho]. \quad (5.5)$$

Therefore, the propagator of any dynamical spin system can be found using the same formalism for the cases of presence and absence of dissipation. The only serious bottleneck in the dissipative case is the size of the matrices being  $2^{2N} \times 2^{2N}$  instead of  $2^N \times 2^N$  in the nondissipative case (e.g.  $256 \times 256$  vs.  $16 \times 16$  for  $N = 4$ ). This can make a big difference even for relatively small numbers of electrons. Thus, it is imperative that we employ heavily optimized algorithms at the very beginning to ensure that the computational costs are manageable for larger systems.

The general solution of equation (5.1) is given by the so-called time-ordered exponential, defined as the Dyson series [91]:

$$\mathcal{G}(t) = \mathcal{T} \exp\left(\int_0^t dt_1 \mathcal{L}(t_1)\right) \equiv \mathbb{1} + \int_0^t dt_1 \mathcal{L}(t_1) + \int_0^t dt_1 \int_0^{t_1} dt_2 \mathcal{L}(t_1) \mathcal{L}(t_2) + \dots \quad (5.6)$$

This can be verified in the following way. Having integrated the expression (5.1) once, we obtain an equivalent integral equation:

$$\mathcal{G}(t) = \mathbb{1} + \int_0^t dt_1 \mathcal{G}(t_1) \mathcal{L}(t_1)$$

By substituting the operator  $\mathcal{G}$  under the integral with the whole right-hand side of the equation repetitively, one easily obtains (5.6). In case  $[\mathcal{L}(t'), \mathcal{L}(t'')] = 0$  at all times, the time-ordered exponential simplifies to an ordinary matrix exponential. In the general case, this commutation relation does not hold, and the series (5.6) converges badly. Therefore, we resort to designing *piecewise constant* control pulses:

$$a_{k,m} = a_k((m-1)\Delta t \leq t < m\Delta t) = \text{const}, \quad m = 1 \dots M, \quad \Delta t = T/M, \quad (5.7)$$

$$\mathcal{L}^{[m]} = \mathcal{L}((m-1)\Delta t \leq t < m\Delta t) = \mathcal{L}_0 + \sum_{i=1}^K a_{i,m} \mathcal{L}_i, \quad (5.8)$$

where  $T$  is the duration of the pulse, and  $M$  is the total number of steps (user-defined). Hereinafter, the upper index in square brackets  $^{[m]}$  denotes the value of a time-dependent operator at the  $m^{\text{th}}$  time step. The solution in each segment is given by a simple matrix exponential, thus expression for the propagator reads as follows:

$$\begin{aligned} \mathcal{G}(T) &= \prod_{m=1}^M \exp\left(\int_{(m-1)\Delta t}^{m\Delta t} dt_1 \mathcal{L}(t_1)\right) = \\ &= \prod_{m=1}^M \exp\left[\left(\mathcal{L}_0 + \sum_{k=1}^K a_{k,m} \mathcal{L}_k\right) \Delta t\right] = \prod_{m=1}^M \exp(\mathcal{L}^{[m]} \Delta t), \quad (5.9) \end{aligned}$$

where the operators are conventionally multiplied in the reverse order:  $\prod_i A_i = \dots A_3 A_2 A_1$ .

## 5.2.2 Toggling frame

Suppose that there are two distinct physical mechanisms that contribute to the evolution of the system. This corresponds to a generator of the form:

$$\mathcal{L}_{\text{total}}(t) = \mathcal{L}'(t) + \mathcal{L}''(t)$$

Clearly, when  $\mathcal{L}'$  and  $\mathcal{L}''$  do not commute at all times (which is most often the case), the system propagator does not factor into the product of propagators under two individual generators. Nonetheless, there is an important theorem in control theory which shows how to partly separate the effects of individual evolutions. The decomposition is universal and especially valuable when  $\mathcal{L}'$  is under full experimental control, and  $\mathcal{L}''$  corresponds to the unwanted interactions or effects to be minimized.

We say that  $\mathcal{G}'(t)$  is the propagator under  $\mathcal{L}'(t)$  alone:

$$\mathcal{G}'(t) = \mathcal{T} \exp\left(\int_0^t dt_1 \mathcal{L}'(t_1)\right), \quad (5.10)$$

whereas the propagator under  $\mathcal{L}_{\text{total}}(t)$  is

$$\mathcal{G}_{\text{total}}(t) = \mathcal{T} \exp\left(\int_0^t dt_1 (\mathcal{L}'(t_1) + \mathcal{L}''(t_1))\right) \quad (5.11)$$

It turns out that:

$$\mathcal{G}_{\text{total}}(t) = \mathcal{G}'(t) \mathcal{G}_{\text{tog}}(t), \quad (5.12)$$

where  $\mathcal{G}_{\text{tog}}$  is the so-called *toggling frame propagator* under the generator  $\widetilde{\mathcal{L}}''$ :

$$\mathcal{G}_{\text{tog}}(t) = \mathcal{T} \exp\left(\int_0^t dt_1 \widetilde{\mathcal{L}}''(t_1)\right), \quad \widetilde{\mathcal{L}}''(t) = \mathcal{G}'^{-1}(t) \mathcal{L}''(t) \mathcal{G}'(t) \quad (5.13)$$

To prove this, we differentiate the right hand side of equation (5.12):

$$\begin{aligned} \frac{d}{dt} (\mathcal{G}'(t) \mathcal{G}_{\text{tog}}(t)) &= \dot{\mathcal{G}}'(t) \mathcal{G}_{\text{tog}}(t) + \mathcal{G}'(t) \dot{\mathcal{G}}_{\text{tog}}(t) = \mathcal{L}'(t) \mathcal{G}'(t) \mathcal{G}_{\text{tog}}(t) + \mathcal{G}'(t) \widetilde{\mathcal{L}}''(t) \mathcal{G}_{\text{tog}}(t) = \\ &= (\mathcal{L}'(t) + \mathcal{L}''(t)) (\mathcal{G}'(t) \mathcal{G}_{\text{tog}}(t)) = \mathcal{L}_{\text{total}}(t) \mathcal{G}_{\text{total}}(t) = \frac{d}{dt} \mathcal{G}_{\text{total}}(t), \end{aligned} \quad (5.14)$$

and obtain the equality of derivatives of both sides. Since the equality (5.12) obviously holds at  $t = 0$ , this concludes the proof that it holds at all times as well.



Although we have not fully separated the dynamics under  $\mathcal{L}'$  from the rest due to the intrinsic dependency of the toggling frame generator  $\widetilde{\mathcal{L}}''$  on  $\mathcal{G}$ , we can try to estimate the effect of  $\mathcal{L}'$  up to different orders. To do this, we expand  $\mathcal{G}_{\text{tog}}(t)$  in (5.12) into the Dyson series (5.6):

$$\mathcal{G}_{\text{total}}(t) = \mathcal{G}'(t) + \mathcal{G}'(t) \int_0^t dt_1 \widetilde{\mathcal{L}}''(t_1) + \mathcal{G}'(t) \int_0^t dt_1 \int_0^{t_1} dt_2 \widetilde{\mathcal{L}}''(t_1) \widetilde{\mathcal{L}}''(t_2) + \dots \quad (5.15)$$

The role of the terms of different orders will be addressed further on.

### 5.2.3 Directional derivatives

Gradient-based optimization methods essentially rely on the evaluation of the derivatives of the function to be optimized. Apart from the partial derivative with respect to a scalar, the derivative along the direction of an operator  $R$  may be of interest. For some functional or superoperator  $F[\mathcal{L}]$ , we define it in the following way:

$$\mathcal{D}_R F[\mathcal{L}] = \left. \frac{d}{d\epsilon} \right|_{\epsilon=0} F[\mathcal{L} + \epsilon R]$$

Clearly, if we put  $\mathcal{L}' = \mathcal{L}$ ,  $\mathcal{L}'' = \epsilon R$  in the expansion (5.15), we will obtain a series in powers of a small parameter  $\epsilon$ . From this, we immediately obtain the directional derivative of a time-ordered exponential (5.6) (the term coupled to  $\epsilon^1$ ):

$$\begin{aligned} \mathcal{D}_R \mathcal{G}(t) \equiv \frac{\mathcal{D}\mathcal{G}}{\mathcal{D}R}(t) &= \left. \frac{d}{d\epsilon} \right|_{\epsilon=0} \mathcal{T} \exp \left\{ \int_0^t dt_1 [\mathcal{L}(t_1) + \epsilon R(t_1)] \right\} = \\ & \mathcal{G}(t) \int_0^t dt_1 \mathcal{G}^{-1}(t_1) R(t_1) \mathcal{G}(t_1). \end{aligned} \quad (5.16)$$

This expression shows how susceptible (to a first order) the cumulative system evolution is to the interactions represented by  $R$ . The formulas for higher-order derivatives can be derived in the same manner, for example:

$$\mathcal{D}_{R,R}^2 \mathcal{G}(t) \equiv \frac{\mathcal{D}^2 \mathcal{G}}{\mathcal{D}R^2}(t) = 2\mathcal{G}(t) \int_0^t dt_1 \int_0^{t_1} dt_2 \mathcal{G}^{-1}(t_1) R(t_1) \mathcal{G}(t_1) \mathcal{G}^{-1}(t_2) R(t_2) \mathcal{G}(t_2) \quad (5.17)$$

$$\begin{aligned} \frac{\mathcal{D}^2 \mathcal{G}}{\mathcal{D}R \mathcal{D}Q}(t) &= \mathcal{G}(t) \int_0^t dt_1 \int_0^{t_1} dt_2 \mathcal{G}^{-1}(t_1) R(t_1) \mathcal{G}(t_1) \mathcal{G}^{-1}(t_2) Q(t_2) \mathcal{G}(t_2) + \\ & \mathcal{G}(t) \int_0^t dt_1 \int_0^{t_1} dt_2 \mathcal{G}^{-1}(t_1) Q(t_1) \mathcal{G}(t_1) \mathcal{G}^{-1}(t_2) R(t_2) \mathcal{G}(t_2) \end{aligned} \quad (5.18)$$

As our control problem (5.2) is bilinear (i.e. linear with respect to each control parameter  $a_k(t)$ ), we can write the derivative with respect to  $a_k(t)$  in terms of a directional derivative:

$$\begin{aligned} \frac{\partial \mathcal{G}}{\partial a_k}(t) &= \frac{\partial}{\partial a_k} \mathcal{T} \exp \left\{ \int_0^t dt_1 \mathcal{L}_0 + \sum_{l=1}^K a_l(t_1) \mathcal{L}_l \right\} = \\ &= \left. \frac{\partial}{\partial \epsilon} \right|_{\epsilon=0} \mathcal{T} \exp \left\{ \int_0^t dt_1 \left[ \mathcal{L}_0 + \epsilon \mathcal{L}_k + \sum_{l=1}^K a_l(t_1) \mathcal{L}_l \right] \right\} = \frac{\mathcal{D} \mathcal{G}}{\mathcal{D} \mathcal{L}_k}(t) \end{aligned} \quad (5.19)$$

This expression can be simplified further in the case of a discretized pulse (5.9), as all variables  $a_{k,m}$  are independent of each other:

$$\frac{\partial \mathcal{G}(T)}{\partial a_{k,m}} = \pi_m^+[\mathcal{L}] \Upsilon_m[\mathcal{L}, \mathcal{L}_k] \pi_m^-[\mathcal{L}], \quad k = 1, \dots, K, \quad m = 1, \dots, M \quad (5.20a)$$

$$\pi_m^+[\mathcal{L}] = \prod_{j=m+1}^M \exp(\mathcal{L}^{[j]} \Delta t), \quad \pi_m^-[\mathcal{L}] = \prod_{j=1}^{m-1} \exp(\mathcal{L}^{[j]} \Delta t), \quad \pi_M^+ = \pi_1^- = \mathbb{1} \quad (5.20b)$$

$$\begin{aligned} \Upsilon_m[\mathcal{L}, \mathcal{L}_k] &= \frac{\partial}{\partial a_{k,m}} \exp \left[ \left( \mathcal{L}_0 + \sum_{i=1}^K a_{i,m} \mathcal{L}_i \right) \Delta t \right] = \frac{\mathcal{D}}{\mathcal{D} \mathcal{L}_k} \exp(\mathcal{L}^{[m]} \Delta t) = \\ &= \exp(\mathcal{L}^{[m]} \Delta t) \int_0^{\Delta t} dt \exp(-\mathcal{L}^{[m]} t) \mathcal{L}_k \exp(\mathcal{L}^{[m]} t). \end{aligned} \quad (5.20c)$$

As a reminder, the index  $k$  denotes the control parameter, and  $m$  is the number of the time step. The superoperators  $\pi_m^+, \pi_m^-$ , defined in equation (5.20b), are known as the forward and backward propagators, respectively. Importantly, they do not depend on  $k$  and can be updated recursively at each increment of  $m$ :

$$\pi_{m+1}^+[\mathcal{L}] = \pi_m^+[\mathcal{L}] \exp(-\mathcal{L}^{[m+1]} \Delta t), \quad \pi_{m+1}^-[\mathcal{L}] = \exp(\mathcal{L}^{[m]} \Delta t) \pi_m^-[\mathcal{L}], \quad (5.21)$$

This method is very memory efficient since it involves only one matrix multiplication at each update.

## 5.2.4 Van Loan method

Formulas (5.16), (5.19) and (5.20c) show that we need an efficient algorithm to evaluate integrals of such type:  $\int [\mathcal{T} \exp(\bullet)]^{-1} K \mathcal{T} \exp(\bullet)$  – in order to find a derivative. The

method developed by Van Loan shows that such integrals naturally appear in the solutions of linear differential equations for larger block matrices [91, 92]. Precisely, the solution to the following block matrix equation:

$$\frac{d}{dt} \begin{pmatrix} C_{11}(t) & C_{12}(t) \\ 0 & C_{22}(t) \end{pmatrix} = \begin{pmatrix} \mathcal{L}(t) & R(t) \\ 0 & \mathcal{L}(t) \end{pmatrix} \begin{pmatrix} C_{11}(t) & C_{12}(t) \\ 0 & C_{22}(t) \end{pmatrix}, \quad C_{11}(0) = C_{12}(0) = C_{22}(0) = \mathbb{1}, \quad (5.22)$$

is given by:

$$\begin{pmatrix} C_{11}(t) & C_{12}(t) \\ 0 & C_{22}(t) \end{pmatrix} \equiv \mathcal{T} \exp \left[ \int_0^t dt_1 \begin{pmatrix} \mathcal{L}(t_1) & R(t_1) \\ 0 & \mathcal{L}(t_1) \end{pmatrix} \right] = \begin{pmatrix} \mathcal{G}(t) & \mathcal{D}_R \mathcal{G}(t) \\ 0 & \mathcal{G}(t) \end{pmatrix}. \quad (5.23)$$

Remarkably, the equalities with higher-order directional derivatives, analogous to (5.17) and (5.18), also hold, e.g.:

$$\mathcal{T} \exp \left[ \int_0^t dt_1 \begin{pmatrix} \mathcal{L}(t_1) & R(t_1) & 0 \\ 0 & \mathcal{L}(t_1) & Q(t_1) \\ 0 & 0 & \mathcal{L}(t_1) \end{pmatrix} \right] = \begin{pmatrix} \mathcal{G}(t) & \mathcal{D}_R \mathcal{G}(t) & \mathcal{D}_{R,Q}^2 \mathcal{G}(t) \\ 0 & \mathcal{G}(t) & \mathcal{D}_Q \mathcal{G}(t) \\ 0 & 0 & \mathcal{G}(t) \end{pmatrix}. \quad (5.24)$$

The time-ordered exponential substantially simplifies in the case of constant matrices and gives the way to evaluate  $\Upsilon_m[\mathcal{L}, \mathcal{L}_k]$  from (5.20c), which depends only on the values at the  $m^{\text{th}}$  time step:

$$\begin{pmatrix} \exp(\mathcal{L}^{[m]} \Delta t) & \Upsilon_m[\mathcal{L}, \mathcal{L}_k] \\ 0 & \exp(\mathcal{L}^{[m]} \Delta t) \end{pmatrix} = \exp \left[ \begin{pmatrix} \mathcal{L}^{[m]} & \mathcal{L}_k \\ 0 & \mathcal{L}^{[m]} \end{pmatrix} \Delta t \right] \quad (5.25)$$

This result shows that for a partial derivative with respect to a scalar, one needs to exponentiate only one block matrix of the size  $2 \dim(\mathcal{L}) \times 2 \dim(\mathcal{L})$ , and take its top right slice (highlighted). The situation is different for a directional derivative with respect to an operator  $R$  that affects the system evolution *at all times*, whether  $R$  is time-dependent or not. We can obtain a formula for it from the fact that the solution to equation (5.22) in the piecewise constant case can be written as a product of matrix exponentials, by analogy to (5.9):

$$\begin{pmatrix} C_{11}(t) & C_{12}(t) \\ 0 & C_{22}(t) \end{pmatrix} = \begin{pmatrix} \mathcal{G}(t) & \mathcal{D}_R \mathcal{G}(t) \\ 0 & \mathcal{G}(t) \end{pmatrix} = \prod_{m=1}^M \exp \left[ \begin{pmatrix} \mathcal{L}^{[m]} & R^{[m]} \\ 0 & \mathcal{L}^{[m]} \end{pmatrix} \Delta t \right] \quad (5.26)$$

This brings us to the conclusion that the evaluation of a directional derivative with respect to an operator requires the evaluation of  $M$  matrix exponentials of the size  $2 \dim(\mathcal{L}) \times$

2  $\dim(\mathcal{L})$ , and their multiplication. As before, the desired derivative is given by the upper right quadrant of the obtained matrix.

What about the mixed derivative of this type:  $\frac{\partial}{\partial a_{k,m}} \mathcal{D}_R \mathcal{G}(t)$ ? The answer comes from the differentiation of both sides of equation (5.26) (consider the case of time-independent  $R$  for simplicity):

$$\begin{aligned} \begin{pmatrix} \frac{\partial \mathcal{G}(t)}{\partial a_{k,m}} & \frac{\partial}{\partial a_{k,m}} \mathcal{D}_R \mathcal{G}(t) \\ 0 & \frac{\partial \mathcal{G}(t)}{\partial a_{k,m}} \end{pmatrix} &= \frac{\partial}{\partial a_{k,m}} \prod_{j=1}^M \exp \left[ \begin{pmatrix} \mathcal{L}_0 + \sum_{i=1}^K a_{i,j} \mathcal{L}_i & R \\ 0 & \mathcal{L}_0 + \sum_{i=1}^K a_{i,j} \mathcal{L}_i \end{pmatrix} \Delta t \right] = \\ &= \frac{\partial}{\partial a_{k,m}} \prod_{j=1}^M \exp \left[ \begin{pmatrix} \mathcal{L}'_0 + \sum_{i=1}^K a_{i,j} \mathcal{L}'_i \\ 0 \end{pmatrix} \Delta t \right], \\ &\text{where } \mathcal{L}'_0 = \mathbb{1}_2 \otimes \mathcal{L}_0 + \begin{pmatrix} 0 & 1 \\ 0 & 0 \end{pmatrix} \otimes R, \mathcal{L}'_i = \mathbb{1}_2 \otimes \mathcal{L}_i \quad (5.27) \end{aligned}$$

We already have formula (5.20) that gives the derivative of an analogous product of matrix exponentials. This means we can directly use it for the “effective” Liouville operator  $\mathcal{L}'(t) = \mathcal{L}'_0 + \sum_{i=1}^K a_i(t) \mathcal{L}'_i$ :

$$\begin{pmatrix} \frac{\partial \mathcal{G}(t)}{\partial a_{k,m}} & \frac{\partial}{\partial a_{k,m}} \mathcal{D}_R \mathcal{G}(t) \\ 0 & \frac{\partial \mathcal{G}(t)}{\partial a_{k,m}} \end{pmatrix} = \pi_m^+ [\mathcal{L}'] \Upsilon_m [\mathcal{L}', \mathcal{L}'_k] \pi_m^- [\mathcal{L}'], \quad (5.28a)$$

$$\begin{aligned} \pi_m^+ [\mathcal{L}'] &= \prod_{j=m+1}^M \exp \left[ \begin{pmatrix} \mathcal{L}^{[j]} & R \\ 0 & \mathcal{L}^{[j]} \end{pmatrix} \Delta t \right], \quad \pi_m^- [\mathcal{L}'] = \prod_{j=1}^{m-1} \exp \left[ \begin{pmatrix} \mathcal{L}^{[j]} & R \\ 0 & \mathcal{L}^{[j]} \end{pmatrix} \Delta t \right], \\ &\pi_M^+ = \pi_1^- = \mathbb{1}, \end{aligned} \quad (5.28b)$$

$$\begin{pmatrix} \exp(\mathcal{L}'^{[m]} \Delta t) & \Upsilon_m [\mathcal{L}', \mathcal{L}'_k] \\ 0 & \exp(\mathcal{L}'^{[m]} \Delta t) \end{pmatrix} = \prod_{m=1}^M \exp \left[ \begin{pmatrix} \mathcal{L}^{[m]} & R & \mathcal{L}_k & 0 \\ 0 & \mathcal{L}^{[m]} & 0 & \mathcal{L}_k \\ 0 & 0 & \mathcal{L}^{[m]} & R \\ 0 & 0 & 0 & \mathcal{L}^{[m]} \end{pmatrix} \Delta t \right] \quad (5.28c)$$

In this case, the matrix slices should be extracted taken two times (highlighted with red and yellow). The rules of updating the backward and forward propagators remain the same as before.

## 5.3 Control problem formulation for gradient minimization

### 5.3.1 Spin dynamics: generalization to a nonlinear problem

The problem we need to solve — find optimal voltage and field sequences for the quantum control of electron spins — is clearly not bilinear. Indeed, such control parameters as deviation  $g$ -factors and exchange coefficients depend nontrivially on the experimentally controlled gate voltages. As before, we denote the plunger gate voltages as  $V_i$ ,  $i = 1, \dots, N$ , and the tunnel gate voltages as  $W_j$ ,  $j = 1, \dots, N - 1$ . Consider the nondissipative case first. We can rewrite the Liouville evolution generator as follows:

$$\mathcal{L}(t) = \mathcal{L}_0 + \sum_{k=1}^K a_k (\{b_s(t)\}_k) \mathcal{L}_k, \quad \{b_s(t)\} = \bigcup_{k=1}^K \{b_s(t)\}_k \quad (5.29)$$

where  $\{b_s\}_k$  is the set of experimentally controlled parameters which determine the value of  $a_k$ , and  $\{b_s\}$  is the set of all such parameters. The coefficients and generator components are deduced from the system spin Hamiltonian (3.23) and are summarized in table 5.1.

Index $k$	$a_k$	$\mathcal{L}_k$	$\{b_k\}$ elements
0	—	$\sum_{j=1}^N \frac{i}{2} (\omega - \omega_{\text{RF}}) Z_j$	—
$1 \dots N$	$\delta g_k$	$\frac{i\omega}{4} Z_k$	$V_k, W_{k-1}, W_k$
$N + 1, \dots, 2N - 1$	$J_{k-N}$	$\frac{i}{4\hbar} \vec{\sigma}_{k-N} \cdot \vec{\sigma}_{k+1-N}$	$V_{k-N}, V_{k+1-N}, W_{k-N}$
$2N$	$B_{\text{RF}} \cos \phi$	$i \frac{2\mu_B}{\hbar} \sum_{j=1}^N X_j$	$B_{\text{RF}}, \phi$
$2N + 1$	$B_{\text{RF}} \sin \phi$	$i \frac{2\mu_B}{\hbar} \sum_{j=1}^N Y_j$	$B_{\text{RF}}, \phi$

Table 5.1: Components of the spin evolution generator. If higher precision is required, influence of all voltages on  $\delta g_k$ ,  $J_k$  can be taken into account.

Index $s$	$b_s$	$\frac{\partial}{\partial b_{s,m}}$
$1 \dots N$	$V_s$	$\left(\frac{\partial g_s}{\partial V_s}\right)_m \frac{\partial}{\partial a_{s,m}} + \left(\frac{\partial J_{s,s+1}}{\partial V_s}\right)_m \frac{\partial}{\partial a_{N+s,m}} + \left(\frac{\partial J_{s-1,s}}{\partial V_s}\right)_m \frac{\partial}{\partial a_{N+s-1,m}}$
$N+1, \dots, 2N-1$	$W_{s-N}$	$\left(\frac{\partial g_{s-N}}{\partial V_{s-N}}\right)_m \frac{\partial}{\partial a_{s-N,m}} + \left(\frac{\partial g_{s+1-N}}{\partial V_{s+1-N}}\right)_m \frac{\partial}{\partial a_{s+1-N,m}} + \left(\frac{\partial J_{s-N,s+1-N}}{\partial W_{s-N}}\right)_m \frac{\partial}{\partial a_{s,m}}$
$2N$	$B_{\text{RF}}$	$\cos \phi_m \frac{\partial}{\partial a_{2N,m}} + \sin \phi_m \frac{\partial}{\partial a_{2N+1,m}}$
$2N+1$	$\phi$	$-\frac{\sin \phi_m}{B_{\text{RF},m}} \frac{\partial}{\partial a_{2N,m}} + \frac{\cos \phi_m}{B_{\text{RF},m}} \frac{\partial}{\partial a_{2N+1,m}}$

Table 5.2: Derivatives with respect to the control parameters of a nonlinear spin dynamics control problem.

Here, we make a reasonable approximation that each control parameter is dependent only on the voltages of the three closest gates. However, the approximation can be lifted if needed to achieve higher precision. In total, there are  $K = 2N + 1$  distinct variables  $a_k$ , and  $2N + 1$  physically controlled quantities:  $V_i, W_i, B_{\text{RF}}, \phi$ . Gradient optimization methods require the derivative information about the latter. Thus, we need to express all derivatives with respect to voltages, field magnitude and phase at the  $m^{\text{th}}$  time step in terms of  $\frac{\partial}{\partial a_{k,m}}$ . This will enable us to utilize the formalism developed earlier, since  $\mathcal{L}(t)$  is bilinear with respect to  $\{a_k(t)\}$ . In this work, we do not aim at the GRAPE implementations which incorporate the second derivatives but rather stick to the quasi-Newton BFGS algorithm [85] that estimates the system Hessian matrix based on the gradient history. Therefore, we derive the expressions only for the first derivatives.

The summary of the results is presented in table 5.2. The coefficients in the last two entries correspond to a Jacobian matrix of polar coordinates in a Cartesian system:

$$\frac{\partial(r, \phi)}{\partial(x, y)} = \left(\frac{\partial(x, y)}{\partial(r, \phi)}\right)^{-1} = \begin{pmatrix} \cos \phi & -r \sin \phi \\ \sin \phi & r \cos \phi \end{pmatrix}^{-1} = \begin{pmatrix} \cos \phi & \sin \phi \\ -\frac{\sin \phi}{r} & \frac{\cos \phi}{r} \end{pmatrix}$$

As before, we can transition from the nondissipative to the dissipative case with the substitutions:

$$\textcircled{1} \quad \mathcal{L}_k \rightarrow \mathbb{1}_{2^N} \otimes \mathcal{L}_k - \mathcal{L}_k^T \otimes \mathbb{1}_{2^N}, \quad \textcircled{2} \quad \mathcal{L} \rightarrow \mathcal{L} + \Gamma. \quad (5.30)$$

Also, for simplicity, we will keep only the dephasing Lindblad terms for further derivations, i.e.  $\alpha = 3$  in formulas (3.25). First of all, only this contribution to non-unitarity is "avoidable", and secondly, it affects the system on much shorter timescales than spin relaxation (usually,  $T_2 \ll T_1$ ). Thus, the expression for  $\Gamma$  from (5.3) simplifies to the following:

$$\Gamma = \frac{1}{2T_2} \sum_{j=1}^N (Z_j \otimes Z_j - \mathbb{1}_{2^{2N}}) \quad (5.31)$$

### 5.3.2 Expression for the cost function

As before, the problem to be solved with the gradient descent method is formulated as a scalar cost function minimization. Unlike in chapter 4, the cost function can include more terms now — GRAPE allows to directly control more quantities:

$$f = w_F f_F + w_\Gamma f_\Gamma + w_{CS} f_{CS} + w_{BF} f_{BF} + w_{VW} f_{VW}, \quad \sum_i w_i = 1. \quad (5.32)$$

The last three terms have the same meaning as discussed in section 4.2: charge stability preservation, restrictions on the electromagnetic energy losses and voltage sweep rates. The corresponding expressions for cost function contributions (4.26), (4.29), and (4.31), still apply but in a discretized form (integrals are replaced with sums  $\int \rightarrow \sum_m \Delta t$ , and time derivatives with the finite difference formulas).

The role of the first two terms is maximizing the quantum operation fidelity and the reduction of system susceptibility to decoherence, respectively. The corresponding expressions are derived in the next two subsections. Although not discussed here, it is also possible in principle to design pulses robust to noise using the same cost function formalism. The examples of noise incorporation for a linear control problem can be found in [91].

### 5.3.3 Maximizing fidelity

Suppose the unitary operator  $U_0(t)$  corresponds to a desired system evolution. In the ideal case, there is obviously no decoherence, and the density matrix evolution dynamics can be expressed in one of the two equivalent forms:

$$\rho(t) = U_0(t)\rho(0)U_0^\dagger(t), \quad \mathbf{col}[\rho](t) = U_0^* \otimes U_0 \mathbf{col}[\rho](0). \quad (5.33)$$

We introduce the following general notation for unitary operators:

$$\mathcal{U}_\perp = \begin{cases} U_\perp, & \text{nondissipative case,} \\ U_\perp^* \otimes U_\perp, & \text{dissipative case,} \end{cases} \quad (5.34)$$

where the index “0” corresponds to the desired quantum operation, and no index refers to the actual system evolution:

$$\mathcal{L} = -i\mathcal{H} + \Gamma, \quad U(t) = \mathcal{T} \exp\left(-i \int_0^t dt_1 \mathcal{H}(t_1)\right) \quad (5.35)$$

We define the infidelity of a quantum operation in the following way:

$$f_{\text{F}} = 1 - \frac{1}{\dim \mathcal{G}} |\langle \mathcal{G}(T), \mathcal{U}_0(T) \rangle| = 1 - \frac{1}{\dim \mathcal{G}} \sqrt{\text{tr} [\mathcal{G}(T) \mathcal{U}_0^\dagger(T)] \text{tr} [\mathcal{G}^\dagger(T) \mathcal{U}_0(T)]}, \quad (5.36)$$

where  $\langle \cdot, \cdot \rangle$  denotes a Frobenius inner product:  $\langle A, B \rangle = \text{tr} A^\dagger B$ ;  $\dim \mathcal{G} = 2^N$  in the nondissipative case, and is  $2^{2N}$  otherwise. The corresponding Frobenius norm is denoted as  $\|A\| = \sqrt{\langle A, A \rangle} = \sqrt{\text{tr} A^\dagger A}$ . It immediately follows from Cauchy-Schwarz inequality that

$$0 \leq \left( \frac{1}{\dim \mathcal{G}} |\langle \mathcal{G}(T), \mathcal{U}_0(T) \rangle| \right)^2 \leq \frac{\text{tr} [\mathcal{G}^\dagger(T) \mathcal{G}(T)]}{\dim \mathcal{G}} \cdot \underbrace{\frac{\text{tr} [\mathcal{U}^\dagger(T) \mathcal{U}(T)]}{\dim \mathcal{U}}}_{\equiv 1} \leq 1. \quad (5.37)$$

The right-hand side of this inequality obviously holds in the nondissipative case, when the propagator  $\mathcal{G} \equiv \mathcal{U}$  is unitary. Let us now prove it in the dissipative case. As is well known [93], any density matrix transformation is a completely positive trace-preserving map and thus can be written in the Kraus form:

$$\tilde{\rho} = \sum_l S_l \rho S_l^\dagger, \quad \sum_l S_l^\dagger S_l = \mathbb{1}_{2N} \quad (5.38)$$



for some set of Kraus operators  $S_l$  (their actual expressions for are unimportant). If we vectorize equation (5.38) according to identity (5.5), we can express the system propagator in the following way:

$$\mathcal{G}(t) = \sum_l S_l^*(t) \otimes S_l(t). \quad (5.39)$$

From this we derive:

$$\begin{aligned} \text{tr} [\mathcal{G}^\dagger \mathcal{G}] &= \text{tr} \left[ \sum_{l,q} (S_l^* \otimes S_l)^\dagger S_q^* \otimes S_q \right] = \sum_{l,q} \left( \text{tr} S_l^\dagger S_q \right)^* \text{tr} S_l^\dagger S_q \\ &= \sum_{l,q} |\langle S_l, S_q \rangle|^2 \leq \sum_{l,q} \|S_l\|^2 \|S_q\|^2 = \text{tr} \left[ \sum_l S_l^\dagger S_l \right] \cdot \text{tr} \left[ \sum_q S_q^\dagger S_q \right] = (2^N)^2 = \dim \mathcal{G}. \end{aligned}$$

Thus, the inequality (5.37) holds at all  $T$ , which justifies the choice of the infidelity cost function (5.36). Its derivatives with respect to the control variables:

$$\begin{aligned} \frac{\partial f_{\text{F}}}{\partial a_{k,m}} &= -\frac{1}{\dim \mathcal{G}} \frac{\text{tr} \left[ \frac{\partial \mathcal{G}(T)}{\partial a_{k,m}} \mathcal{U}^\dagger(T) \right] \text{tr} [\mathcal{G}^\dagger(T) \mathcal{U}_0(T)] + \text{tr} [\mathcal{G}(T) \mathcal{U}^\dagger(T)] \text{tr} \left[ \frac{\partial \mathcal{G}^\dagger(T)}{\partial a_{k,m}} \mathcal{U}_0(T) \right]}{2 \sqrt{\text{tr} [\mathcal{G}(T) \mathcal{U}^\dagger(T)] \text{tr} [\mathcal{G}^\dagger(T) \mathcal{U}_0(T)]}} \\ &= \frac{1}{\dim \mathcal{G} \sqrt{\text{tr} [\mathcal{G}(T) \mathcal{U}^\dagger(T)] \text{tr} [\mathcal{G}^\dagger(T) \mathcal{U}_0(T)]}} \text{Re} \left\{ \text{tr} \left[ \frac{\partial \mathcal{G}(T)}{\partial a_{k,m}} \mathcal{U}^\dagger(T) \right] \text{tr} [\mathcal{G}^\dagger(T) \mathcal{U}_0(T)] \right\}, \end{aligned} \quad (5.40)$$

and  $\frac{\partial \mathcal{G}(T)}{\partial a_{k,m}}$  is given by formula (5.20).

### 5.3.4 Lowering susceptibility to decoherence

This cost function contribution is obviously defined only in dissipative case and is given by the following expression:

$$f_{\Gamma} = \frac{\|\mathcal{D}_{\Gamma} \mathcal{U}(T)\|}{\max_{a(t)} \|\mathcal{D}_{\Gamma} \mathcal{U}(T)\|} \quad (5.41)$$

The motivation for this choice of cost function is the following. If we put  $\mathcal{L}' = -i\mathcal{H}$ ,  $\mathcal{L}'' = \Gamma$  in formula (5.15), we get an expansion:

$$\mathcal{G}(t) = \mathcal{U}(t) + \mathcal{D}_{\Gamma} \mathcal{U}(t) + \mathcal{D}_{\Gamma, \Gamma}^2 \mathcal{U}(t) + \dots \quad (5.42)$$

From here, we see that the term  $\mathcal{D}_\Gamma \mathcal{U}(t)$  is the leading term in the perturbation of the unitary operator. Consequently, if we minimize its norm, we will maximize the system robustness to decoherence in the 1<sup>st</sup> order. The directional derivative with respect to any operator  $A$  satisfies the following inequality:

$$\begin{aligned} \|\mathcal{D}_A \mathcal{U}(T)\| &= \left\| \mathcal{U}(T) \int_0^T dt_1 \mathcal{U}^\dagger(t_1) A(t_1) \mathcal{U}(t_1) \right\| = \left\| \int_0^T dt_1 \mathcal{U}^\dagger(t_1) A(t_1) \mathcal{U}(t_1) \right\| \leq \\ & \int_0^T dt_1 \|\mathcal{U}^\dagger(t_1) A(t_1) \mathcal{U}(t_1)\| = \int_0^T dt_1 \|A(t_1)\|, \end{aligned} \quad (5.43)$$

where we used the fact that the Frobenius norm of a matrix does not change when a unitary acts on it (this immediately follows from the definition of the norm). In case of a time independent operator  $A$ , the maximum simplifies to  $\|A\| T$ . Using expressions (5.31) and (5.43), we derive the upper bound on the directional derivative with respect to  $\Gamma$ :

$$\begin{aligned} \max_{a(t)} \|\mathcal{D}_\Gamma \mathcal{U}(T)\| &= \frac{T}{2T_2} \sqrt{\text{tr} \left( \sum_{j=1}^N Z_j \otimes Z_j - \mathbb{1}_{2^{2N}} \right)^2} = \\ & \frac{T}{2T_2} \sqrt{\text{tr} \left[ \sum_{j,l=1}^N Z_j Z_l \otimes Z_j Z_l + \mathbb{1}_{2^{2N}} \right]} = \\ & \frac{T}{2T_2} \sqrt{\sum_{j,l=1}^N 2^{2N} \delta_{jl} + 2^{2N}} = \frac{T}{T_2} 2^{N-1} \sqrt{N^2 + N}, \end{aligned} \quad (5.44)$$

and obtain the final expression for the cost function contribution due to decoherence:

$$f_\Gamma = \frac{T_2}{2^{N-1} T \sqrt{N^2 + N}} \sqrt{\text{tr} [\mathcal{D}_\Gamma \mathcal{U}^\dagger(T) \mathcal{D}_\Gamma \mathcal{U}(T)]}. \quad (5.45)$$

Using the same method as before, we find the derivatives of  $f_\Gamma$  with respect to control parameters:

$$\frac{\partial f_\Gamma}{\partial a_{k,m}} = \frac{T_2}{2^{N-1} T \sqrt{N^2 + N}} \frac{\text{Re} \left\{ \text{tr} \left[ \frac{\partial \mathcal{D}_\Gamma \mathcal{U}(T)}{\partial a_{k,m}} \mathcal{D}_\Gamma \mathcal{U}^\dagger(T) \right] \right\}}{\sqrt{\text{tr} [\mathcal{D}_\Gamma \mathcal{U}^\dagger(T) \mathcal{D}_\Gamma \mathcal{U}(T)]}}; \quad (5.46)$$

refer to subsection 5.2.4 for the appropriate formulas for the directional and mixed derivatives of  $\mathcal{G} = \mathcal{U}$ .

## 5.4 Summary of chapter 5

In summary, a powerful gradient ascent pulse engineering (GRAPE) algorithm is adapted to the problem of voltage and ESR field pulse design in the spin qubit architecture proposed in [65]. The main results include:

1. A linear control problem for a general Liouville equation (with the incorporation of dissipation when necessary) is generalized to the case of nonlinear connection between effective parameters of the spin system and physically controlled gate voltages, ESR magnetic field amplitude and phase.
2. A nonlinear cost function minimization problem, accounting for the pulse infidelity and system susceptibility to decoherence, is rigorously defined.
3. Relevant scalar, directional and mixed derivatives needed for the second-order quasi-Newton optimization, are explicitly derived.

Due to its higher versatility, once implemented, the GRAPE algorithm is expected to further improve the shapes and timescales of the pulses designed in chapter 4.

# Chapter 6

## Conclusions and future work

In conclusion, we made a considerable progress towards the realization of semiconductor quantum computers with electron spins and Majorana fermions.

The results of chapter 2 are a significant step towards the holistic understanding of the mechanisms of epitaxial Al formation on III-V heterostructures. The first comprehensive review of the topic was presented and augmented with two new sets of results obtained experimentally. First, we demonstrated epitaxial metallization of In-rich InGaAs with a flat Al layer, and, for the first time, capping of the Al layer with As<sub>4</sub> as an alternative to its oxidation. The sharpness of metal-semiconductor interface was confirmed with cross-sectional STEM and EELS with atomic precision. Second, based on extensive in situ and ex situ investigation of capped and uncapped growths with a broad range of Al deposition rates, we identified a significant advantage of using very fast rates to substantially reduce wafer heating and improve its surface morphology up to the level of atomic smoothness.

A plethora of interesting phenomena discovered during this study will benefit from further investigation with a new, targeted series of experiments. The extensive monitoring and characterization (with STEM and EELS in particular) of the new test samples will hopefully provide enough data to establish a consistent procedure for growing epitaxially-metallized, scalable, InAs quantum well based platforms for the observation of Majorana zero modes.

In chapters 3, 4 and 5, we developed a strong algorithmic and software foundation for the simulation of a scalable spin-qubit computer architecture in silicon. The full-scale simulator is being developed as a part of QuDiPy — a general-purpose Python package for

semiconductor quantum dot simulation. The direct incorporation of realistic gate geometries to infer effective parameters of the qubit system by efficient many-electron calculations makes possible the use of the simulator in conjunction with real quantum dot devices. A very general and numerically inexpensive voltage pulse engineering algorithm for unitary operations, derived in chapter 4, goes far beyond the spin-qubit control schemes proposed previously for similar devices by featuring theoretical 100% fidelity, automatic incorporation of all interdot cross-couplings, and numerically inexpensive optimization for meeting system limitations. The chapter 5 features a novel adaptation of GRAPE to the gate and ESR voltage control problem for spin qubit manipulation. We anticipate it to further improve the performance of pulses engineered in chapter 4.

The full software realization of these algorithms (particularly, implementation of exchange two-qubit gates and cross-coupling incorporation) along with the improvement of many-body calculation method in QuDiPy are our primary near-term goals. This will enable us to demonstrate the full-scale performance of the computer simulation, interface it with the cryogenic control electronics, and experimentally realize quantum operations on real quantum dot devices.

Above all, we consider our results to be directly relevant to the development and control of hybrid topological quantum devices, which will combine advantages of spin quantum dot and Majorana qubit operations. In particular, our method of mapping potential landscapes onto effective Hubbard model is immediately applicable to any networks of Majorana islands and quantum dots in planar semiconductor heterostructures. Furthermore, the pulse engineering algorithm proposed for Si qubits can be utilized in the hybrid devices that will combine electron spin manipulation and Majorana braiding (or equivalent measurements) for quantum gate operations.

# References

- [1] Brandon Buonacorsi, Marek Korkusinski, Bohdan Khromets, and Jonathan Baugh. “Optimizing lateral quantum dot geometries for reduced exchange noise”. In: (2020).
- [2] A. T. Hatke, T. Wang, C. Thomas, G. C. Gardner, and M. J. Manfra. “Mobility in excess of  $106 \text{ cm}^2/\text{V s}$  in InAs quantum wells grown on lattice mismatched InP substrates”. In: *Applied Physics Letters* 111.14 (2017), p. 142106. DOI: [10.1063/1.4993784](https://doi.org/10.1063/1.4993784).
- [3] H. J. Suominen et al. “Zero-Energy Modes from Coalescing Andreev States in a Two-Dimensional Semiconductor-Superconductor Hybrid Platform”. In: *Phys. Rev. Lett.* 119 (17 2017), p. 176805. DOI: [10.1103/PhysRevLett.119.176805](https://doi.org/10.1103/PhysRevLett.119.176805).
- [4] R Maurand et al. “A CMOS silicon spin qubit”. In: *Nature communications* 7.1 (2016), pp. 1–6.
- [5] Irene Puerto Gimenez, Marek Korkusinski, and Pawel Hawrylak. “Linear combination of harmonic orbitals and configuration interaction method for the voltage control of exchange interaction in gated lateral quantum dot networks”. In: *Phys. Rev. B* 76 (7 2007), p. 075336. DOI: [10.1103/PhysRevB.76.075336](https://doi.org/10.1103/PhysRevB.76.075336).
- [6] Stephen Blundell. *Magnetism in condensed matter*. 2003.
- [7] Fanming Qu et al. “Quantized Conductance and Large  $g$ -Factor Anisotropy in InSb Quantum Point Contacts”. In: *Nano Letters* 16.12 (2016), 7509–7513. ISSN: 1530-6992. DOI: [10.1021/acs.nanolett.6b03297](https://doi.org/10.1021/acs.nanolett.6b03297).
- [8] Zijin Lei et al. “Electronic  $g$  factor and magnetotransport in InSb quantum wells”. In: *Phys. Rev. Research* 2 (3 2020), p. 033213. DOI: [10.1103/PhysRevResearch.2.033213](https://doi.org/10.1103/PhysRevResearch.2.033213).
- [9] A Yu Kitaev. “Unpaired Majorana fermions in quantum wires”. In: *Physics-Uspekhi* 44.10S (2001), pp. 131–136. DOI: [10.1070/1063-7869/44/10s/s29](https://doi.org/10.1070/1063-7869/44/10s/s29).

- [10] Roman M. Lutchyn, Jay D. Sau, and S. Das Sarma. “Majorana Fermions and a Topological Phase Transition in Semiconductor-Superconductor Heterostructures”. In: *Phys. Rev. Lett.* 105 (7 2010), p. 077001. DOI: [10.1103/PhysRevLett.105.077001](https://doi.org/10.1103/PhysRevLett.105.077001).
- [11] Yuval Oreg, Gil Refael, and Felix von Oppen. “Helical Liquids and Majorana Bound States in Quantum Wires”. In: *Phys. Rev. Lett.* 105 (17 2010), p. 177002. DOI: [10.1103/PhysRevLett.105.177002](https://doi.org/10.1103/PhysRevLett.105.177002).
- [12] Ramón Aguado. “Majorana quasiparticles in condensed matter”. In: *La Rivista del Nuovo Cimento* 40.11 (2017), pp. 523–593.
- [13] PM Tedrow and R Meservey. “Critical magnetic field of very thin superconducting aluminum films”. In: *Physical Review B* 25.1 (1982), p. 171.
- [14] A. D. K. Finck, D. J. Van Harlingen, P. K. Mohseni, K. Jung, and X. Li. “Anomalous Modulation of a Zero-Bias Peak in a Hybrid Nanowire-Superconductor Device”. In: *Phys. Rev. Lett.* 110 (12 2013), p. 126406. DOI: [10.1103/PhysRevLett.110.126406](https://doi.org/10.1103/PhysRevLett.110.126406).
- [15] V. Mourik et al. “Signatures of Majorana Fermions in Hybrid Superconductor-Semiconductor Nanowire Devices”. In: *Science* 336.6084 (2012), pp. 1003–1007. ISSN: 0036-8075. DOI: [10.1126/science.1222360](https://doi.org/10.1126/science.1222360).
- [16] Anindya Das et al. “Zero-bias peaks and splitting in an Al-InAs nanowire topological superconductor as a signature of Majorana fermions”. In: *Nature Physics* 8.12 (2012), pp. 887–895. ISSN: 1745-2481. DOI: [10.1038/nphys2479](https://doi.org/10.1038/nphys2479).
- [17] Fabrizio Nichele et al. “Scaling of Majorana Zero-Bias Conductance Peaks”. In: *Phys. Rev. Lett.* 119 (13 2017), p. 136803. DOI: [10.1103/PhysRevLett.119.136803](https://doi.org/10.1103/PhysRevLett.119.136803).
- [18] S. M. Albrecht et al. “Exponential protection of zero modes in Majorana islands”. In: *Nature* 531.7593 (2016), pp. 206–209. ISSN: 1476-4687. DOI: [10.1038/nature17162](https://doi.org/10.1038/nature17162).
- [19] Dominique Laroche et al. “Observation of the  $4\pi$ -periodic Josephson effect in indium arsenide nanowires”. In: *Nature Communications* 10.1 (2019), p. 245. ISSN: 2041-1723. DOI: [10.1038/s41467-018-08161-2](https://doi.org/10.1038/s41467-018-08161-2).
- [20] J. J. Sakurai and Jim Napolitano. *Modern Quantum Mechanics*. 2nd ed. Cambridge University Press, 2017. DOI: [10.1017/9781108499996](https://doi.org/10.1017/9781108499996).
- [21] M Pioro-Ladriere et al. “Electrically driven single-electron spin resonance in a slanting Zeeman field”. In: *Nature Physics* 4.10 (2008), pp. 776–779.
- [22] TF Watson et al. “A programmable two-qubit quantum processor in silicon”. In: *nature* 555.7698 (2018), pp. 633–637.

- [23] Zhenyu Cai et al. “A silicon surface code architecture resilient against leakage errors”. In: *Quantum* 3 (2019), p. 212.
- [24] Jason Alicea, Yuval Oreg, Gil Refael, Felix von Oppen, and Matthew P. A. Fisher. “Non-Abelian statistics and topological quantum information processing in 1D wire networks”. In: *Nature Physics* 7.5 (2011), pp. 412–417. ISSN: 1745-2481. DOI: [10.1038/nphys1915](https://doi.org/10.1038/nphys1915).
- [25] Martin Leijnse and Karsten Flensberg. “Quantum Information Transfer between Topological and Spin Qubit Systems”. In: *Phys. Rev. Lett.* 107 (21 2011), p. 210502. DOI: [10.1103/PhysRevLett.107.210502](https://doi.org/10.1103/PhysRevLett.107.210502).
- [26] Kaveh Gharavi, Darryl Hoving, and Jonathan Baugh. “Readout of Majorana parity states using a quantum dot”. In: *Phys. Rev. B* 94 (15 2016), p. 155417. DOI: [10.1103/PhysRevB.94.155417](https://doi.org/10.1103/PhysRevB.94.155417).
- [27] Silas Hoffman, Constantin Schrader, Jelena Klinovaja, and Daniel Loss. “Universal quantum computation with hybrid spin-Majorana qubits”. In: *Physical Review B* 94.4 (2016). ISSN: 2469-9969. DOI: [10.1103/physrevb.94.045316](https://doi.org/10.1103/physrevb.94.045316).
- [28] Torsten Karzig et al. “Scalable designs for quasiparticle-poisoning-protected topological quantum computation with Majorana zero modes”. In: *Phys. Rev. B* 95 (23 2017), p. 235305. DOI: [10.1103/PhysRevB.95.235305](https://doi.org/10.1103/PhysRevB.95.235305).
- [29] Torsten Karzig, Yuval Oreg, Gil Refael, and Michael H. Freedman. “Robust Majorana magic gates via measurements”. In: *Phys. Rev. B* 99 (14 2019), p. 144521. DOI: [10.1103/PhysRevB.99.144521](https://doi.org/10.1103/PhysRevB.99.144521).
- [30] A. Y. Cho and P. D. Dernier. “Single-crystal-aluminum Schottky-barrier diodes prepared by molecular-beam epitaxy (MBE) on GaAs”. In: *Journal of Applied Physics* 49.6 (1978), pp. 3328–3332. DOI: [10.1063/1.325286](https://doi.org/10.1063/1.325286).
- [31] Kazuyoshi Ueno, Takayoshi Yoshida, and Kazuyuki Hirose. “Epitaxial Al Schottky contacts formed on (111) GaAs”. In: *Applied Physics Letters* 56.22 (1990), pp. 2204–2206. DOI: [10.1063/1.102967](https://doi.org/10.1063/1.102967).
- [32] J Tournet et al. “Growth and characterization of epitaxial aluminum layers on gallium-arsenide substrates for superconducting quantum bits”. In: *Superconductor Science and Technology* 29.6 (2016), p. 064004. DOI: [10.1088/0953-2048/29/6/064004](https://doi.org/10.1088/0953-2048/29/6/064004).
- [34] G. Landgren, R. Ludeke, and C. Serrano. “Epitaxial Al films on GaAs(100) surfaces”. In: *Journal of Crystal Growth* 60.2 (1982), pp. 393–402. ISSN: 0022-0248. DOI: [https://doi.org/10.1016/0022-0248\(82\)90117-8](https://doi.org/10.1016/0022-0248(82)90117-8).



- [35] R. Ludeke, L. L. Chang, and L. Esaki. “Molecular beam epitaxy of alternating metal-semiconductor films”. In: *Applied Physics Letters* 23.4 (1973), pp. 201–203. DOI: [10.1063/1.1654858](https://doi.org/10.1063/1.1654858).
- [36] Wendy L. Sarney, Stefan P. Svensson, Kaushini S. Wickramasinghe, Joseph Yuan, and Javad Shabani. “Reactivity studies and structural properties of Al on compound semiconductor surfaces”. In: *Journal of Vacuum Science & Technology B* 36.6 (2018), p. 062903. DOI: [10.1116/1.5053987](https://doi.org/10.1116/1.5053987).
- [37] Kedong Zhang et al. “Interfacial modulation on single-crystalline aluminum films grown on GaAs by ErAs insertion”. In: *Journal of Vacuum Science & Technology A* 38.6 (2020), p. 060402. DOI: [10.1116/6.0000530](https://doi.org/10.1116/6.0000530).
- [38] J. Shabani et al. “Two-dimensional epitaxial superconductor-semiconductor heterostructures: A platform for topological superconducting networks”. In: *Phys. Rev. B* 93 (15 2016), p. 155402. DOI: [10.1103/PhysRevB.93.155402](https://doi.org/10.1103/PhysRevB.93.155402).
- [39] Tiantian Wang et al. “The dependence of aluminum lattice orientation on semiconductor lattice parameter in planar InAs/Al hybrid heterostructures”. In: *Journal of Crystal Growth* 535 (2020), p. 125570. ISSN: 0022-0248. DOI: <https://doi.org/10.1016/j.jcrysgro.2020.125570>.
- [40] Candice Thomas et al. “Toward durable Al-InSb hybrid heterostructures via epitaxy of 2ML interfacial InAs screening layers”. In: *Physical Review Materials* 3.12 (2019), p. 124202.
- [41] Wendy L. Sarney et al. “Aluminum metallization of III–V semiconductors for the study of proximity superconductivity”. In: *Journal of Vacuum Science & Technology B* 38.3 (2020), p. 032212. DOI: [10.1116/1.5145073](https://doi.org/10.1116/1.5145073).
- [42] Y. S. Luo, Y.-N. Yang, J. H. Weaver, L. T. Florez, and C. J. Palmstro/m. “Multiorientational growth of Al on GaAs(001) studied with scanning tunneling microscopy”. In: *Phys. Rev. B* 49 (3 1994), pp. 1893–1899. DOI: [10.1103/PhysRevB.49.1893](https://doi.org/10.1103/PhysRevB.49.1893).
- [43] Pauli Virtanen et al. “SciPy 1.0: fundamental algorithms for scientific computing in Python”. In: *Nature methods* 17.3 (2020), pp. 261–272.
- [44] Zhang Kedong. “Interfacial modulation on single-crystalline aluminum films grown on GaAs by ErAs insertion”. In: *Journal of Vacuum Science & Technology A* 38 (6 2020), p. 60402.
- [45] Shen Jian. “Real Space Surface Reconstructions of Decapped As-rich In<sub>0.53</sub>Ga<sub>0.47</sub>As (001)-(2× 4)”. In: *ECS Transactions* 16 (2008), p. 463.

- [46] Labella V. “Reflection high-energy electron diffraction and scanning tunneling microscopy study of InP (001) surface reconstructions”. In: *Journal of Vacuum Science & Technology A: Vacuum, Surfaces, and Films* 18 (2000), pp. 1492–1496.
- [47] Belk J. “Surface alloying at InAs/GaAs interfaces grown on (001) surfaces by molecular beam epitaxy”. In: *Surface science* 387 (1997), pp. 213–226.
- [48] Millunchick J and Mirecki. “Surface reconstructions of InGaAs alloys”. In: *Surface science* 550 (1-3 2004), pp. 1–7.
- [49] William Mayer et al. “Superconducting proximity effect in epitaxial Al-InAs heterostructures”. In: *Applied Physics Letters* 114.10 (2019), p. 103104. DOI: [10.1063/1.5067363](https://doi.org/10.1063/1.5067363).
- [50] Alexei M Tyryshkin et al. “Electron spin coherence exceeding seconds in high-purity silicon”. In: *Nature materials* 11.2 (2012), pp. 143–147.
- [51] Daniel Loss and David P DiVincenzo. “Quantum computation with quantum dots”. In: *Physical Review A* 57.1 (1998), p. 120.
- [52] Guido Burkard, Hans-Andreas Engel, and Daniel Loss. “Spintronics and quantum dots for quantum computing and quantum communication”. In: *Fortschritte der Physik: Progress of Physics* 48.9-11 (2000), pp. 965–986.
- [53] Jason R Petta et al. “Coherent manipulation of coupled electron spins in semiconductor quantum dots”. In: *Science* 309.5744 (2005), pp. 2180–2184.
- [54] M Veldhorst et al. “An addressable quantum dot qubit with fault-tolerant control-fidelity”. In: *Nature nanotechnology* 9.12 (2014), pp. 981–985.
- [55] Kevin Eng et al. “Isotopically enhanced triple-quantum-dot qubit”. In: *Science advances* 1.4 (2015), e1500214.
- [56] Jun Yoneda et al. “A quantum-dot spin qubit with coherence limited by charge noise and fidelity higher than 99.9%”. In: *Nature nanotechnology* 13.2 (2018), pp. 102–106.
- [57] W Huang et al. “Fidelity benchmarks for two-qubit gates in silicon”. In: *Nature* 569.7757 (2019), pp. 532–536.
- [58] Alessandro Crippa et al. “Gate-reflectometry dispersive readout and coherent control of a spin qubit in silicon”. In: *Nature communications* 10.1 (2019), pp. 1–6.
- [59] Luca Petit et al. “Universal quantum logic in hot silicon qubits”. In: *Nature* 580.7803 (2020), pp. 355–359.
- [60] Charles D Hill et al. “A surface code quantum computer in silicon”. In: *Science advances* 1.9 (2015), e1500707.

- [61] M Veldhorst, HGJ Eenink, Chih-Hwan Yang, and Andrew S Dzurak. “Silicon CMOS architecture for a spin-based quantum computer”. In: *Nature communications* 8.1 (2017), pp. 1–8.
- [62] Ruoyu Li et al. “A crossbar network for silicon quantum dot qubits”. In: *Science advances* 4.7 (2018), eaar3960.
- [63] Jelmer M Boter et al. “A sparse spin qubit array with integrated control electronics”. In: *2019 IEEE International Electron Devices Meeting (IEDM)*. IEEE. 2019, pp. 31–4.
- [64] Joe O’Gorman, Naomi H Nickerson, Philipp Ross, John JL Morton, and Simon C Benjamin. “A silicon-based surface code quantum computer”. In: *npj Quantum Information* 2.1 (2016), pp. 1–14.
- [65] Brandon Buonacorsi et al. “Network architecture for a topological quantum computer in silicon”. In: *Quantum Science and Technology* 4.2 (2019), p. 025003. DOI: [10.1088/2058-9565/aaf3c4](https://doi.org/10.1088/2058-9565/aaf3c4).
- [66] Eduardo B Ramirez, Francois Sfigakis, Sukanya Kudva, and Jonathan Baugh. “Few-electrode design for silicon MOS quantum dots”. In: *Semiconductor Science and Technology* 35.1 (2019), p. 015002.
- [67] Brandon Buonacorsi, Benjamin Shaw, and Jonathan Baugh. “Simulated coherent electron shuttling in silicon quantum dots”. In: *Phys. Rev. B* 102 (12 2020), p. 125406. DOI: [10.1103/PhysRevB.102.125406](https://doi.org/10.1103/PhysRevB.102.125406).
- [68] MF Gonzalez-Zalba, S Barraud, AJ Ferguson, and AC Betz. “Probing the limits of gate-based charge sensing”. In: *Nature communications* 6.1 (2015), pp. 1–8.
- [69] Elliot J. Connors, JJ Nelson, and John M. Nichol. “Rapid High-Fidelity Spin-State Readout in Si/Si-Ge Quantum Dots via rf Reflectometry”. In: *Phys. Rev. Applied* 13 (2 2020), p. 024019. DOI: [10.1103/PhysRevApplied.13.024019](https://doi.org/10.1103/PhysRevApplied.13.024019).
- [70] Akito Noiri et al. “Radio-Frequency-Detected Fast Charge Sensing in Undoped Silicon Quantum Dots”. In: *Nano Letters* 20.2 (2020), pp. 947–952. DOI: [10.1021/acs.nanolett.9b03847](https://doi.org/10.1021/acs.nanolett.9b03847).
- [71] Charles R Harris et al. “Array programming with NumPy”. In: *Nature* 585.7825 (2020), pp. 357–362.
- [72] Stefan Birner et al. “nextnano: General Purpose 3-D Simulations”. In: *IEEE Transactions on Electron Devices* 54.9 (2007), pp. 2137–2142. DOI: [10.1109/TED.2007.902871](https://doi.org/10.1109/TED.2007.902871).

- [73] S. Das Sarma, Xin Wang, and Shuo Yang. “Hubbard model description of silicon spin qubits: Charge stability diagram and tunnel coupling in Si double quantum dots”. In: *Phys. Rev. B* 83 (23 2011), p. 235314. DOI: [10.1103/PhysRevB.83.235314](https://doi.org/10.1103/PhysRevB.83.235314).
- [74] W. G. van der Wiel et al. “Electron transport through double quantum dots”. In: *Reviews of Modern Physics* 75.1 (2002), pp. 1–22. DOI: [10.1103/revmodphys.75.1](https://doi.org/10.1103/revmodphys.75.1).
- [75] Wolfgang Gös. “Hole trapping and the negative bias temperature instability”. PhD thesis. 2011.
- [76] L DiCarlo et al. “Differential charge sensing and charge delocalization in a tunable double quantum dot”. In: *Physical review letters* 92.22 (2004), p. 226801.
- [77] JR Petta, AC Johnson, CM Marcus, MP Hanson, and AC Gossard. “Manipulation of a single charge in a double quantum dot”. In: *Physical review letters* 93.18 (2004), p. 186802.
- [78] Daniel Manzano. “A short introduction to the Lindblad master equation”. In: *AIP Advances* 10.2 (2020), 025f106.
- [79] Steffen J Glaser et al. “Training Schrödinger’s cat: quantum optimal control”. In: *The European Physical Journal D* 69.12 (2015), pp. 1–24.
- [80] Bilal Riaz, Cong Shuang, and Shahid Qamar. “Optimal control methods for quantum gate preparation: a comparative study”. In: *Quantum Information Processing* 18.4 (2019), p. 100. ISSN: 1573-1332. DOI: [10.1007/s11128-019-2190-0](https://doi.org/10.1007/s11128-019-2190-0).
- [81] Ingvild Hansen et al. *The SMART protocol – Pulse engineering of a global field for robust and universal quantum computation*. 2021.
- [82] Charu C Aggarwal et al. *Neural networks and deep learning*. Vol. 10. Springer, 2018, pp. 978–3.
- [83] Alastair Kay. “Tutorial on the quantikz package”. In: *arXiv preprint arXiv:1809.03842* (2018).
- [84] Navin Khaneja, Timo Reiss, Cindie Kehlet, Thomas Schulte-Herbrüggen, and Steffen J. Glaser. “Optimal control of coupled spin dynamics: design of NMR pulse sequences by gradient ascent algorithms”. In: *Journal of Magnetic Resonance* 172.2 (2005), pp. 296–305. ISSN: 1090-7807. DOI: <https://doi.org/10.1016/j.jmr.2004.11.004>.
- [85] P. de Fouquieres, S.G. Schirmer, S.J. Glaser, and Ilya Kuprov. “Second order gradient ascent pulse engineering”. In: *Journal of Magnetic Resonance* 212.2 (2011), pp. 412–417. ISSN: 1090-7807. DOI: <https://doi.org/10.1016/j.jmr.2011.07.023>.

- [86] D. L. Goodwin and Ilya Kuprov. “Modified Newton-Raphson GRAPE methods for optimal control of spin systems”. In: *The Journal of Chemical Physics* 144.20 (2016), p. 204107. DOI: [10.1063/1.4949534](https://doi.org/10.1063/1.4949534).
- [87] D. L. Goodwin and Ilya Kuprov. “Auxiliary matrix formalism for interaction representation transformations, optimal control, and spin relaxation theories”. In: *The Journal of Chemical Physics* 143.8 (2015), p. 084113. DOI: [10.1063/1.4928978](https://doi.org/10.1063/1.4928978).
- [88] Mohamed Abdelhafez, David I. Schuster, and Jens Koch. “Gradient-based optimal control of open quantum systems using quantum trajectories and automatic differentiation”. In: *Phys. Rev. A* 99 (5 2019), p. 052327. DOI: [10.1103/PhysRevA.99.052327](https://doi.org/10.1103/PhysRevA.99.052327).
- [89] Nelson Leung, Mohamed Abdelhafez, Jens Koch, and David Schuster. “Speedup for quantum optimal control from automatic differentiation based on graphics processing units”. In: *Phys. Rev. A* 95 (4 2017), p. 042318. DOI: [10.1103/PhysRevA.95.042318](https://doi.org/10.1103/PhysRevA.95.042318).
- [90] CH Yang et al. “Silicon qubit fidelities approaching incoherent noise limits via pulse engineering”. In: *Nature Electronics* 2.4 (2019), pp. 151–158.
- [91] Holger Haas. “Engineering the effective Hamiltonians for Magnetic Resonance”. thesis. University of Waterloo, July 22, 2019.
- [92] David L. Goodwin. “Advanced optimal control methods for spin systems”. PhD thesis. University of Southampton, 2017.
- [93] Michael Riesch and Christian Jirauschek. “Analyzing the positivity preservation of numerical methods for the Liouville-von Neumann equation”. In: *Journal of Computational Physics* 390 (2019), 290–296. ISSN: 0021-9991. DOI: [10.1016/j.jcp.2019.04.006](https://doi.org/10.1016/j.jcp.2019.04.006).